Université de Montréal

A study of the large-scale structure of the wind of WR 134

par
Emily Aldoretta

Département de Physique
Faculté des arts et des sciences

Mémoire présenté à la Faculté des études supérieures
en vue de l'obtention du grade de Maître ès sciences (M.Sc.)
en Physique

October, 2015

Université de Montréal
Faculté des études supérieures

Ce mémoire intitulé:

A study of the large-scale structure of the wind of WR 134

présenté par:

Emily Aldoretta

a été évalué par un jury composé des personnes suivantes:

Pierre Bergeron ,	président-rapporteur
Nicole St-Louis,	directeur de recherche
David Lafrenière,	membre du jury

Mémoire accepté le: December 2015

RÉSUMÉ

Diverses méthodes ont été utilisées pour étudier les étoiles Wolf-Rayet (WR) dans le but de comprendre les phénomènes physiques variés qui prennent place dans leur vent dense. Pour étudier la variabilité qui n'est pas strictement périodique et ayant des caractéristiques différentes d'une époque à l'autre, il faut observer pendant des périodes de temps suffisamment longues en adopter un échantillonnage temporel élevé pour être en mesure d'identifier les phénomènes physiques sous-jacents. À l'été 2013, des astronomes professionnels et amateurs du monde entier ont contribué à une campagne d'observation de 4 mois, principalement en spectroscopie, mais aussi en photométrie, polarimétrie et en interférométrie, pour observer les 3 premières étoiles Wolf-Rayet découvertes: WR 134 (WN6b), WR 135 (WC8) et WR 137 (WC7pd + O9). Chacune de ces étoiles est intéressante à sa manière, chacune présentant une variété différente de structures dans son vent. Les données spectroscopiques de cette campagne ont été réduites et analysées pour l'étoile présumée simple WR 134 pour mieux comprendre le comportement de sa variabilité périodique à long terme dans le cadre d'une étude des régions d'interactions en corotation (CIRs) qui se retrouvent dans son vent. Les résultats de cette étude sont présentés dans ce mémoire.

Mots clés: techniques: spectroscopique - instabilités - les étoiles: massive - les étoiles: Wolf-Rayet - les étoiles: individuel (WR 134) - méthodes: l'analyse des données

ABSTRACT

Wolf-Rayet stars have been studied using various methods in order to understand the many physical phenomena taking place in their dense outflows. In the case of variability that is not strictly periodic or for epoch-dependant changes, the challenge is to observe for sufficiently long periods of time and with a high enough time sampling to be able to understand the underlying phenomena. During the summer of 2013, professional and amateur astronomers from around the world contributed to a 4-month campaign, mainly in spectroscopy but also in photometry, polarimetry and interferometry, to observe the first 3 Wolf-Rayet stars discovered: WR 134 (WN6b), WR 135 (WC8) and WR 137 (WC7pd+O9). Each of these stars are interesting in their own way, showing a variety of stellar wind structures. The spectroscopic data from this campaign have been reduced and analyzed for the presumably single star WR 134 in order to better understand its behavior and long-term periodicity in the context of corotating interaction regions (CIRs) in the wind. The results of this study are presented in this thesis.

Keywords: techniques: spectroscopic - instabilities - stars: massive - stars: Wolf-Rayet - stars: individual (WR 134) - methods: data analysis

TABLE DES MATIÈRES

LISTE DES TABLEAUX

LISTE DES FIGURES

LISTE DES ANNEXES

LISTE DES SIGLES

BSG	Blue Supergiant
CAK	Castor, Abbott and Klein
CIR	Corotating Interaction Region
DAC	Discrete Absorption Component
EW	Equivalent Width
HRD	Hertzsprung-Russel Diagram
IAC	Instituto de Astrofísica de Canarias
ISM	Interstellar Medium
IUE	International Ultraviolet Explorer
LBV	Luminous Blue Variable
NAC	Narrow Absorption Component
NOT	Nordic Optical Telescope
OMM	Observatoire du Mont-Mégantic
RSG	Red Supergiant
SN	Supernova
WR	Wolf-Rayet

NOTATION

Å	Angstroms
$M_\odot$	solar mass (2.0×10^{33} g)
$\dot{M}$	mass-loss rate
R_*	stellar radius
τ_ν	monochromatic optical depth
T	temperature (Kelvin)
v_∞	terminal velocity (km s^{-1})
Z	metallicity

For my parents with love.

REMERCIEMENTS

I would like to thank Nicole St-Louis for providing her knowledge and support during the completion of this project. I thank the entire amateur spectroscopy community that provided the data for this campaign and the Instituto de Astrofísica de Canarias for providing us an amazing telescope on Tenerife and allowed our collaboration access for four months. I also thank Thomas Eversberg, for collaborating with Tenerife and organizing the German amateur group, all of which provided their own money in order to travel to Teide Observatory. I am also grateful to Berthold Stöber, who provided the echelle spectrograph used the majority of the run at Teide Observatory. The entire French amateur group for providing all of their own money in order to collect data on Tenerife, and Mike Potter, Dong Li, Robin Leadbeater and John Strachan for using their own telescopes, cameras and spectrographs. The professional observatories: Sergio Simon-Diaz at NOT, Grant Hill at Keck Observatory, Robert Lamontange at l'Observatoire du Mont-Mégantic, and Brankica Surlan and Jiri Kubat at Ondřejov Observatory for their contributions. The entire massive star group at the Université de Montréal, who all helped collecting and reducing data at OMM: Bert Pablo, Melissa Muñoz, Tahina Ramiaramantsoa, Raphael Maltais-Tariant, Annabelle Richard and Lucas St-Jean. Noel Richardson who helped with the data collection, reduction and bug fixes. Anthony Moffat, Nicole St-Louis and Thomas Eversberg who initially began the collaboration and chose the targets. And finally I want to thank my mother, father and Brian for their unconditional love and support.

CHAPTER 1

LARGE-SCALE STRUCTURES IN HOT-STAR WINDS

1.1 Wolf-Rayet Stars

Wolf-Rayet (WR) stars were first observed in 1867 by the French astronomers Charles Wolf and Georges Rayet at the Paris Observatory (Wolf & Rayet, 1867). These stars are extremely hot and massive with a continuous and sustained outflow of material. Most WR stars evolved from main-sequence (MS) O-type stars and originally had masses over 25 $M_{\odot}$ (Crowther & Smartt, 2007). Due to their high mass-loss rate, these WR stars have lost their outer hydrogen envelope and moved onto fusing helium within their cores. These objects have extremely broad emission lines, making them unusual compared to other stars. The broad emission lines are due to Doppler broadening from high-velocity winds moving out in all directions. Some WR stars still show traces of hydrogen in their wind (WNh) and can be very luminous H-burning MS stars. Once all the hydrogen has been removed, they appear as WN stars with broad nitrogen (from the H-burning CNO-cycle) and helium lines and later as WC stars, which show mainly broad carbon and oxygen lines. For MS stars, the usual evolutionary tracks are presented in Figure 1.1, while Figure 1.2 shows the optical spectra of a small sample of massive stars.

Wolf-Rayet stars are also known for their inhomogeneous winds. Using several observational methods, stochastic clumps along with larger structures can be detected within the stellar outflow. Because these massive stars have mass-loss rates that are ~ 10 times stronger than their progenitors, the winds are optically thick and the hydrostatic cores cannot be directly observed. Therefore, observing the stellar winds becomes the only method, albeit indirect, to determine the activity of the hydrostatic core. While the small-scale structures within the wind can be explained on the basis of radiative instabilities (Owocki & Rybicki, 1991) and subsurface convection (Cantiello et al., 2009), the large-scale structures still have an unknown origin. Determining the causes of these large-scale structures present within the wind will have a major impact on what is known about the nature of these stars.

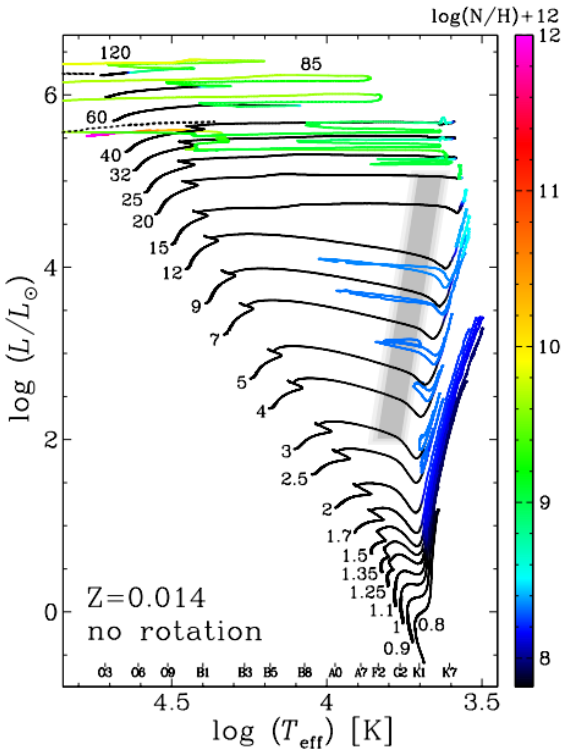

Figure 1.1: Hertzsprung-Russell diagram for non-rotating stellar evolutionary models as a function of effective temperature and luminosity. The tracks represent the evolutionary models for stars with different solar masses. The color scale indicates the surface number abundance of nitrogen on a log scale where the abundance of hydrogen is 12. The tracks that are drawn with black dotted lines display stars that have become a WNE type Wolf-Rayet star. The gray shaded area shows the Cepheid instability strip. (Ekström et al., 2012)

1.2 Stellar winds

Hot, massive stars emit particles along with radiation, thereby creating their stellar winds. When these stellar winds are observed, many parameters can be derived, the most important of which are the mass-loss rate of the star ($\dot{M}$) and the terminal velocity of the wind (v_∞). The stellar mass-loss rate is defined as the amount of mass lost per unit of time and is expressed in units of solar masses per year (1 $M_\odot$ yr^{-1} = 6.303 $\times$ 10^{25} g s^{-1}). Deriving the mass-loss rate of a star is important for determining its evolution; stars with higher mass-loss rates will not evolve in the same manner as those with low mass-loss rates. The terminal velocity of a stellar wind can range between $\sim$ 10 km s^{-1}

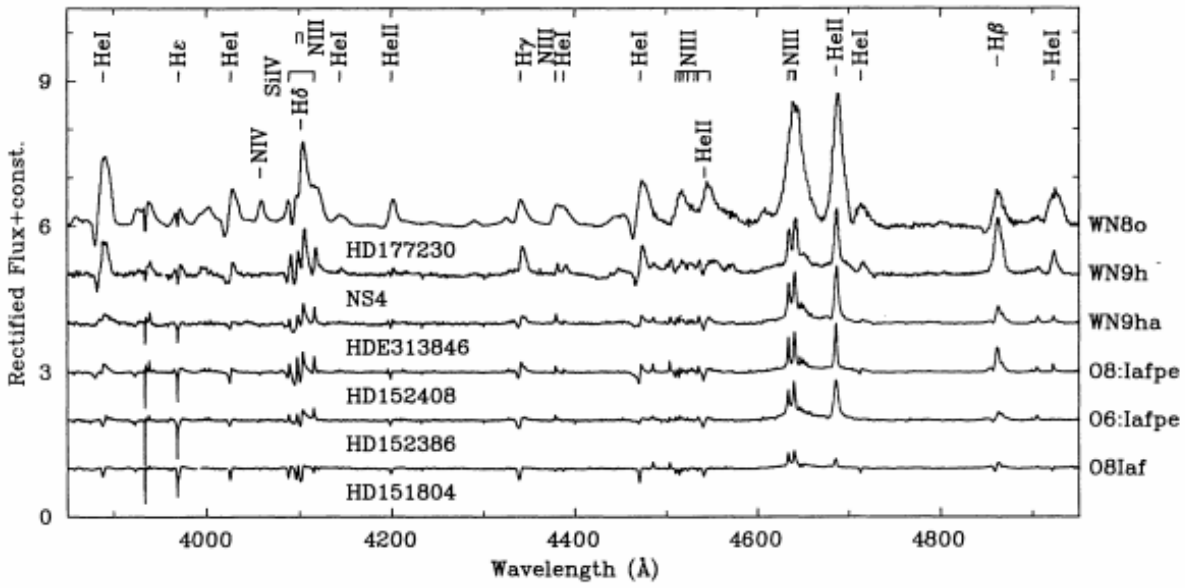

Figure 1.2: Emission lines formed in stellar winds, showing part of the optical spectrum of six stars of spectral types between O8Iaf to WN8 with progressively stronger winds. (Crowther & Bohannan, 1996)

for cooler supergiants to 3000 km s^{-1} (and occasionally more) for hot, luminous stars. When these two derived values are compared with predictions, the mechanism responsible for the stellar mass-loss can be determined. Knowing these two values will also help to understand the effect a stellar wind can have on the interstellar medium surrounding the star.

When a stationary, spherically symmetric wind is observed, the mass-loss rate is then related to the velocity, $v(r)$, and the density, $\rho(r)$, at any point within the wind by

$$\dot{M} = 4\pi r^2 \rho(r) v(r), \tag{1.1}$$

or better known as the equation of mass continuity, r being the distance from the center of the star. This equation assumes that no material in the wind is created or destroyed, i.e. the same amount of gas is flowing per second through any sphere of radius r. The velocity of the wind will approach the terminal velocity at a very large distance from the star ($v_\infty = v(r \to \infty)$). The velocity law, $v(r)$, is defined by the distribution of the wind

velocity with radial distance from the center of the star:

$$v(r) \simeq v_0 + (v_\infty - v_0)\left(1 - \frac{R_*}{r}\right)^\beta, \tag{1.2}$$

with v_0 being the velocity at the hydrostatic radius ($r = R_*$) (Lamers & Cassinelli, 1999). This law states that the velocity will generally increase from v_0 to v_∞. The β parameter describes the steepness of the velocity law. Stars that show winds with a fast acceleration will reach 80% of their terminal velocity 3.1 R_* above their surface, giving them β values of $\simeq 0.8$. This velocity law can be expressed with an alternate form, commonly called the β law:

$$v(r) \simeq v_\infty\left(1 - \frac{r_0}{r}\right)^\beta, \tag{1.3}$$

where

$$r_0 = R_*\left[1 - \left(\frac{v_0}{v_\infty}\right)^{1/\beta}\right]. \tag{1.4}$$

This velocity law has a slight advantage over Eq. 1.2 due to the fact that it gives better results at small distances from the photosphere (Lamers & Cassinelli, 1999). Using these equations helps to derive the information needed to study the past and future evolution of these massive stars.

The initial mass of a star has a major impact on how its life will proceed. Stars that begin with masses greater than 25 $M_\odot$ will have significant mass loss occurring throughout their entire lives, having an effect on their stellar evolution (Lamers & Cassinelli, 1999). Figure 1.3 displays the internal structure and evolution of these massive stars. While the initial mass has a large impact on a star's life, their deaths are also impacted by their masses. A star with an initial mass below 8 $M_\odot$ and thus a final mass below 1.4 $M_\odot$ will generally become a white dwarf, while stars above 8 $M_\odot$ will end their lives in a supernova explosion, leaving either a neutron star or a black hole behind. The mass loss during a star's life plays a huge role in the way they end their lives, while the amount of mass lost is largely affected by the stellar winds. The stellar winds (velocities, structures, etc.) directly impact the fate of these stars and how they affect the interstellar medium (ISM) around them.

Another important factor that must be taken into account when studying stars with

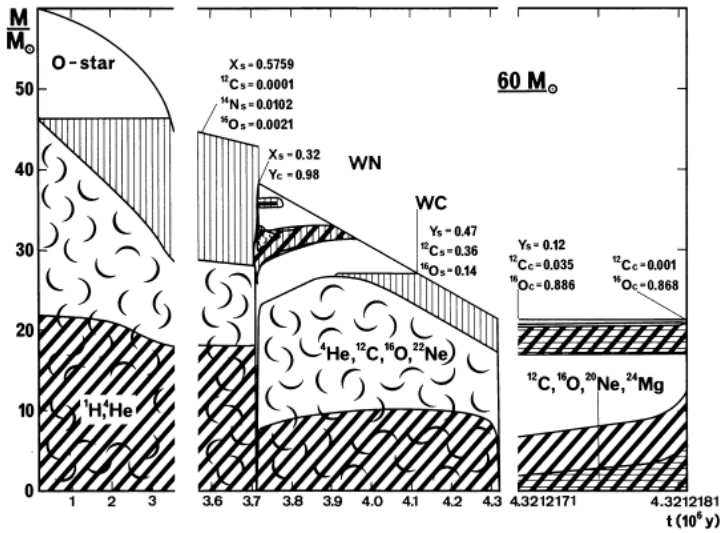

Figure 1.3: Internal structure of a star with an initial mass of 60 $M_\odot$ in the HRD as a function of time. Different spectral types and their phases are indicated. Curly regions indicate convective zones, while the diagonal lines indicate where most of the nuclear fusion takes place. (Maeder & Meynet, 1987)

thick winds is the optical depth, τ_ν, of the wind itself,

$$\tau_\nu = -\int \kappa_\nu \rho dr. \tag{1.5}$$

A star with an ionized wind will emit excess radiation compared to a star without a wind:

$$\frac{L_\nu}{L_\nu^*} \simeq \frac{r^2(\tau_\nu = \tau_{eff})}{R_*^2} \frac{B_{\nu,\mathrm{wind}}(T(\tau_\nu = \tau_{eff}))}{B_\nu(T_{\mathrm{eff}})}, \tag{1.6}$$

where

$$L_\nu \simeq 4\pi r^2(\tau_\nu = \tau_{eff})\pi B_\nu(T(\tau_\nu = \tau_{eff})) \tag{1.7}$$

and

$$L_\nu^* \simeq 4\pi R_*^2 \pi B_\nu(T_{eff}) \tag{1.8}$$

are the monochromatic luminosities (in erg s^{-1} Hz^{-1}) of stars with and without a wind, respectively and τ_{eff} is the effective optical depth. The excess radiation will increase to longer wavelengths because $r(\tau_\nu \simeq \tau_{eff})$ will move outward with increasing λ or decreasing ν (Lamers & Cassinelli, 1999).

Massive stars have all been shown to have strong stellar winds and high mass-loss rates during several phases of their evolution: early B stars, O stars, Luminous Blue Variables (LBVs) and WR stars, with WR stars having terminal velocities of $v_\infty \sim 10^3$ km s^{-1} and mass-loss rates of $\dot{M} \sim 10^{-5}\ M_\odot$ yr^{-1}. From different observational methods, it has been shown that each of these types of stars can show both large-scale systematic structures and small, stochastic multi-scale structures within their winds. What the origin of these structures are, however, is still an ongoing determination.

1.2.1 Structures in the wind

The strong winds of luminous, massive stars show many structures within them. Using several observational methods, small as well as large-scale structures can be detected. The small-scale structures were first identified by Moffat et al. (1988) and were determined to be multi-scaled clumps, or blobs, moving out in the wind on timescales of hours. While these blobs are observable with spectroscopy, it was not known at the time exactly what causes these features within the wind. Owocki & Rybicki (1984) researched the effects of the instability of the line-driving mechanism, which is a likely cause of these small structures, while Cantiello et al. (2009) studied the sub-surface convection zones in hot, massive stars caused by the opacity peaks of iron and helium ionization (see Figure 1.4). It is believed that such convection can help to initiate instabilities in the wind.

Owocki & Rybicki (1984) examined the stability of absorption-line-driven flows, such as the winds of hot stars, against small-amplitude perturbations. Unlike previous studies, the assumptions that the flow perturbations are optically thin and that they satisfy the Sobolev approximation (simplified solution to the radiative transfer equation, treating each point in the medium as being isolated from other points) were avoided. These authors were able to determine that the supersonic portions of the absorption-line-driven flows are in fact unstable against perturbations having a length scale of the order of (or smaller than) the Sobolev length, which is defined as the length over which the conditions of the gas do not change and the approximation is valid. It was also determined that the Sobolev length represents a critical length that bridges the unstable and stable regimes of the winds. These unstable perturbations that have a length scale of the order of the Sobolev length are also complicated and have highly dispersive propagations.

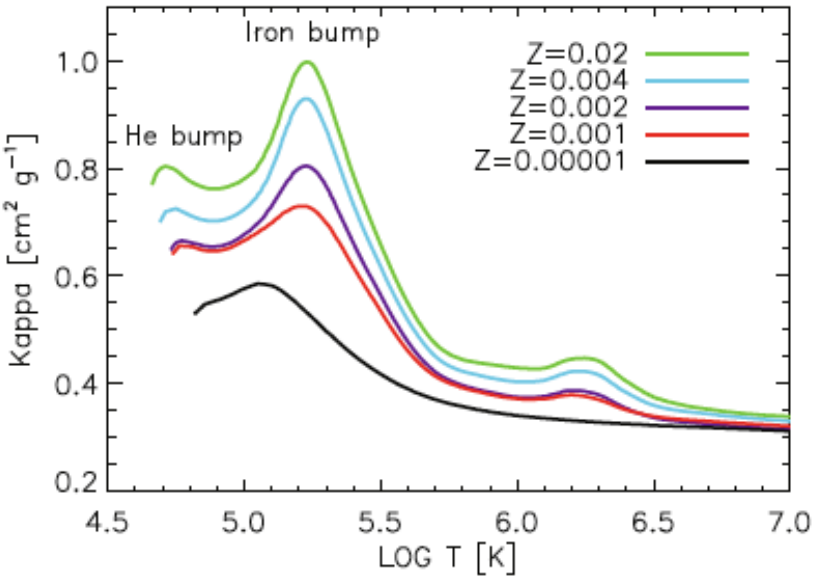

Figure 1.4: Opacity in the interior of 60 $M_\odot$ zero-age main sequence stars of various metallicities as a function of temperature, from the surface up to a temperature of 10^7 K. The different colors refer to different metallicities. (Cantiello et al., 2009)

Owocki & Rybicki (1985) extended their previous work to include the possible effects of the scattered radiation on the line-driving instability. The finite angular size of the stellar photosphere was also taken into account. It was determined that the mean scattered radiation exerts a drag force on velocity perturbations, eliminating the contribution of scattering lines to the flow's instability at the base of the wind. However, when limb darkening is included, the scattering line growth rate at the wind's base becomes positive, although only a few percent of the rate for pure absorption lines. The scattering line growth rate was shown to increase rapidly to more than 50% of the rate for pure absorption lines within a stellar radius of the star's surface and will eventually reach 80% of this rate far from the star. The overall conclusion drawn by Owocki & Rybicki (1985) is that most of the material within a radiatively-driven wind is still very unstable, even when the effects of scattered radiation are taken into account. While the base cause of these small-scale structures was discovered to be the line-driving instabilities, the sub-surface convection zone also has a role in initiating these instabilities.

The convection zones of massive stars cause observable motions near the stellar sur-

face. Because the convection zones are near the photosphere, they may also generate a small-scale magnetic field, affecting the stellar angular momentum loss. Cantiello et al. (2009) predicted that the thickness of the subsurface iron convection zone (FeCZ) increases with increasing metallicity, decreasing effective temperature and increasing luminosity. Cantiello et al. (2009) showed that each of these trends predicted by their model were reflected in observational signatures (i.e. microturblence, non-radial pulsations, wind clumping and line-profile variability), suggesting that the micro-turbulence creates a physical motion of the gas in the atmosphere of the star. This establishes a link between sub-surface convection and stochastic variabilities in the photosphere. Because the iron opacity peak in WR stars can be located at or near the sonic point of the wind, the FeCZ may be strongest in these stars, further concluding that these micro-turbulences do in fact induce the clumps within the WR-star winds.

1.3 Observations of Corotating Interaction Regions

Corotating interaction regions (CIRs) form in the winds of hot stars because of a perturbation at the base of the wind, which locally causes more or less wind driving and therefore the generation of different velocity flows that collide as the star rotates (Cranmer & Owocki, 1996). This phenomenon was first discovered within the solar wind (Mullan, 1984) and has since been identified in massive-star winds using different observational methods. The cause of these structures was attributed to phenomena at the base of the wind, such as surface brightening or darkening associated with magnetic fields or non-radial pulsations. Using UV spectroscopy, narrow absorption components (NACs), which are thought to be snap-shots of discrete absorption components (DACs), can be observed for all O stars in the P Cygni absorption components of strong resonance lines. These observational signatures of CIRs have also been shown to be correlated with blue-edge variability of ultraviolet P Cygni absorption components (Howarth & Prinja, 1996). These DAC features are produced when a CIR in the wind intercepts the observer's line of sight. While most O-type stars show DACs or NACs, only one WR star has shown them, due to their generally saturated absorption components. The observations of optical emission lines have, however, shown that CIRs are present in the winds of WR 1, WR 6 and WR 134 (Chené & St-Louis, 2010; Morel et al., 1997, 1999). Using photometry, spectroscopy

and polarimetry it is possible to learn more about these features and how they are formed.

1.3.1 Photometry

Stochastic inhomogeneities in the thick winds of WR stars render the photometric variability of single WR stars mainly random in nature. CIRs are extremely difficult to reveal in photometry because in addition to using an integrated quantity, CIRs are also epoch-dependent. Therefore, very intense and continuous observing runs are required. Such datasets can only be obtained using space-based observations. Chené et al. (2011) secured such observations for the WN5-6b star WR 110. They obtained nearly continuous observations of the star for a period of 30 days using the MOST satellite (see Figure 1.5). From these data, they were able to identify a periodicity of $P = 4.08 \pm 0.55$ days including several harmonics of the period. These authors attributed the periodic variations as arising from the inner part of a CIR. Depending on the number of CIRs they adopt, the period could also be double this value. They were, however, unable to detect the CIRs in spectroscopy due to insufficient data and therefore a kinematic confirmation still remains to be obtained.

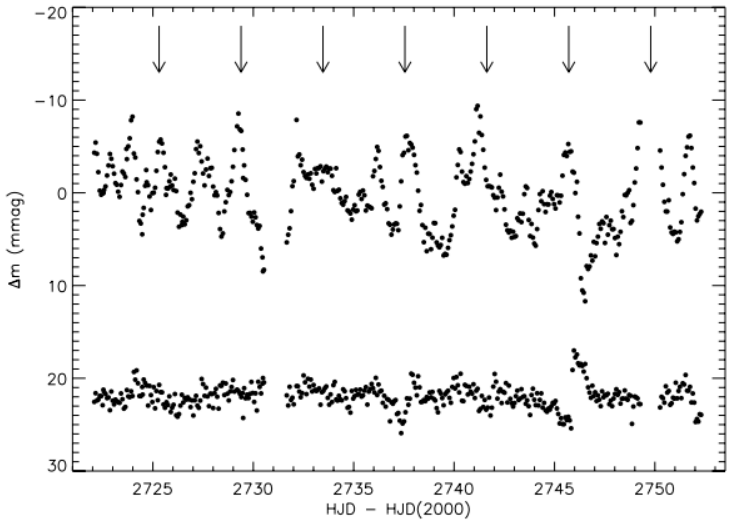

Figure 1.5: Upper curve shows the MOST light curve of WR 110 in 101 minute bins. The vertical arrows indicate intervals of 4.08 days. Lower curves show the simultaneous MOST light curve of HD 312657 reduced in the same way as WR 110 with an arbitrarily displaced magnitude zero point. (Chené et al., 2011)

No such data set exists for WR 134. However, Moffat & Marchenko (1993) studied this star for approximately two years. Daily UBV monitoring of this object using one of the 0.25m automatic photometric telescopes on Mount Hopkins was performed and it showed evidence of a relatively long period of $P = 37.2 \pm 0.4$d for each filter, in addition to a variability with a period of $\simeq 2$ days, which was previously identified by McCandliss et al. (1994). Part of the observations of the Moffat & Marchenko (1993) are presented in Figure 1.6 (third epoch) where the longer period variations are illustrated. The short two-day period is strongly suspected to be the rotation period of the star itself. Variations believed to be caused by CIRs within the wind of this star have been found as sub-peaks moving across the broad emission line (Morel et al., 1999). Moffat & Marchenko (1993) interpreted the longer timescale variability as being caused by either (a) LBV-like micro-variability or (b) the precession of the WR star in a close binary system with a period of 2 days. The target WR 134 was found to be variable, while the reference star, chosen to be WR 136 (WN6), was constant within the errors.

There are several suggested explanations for such long-term periods found in the light curves: binarity, rotation of a star with a spotted surface, intrinsic variability due to mass loss and LBV-like micro-variations. The longer period variations of relatively low amplitude are unlikely to be caused by intrinsic variability of LBV-type stars, as these generally show amplitudes of variation that are much higher (van Genderen, 1985). The second scenario is also unlikely because a rotation period of $P \sim 1$d is expected if one adopts, by analogy with typical rotation velocities of main-sequence OB stars, a rotation velocity of $\sim$200 km s^{-1} (Moffat & Marchenko, 1993). Therefore it is not clear what exactly is the cause for the longer period seen in the photometry of WR 134 by Moffat & Marchenko (1993). While photometric observations are useful to determine the periodicity of WR binary systems, these observations are insufficient on their own to determine the detailed properties of single WR stars and their winds.

1.3.2 Spectroscopy

Contrary to photometry, spectroscopy has the advantage of providing kinematical information in addition to intensity information. As previously mentioned, CIRs can manifest themselves in OB-star spectra as discrete absorption components (DACs) propagating blue

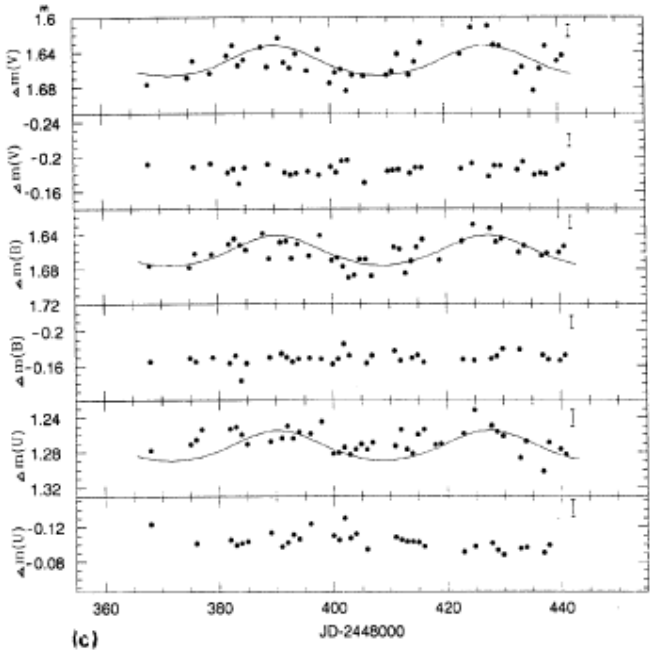

Figure 1.6: Light-curves for WR 134 on an expanded time scale for one epoch in UBV filters. From top to bottom: WR - c(V), ch - c(V), WR - c(B), ch - c(B), WR - c(U), ch - c(U) with *ch* representing the check star and *c* representing the comparison star. The curves represent the modeled fit using a precessing binary model with $i_0 = 72.5°$ and $\Delta i = 7.5°$. (Moffat & Marchenko, 1993)

ward in the P Cygni absorption components of strong resonance lines. Thus, they can be detected using UV spectroscopy where most of these lines can be found. This type of feature has also been shown to have recurrence timescales comparable to the rotation period of the star. CIRs can also manifest themselves as excess emission features moving across the tops of the strong emission lines of WR stars in the optical. OB stars would show both DACs and excess subpeaks in their emission lines if their winds were stronger and/or in spectra of better quality due to the strength required for CIRs to manifest within their winds. Conversely, WR stars would also show both if their winds were weaker.

DACs were detected in the B supergiant HD 64760 (B0.5Ib) by Lobel & Blomme (2008) in a continuous time series of *IUE* high-resolution spectra during the 16-day *IUE* MEGA campaign in 1995. Their dynamic spectra shown in Fig. 1.7 reveals several repeating doublet features within the absorption components of the P Cygni profile of both components of the Si IV λ1393,1402 doublet. Narrow, straight vertical lines can be seen around 0 and

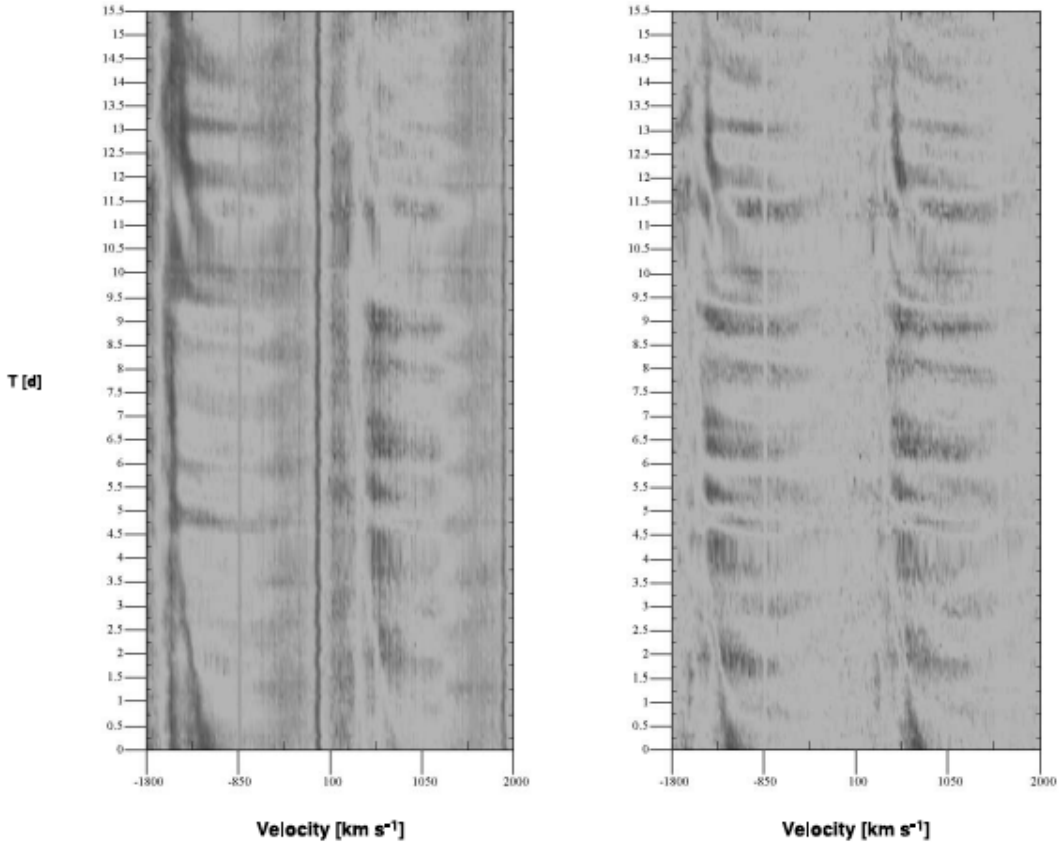

Figure 1.7: Time sequence of the IUE normalized flux of the Si IV λ1400 resonance doublet of HD 64760 is shown on the left. In order to remove the underlying shape of the P Cygni profile of the doublet to help reveal the variations, the mean flux per wavelength bin was subtracted from the absolute flux image, which is shown on the right. DACs can be seen drifting blue-ward from velocities exceeding $\sim$ -1000 to -1600 km s^{-1}. Dark and bright shades indicate low and high flux levels. (Lobel & Blomme, 2008)

+1900 km s^{-1}, which are caused by lines found in the ISM in the line of sight toward this star. The DACs are slowly migrating blue-ward between $T = 0$ and ~ 5 days, and also between $T = 10$ and 15 days. During the same campaign, Howarth et al. (1995) also observed DACs in the O4 supergiant ζ Puppis. They found two periodicities in their dataset, one they associate with the recurrence timescale of DACs ($P = 19.2$ hours) and the other to the rotational period of the star ($P = 5.2$ days).

Finally, the third star observed during the *IUE* MEGA campaign, WR 6, was also shown to display periodic variability in its UV P Cygni absorption components, but due to saturation effects, these were confined to the blue edge at velocities higher than the terminal velocity of the wind. The previously known period of $P = 3.76$ days was associated to the rotation of the star (St-Louis et al., 1995). Simultaneously with this campaign, Morel et al. (1997) obtained an extensive time series over 20 consecutive nights of optical spectra of the same star and detected excess emissions moving with the same period across strong emission lines. A strong correlation between variations in all lines and simultaneously observed optical photometric variability led them to conclude that the changes are caused by the presence of a CIR in the wind of this star.

Morel et al. (1999) observed the He II λ4686 emission line of WR 134 for three separate epochs (as an example, see Figure 1.8). This star was known to show variability with a period of ~ 2.3 days (McCandliss et al., 1994). To quantify the variability, these authors measured the central moments of the line, which are given by

$$\mu_n = \frac{\Sigma_j (\lambda_j - \bar{\lambda})^n I_j}{\Sigma_j I_j} : \tag{1.9}$$

where

$$\bar{\lambda} = \frac{\Sigma_j \lambda_j I_j}{\Sigma_j I_j}, \tag{1.10}$$

and I_j is the intensity of the line, j is the corresponding index for different wavelengths across the spectral line and λ_j is the wavelength. Two main quantities are calculated from these moments : the skewness by $\mu_3/\mu_2^{3/2}$ and the kurtosis by μ_4/μ_2^2. The skewness quantifies the asymmetry of the line from the central wavelength, and therefore it is a good measurement to make to determine the period of the CIR with a large time sample of data, while the kurtosis measures how peaked the line is when compared to a gaussian and could

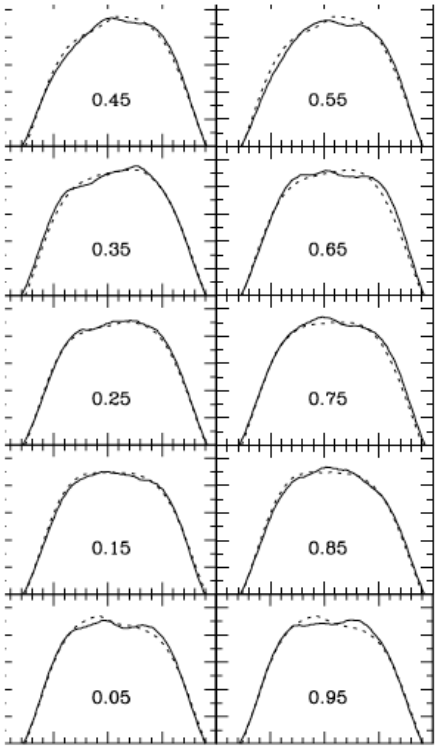

Figure 1.8: The observed (*solid line*) and the mean (*dotted line*) phase-dependent variations of the He II λ4686 emission line of WR 134, showing how a CIR moves across the top of an emission line in a WR star. Each corresponding phase is given. (Morel et al., 1999)

also be used to identify periodic changes. The power spectra (PS) were calculated using the Scargle (1982) technique on the centroid, skewness and FWHM of this line and allowed these authors to refine the period ($P = 2.25 \pm 0.05$ days). Once the period was determined for this dataset and identified in the variability of the various measurements of the line (Figure 1.9), an overall PS was created over the entire spectrum for a single epoch. Again, the highest peak responded to a frequency of $\nu_0 \approx 0.444$ day^{-1}, corresponding to $P_0 \approx 2.25$ days.

Another WR star that shows large-scale variability in its wind is WR 1 (see Figure 1.10). Chené & St-Louis (2010) collected 326 spectra of this object between 2003 and 2004 using several telescopes. Similarly to Morel et al. (1999), the skewness, kurtosis and equivalent widths (EWs) were calculated for He II λ5411 to search for periodic changes. The EW measurements gave no clear period due to the small amount of total line flux compared to the S/N of their data. However, both the skewness and kurtosis showed peaks

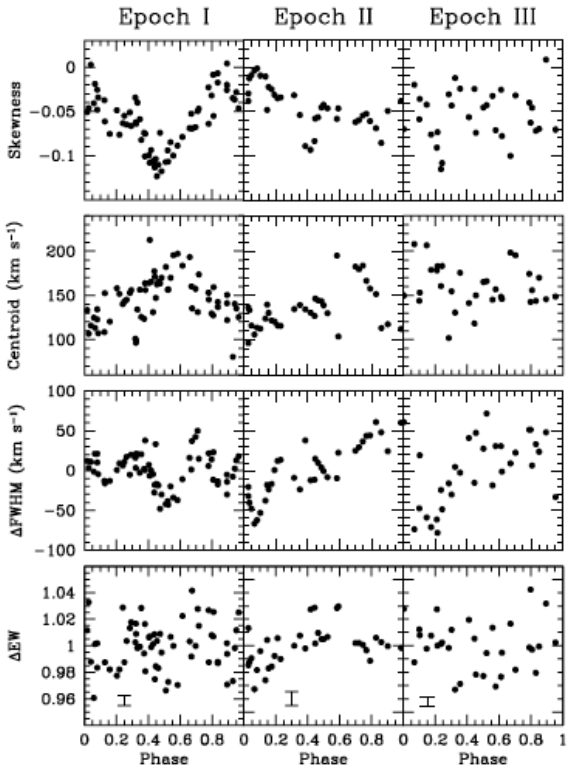

Figure 1.9: Skewness and centroid variations of WR 134, along with the deviations of the FWHM around the mean value and normalized EW variations of He II λ4686 for each epoch as a function of phase. The EW values have 2σ error bars. (Morel et al., 1999)

at a frequency of 0.059 day^{-1}. While long-term spectroscopic observations of these WR

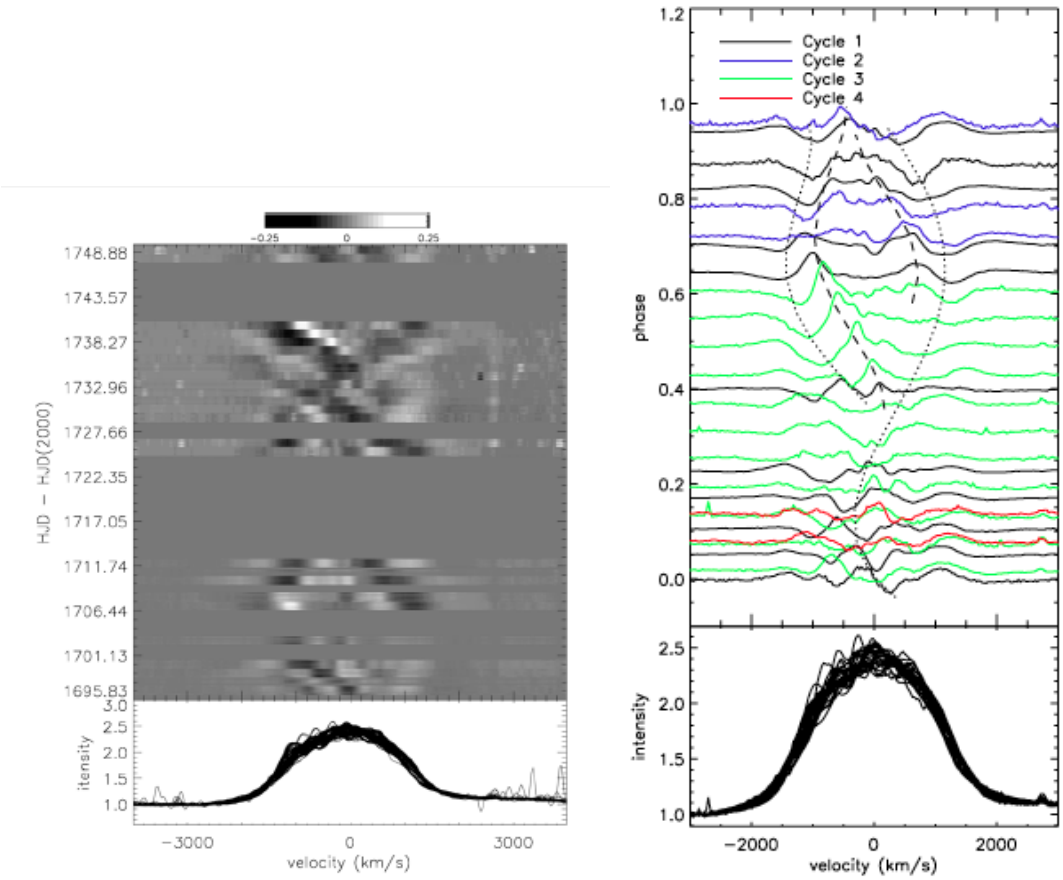

Figure 1.10: Left panel shows grayscale of residuals for the He II λ5411 line of WR 1 obtained by subtracting the mean spectrum of the entire dataset from the spectra taken during runs 4 and 5. Right panel shows the residual of nightly mean spectra from a portion of their observations folded with a period of 16.9 days of the same line with each cycle color in the legend. (Chené & St-Louis, 2010)

stars provide a wealth of information on CIRs within their winds, polarization can also help to shed some light on the variability of these stars.

1.3.3 Polarimetry

Because WR stars have dense winds that are strongly ionized and abundant in free electrons, the polarization of starlight can be a very effective tool for studying these winds. Linear polarization of starlight, in this case, is caused by these free electrons in the winds through Thomson scattering of the photons. No net polarization will be detected if the

free electrons in the wind form a spherically symmetrical distribution around the star, but if the system does show asymmetry then there will be a net component of the linearly polarized light. The dust in the line of sight in the ISM will also polarize the light, contaminating the intrinsic polarized light from the star and this must be accounted for. In order to distinguish between the interstellar and intrinsic components of the polarization, a criterion is needed. Variability can be used due to the fact that the interstellar dust, which generates the ISM polarization, will produce a constant value of polarization. The ISM polarization will also vary with regards to wavelength in a standard fashion, while polarization due to electron scattering is wavelength independent.

The Stokes' parameters Q and U are normally used to characterize the linearly polarized light of an object, while the V parameter is used to describe circularly polarized light. They are given by

$$\begin{aligned} Q &= S_0 P \cos(2\psi)\cos(2\chi) \\ U &= S_0 P \sin(2\psi)\cos(2\chi) \\ V &= S_0 P \sin(2\chi), \end{aligned} \tag{1.11}$$

where P is the degree of polarization, S_0 is the intensity of the light beam and ψ and χ are the spherical coordinates of the polarization vector. Because any polarized ellipse is indistinguishable from one that has been rotated by 180° and from one with semi-major axis lengths that have been swapped accompanied with a 90° rotation, the two spherical coordinates must be multiplied by a factor of two. When these parameters are plotted versus time and show variability it must be related to the star.

The WN4 star, WR 6 (EZ Canis Majoris) shows periodic variations in spectroscopy, photometry, but also in polarimetry. Robert et al. (1992) collected an extensive set of linear polarization observations of this star. They first assumed the detected variability originated in a binary and were able to produce a reasonable fit with an eccentric model, from which they determined the eccentricity ($e = 0.39 \pm 0.02$) and the inclination angle ($i = 114 \pm 3°$) of the system. However, the shape of the polarization light curve of this star is known to vary with epoch (Drissen et al., 1989), which is incompatible with a binary interpretation for this star. CIRs may be the alternative explanation for these results.

Ignace et al. (2015) developed a model to simulate light curves for variable polarization

from CIR structures within massive star winds. By assuming optically thin electron scattering, they produced several polarimetric light curves resulting from varied curvatures, latitudes and number of CIRs. Using these models, they found the net polarization from an unresolved source weighs more towards the inner radii of the wind, which is where the CIRs tend to be conical before they transition into a spiral shape several stellar radii away from the star. Figure 1.11 shows the resulting phased light curves and $q-u$ plane variations for both (a) two equatorial CIRs shifted from each other in longitude by various angles and (b) single CIRs that emerge from different latitudes. These models concluded that winds with a single CIR structure lead to double-wave polarization curves with equally spaced maxima while those with two CIRs yielded double-wave curves but with different phase separations depending on the longitudinal shifts between the two CIRs. Using more than 2 CIRs resulted in obtaining a large variety of curves, depending on the adopted parameters. The theoretical curves obtained for the case with 2 CIRs are extremely reminiscent of the ones found in the literature for periodic variability found for presumably single WR stars. Collecting data and analyzing photometry, spectroscopy and polarization is helpful, particularly when comparing them with the predictions of hydrodynamical models of CIRs in massive-star winds. Modeling stellar winds thus becomes a crucial step.

1.4 CIR models

Much progress has been made in modeling wind variability in massive stars by radiation hydrodynamics. Owocki et al. (1988) identified the line driving instability as the cause of small-scale intrinsic wind inhomogeneities, while Cranmer & Owocki (1996) studied the response of the winds to perturbations at its base for a rotating massive star. This latter study was motivated by the fact that an apparent correlation was found by Prinja & Howarth (1988) between both the recurrence and acceleration timescales of DACs and the projected rotational velocity of the star (v_e sin i). Cranmer & Owocki (1996) successfully modeled the dynamical effect of radiative driving on the formation of CIRs in hot star winds and also computed observational diagnostics to determine if DAC-like signatures could be reproduced.

Ideally, stellar wind modeling must necessarily be three-dimensional due to the fact that rotation imposes a latitude dependence on both the wind and the photosphere of the

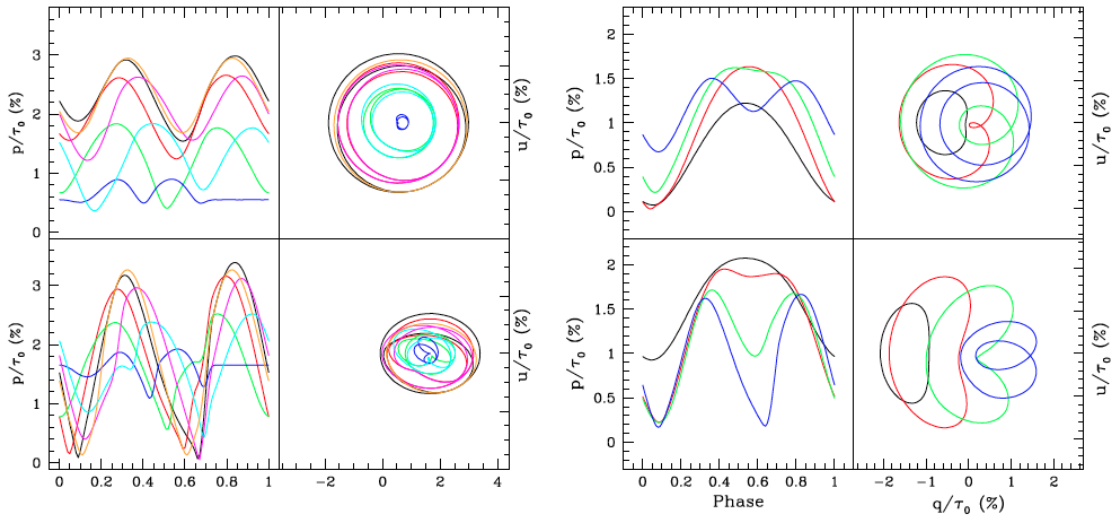

Figure 1.11: Left panel plots the periodic variable polarization for two equatorial CIRs that are shifted from each other by varying angles ($\Delta\phi = 0°$ (*black*), 30° (*red*), 60° (*green*), 90° (*dark blue*), 120° (*light blue*), 150° (*magenta*) and 180° (*orange*)). Right panel plots the periodic variations in polarization for single CIRs that emerge from different latitudes of the star ($\theta = 20°$ (*black*), 40° (*red*), 60° (*green*) and 80° (*blue*)). A viewing perspective of $i = 30°$ (*top*) and $i = 60°$ (*bottom*) are shown for phased light curves to the left and $q - u$ plane variations to the right. (Ignace et al., 2015)

star. However, to make the computations more manageable, Cranmer & Owocki (1996) restricted their models to the equatorial plane and adopted a rotation axis perpendicular to the line-of-sight where rotation has the strongest impact and where the flow can be constrained. A time-dependent hydrodynamics code was used to evolve a model of a radiatively-driven rotating wind toward a steady state. This code solves the Lagrangian form of the hydrodynamics equations in the fluid rest frame while remapping conserved quantities at each time step on an Eulerian grid using spherical coordinates. First the equation of mass conservation,

$$\frac{\partial \rho}{\partial t} + \frac{1}{r^2}\frac{\partial}{\partial r}(\rho v_r r^2) + \frac{1}{r\sin\theta}\frac{\partial}{\partial r}(\rho v_\phi) = 0, \tag{1.12}$$

and then the conservation of r (radial) and ϕ (azimuthal) components of the momentum,

$$\begin{aligned} \frac{\partial v_r}{\partial r} + v_r\frac{\partial v_r}{\partial r} + \frac{v_\phi}{r\sin\theta}\frac{\partial v_r}{\partial \phi} &= \frac{v_\phi^2}{r} - \frac{1}{\rho}\frac{\partial P}{\partial r} + g_r^{ext} \\ \frac{\partial v_\phi}{\partial t} + v_r\frac{\partial v_\phi}{\partial r} + \frac{v_\phi}{r\sin\theta}\frac{\partial v_\phi}{\partial \phi} &= -\frac{v_r v_\phi}{r} - \frac{1}{\rho r\sin\theta}\frac{\partial P}{\partial \phi} \end{aligned} \tag{1.13}$$

where ρ is the mass density, v_r and v_ϕ are the r and ϕ components of the velocity, and t is the time. It is assumed that the latitudinal components of the momentum conservation equation are satisfied in the equatorial plane, i.e. all latitudinal flow is considered negligible. The conservation of energy is also included in the code, along with a perfect gas law equation of state to evaluate the pressure.

The radial acceleration includes gravity and radiative driving by line scattering:

$$g_r = -\frac{GM_*(1-\Gamma)}{r^2} + g_r^{lines}, \tag{1.14}$$

where G and M_* are the gravitational constant and stellar mass. The Eddington factor that accounts for a reduction in effective gravity by outward radiation pressure on electrons is Γ $(= \kappa_e L_*/4\pi G M_* c)$, with κ_e is the electron scattering coefficient. The Sobolev line force per unit mass for one-dimensional winds can be parameterized as

$$g_r^{lines} = kf\left(\frac{1}{\kappa_e v_{th}\rho}\left|\frac{\partial v_r}{\partial r}\right|\right)^\alpha \frac{GM_*\Gamma}{r^2}, \tag{1.15}$$

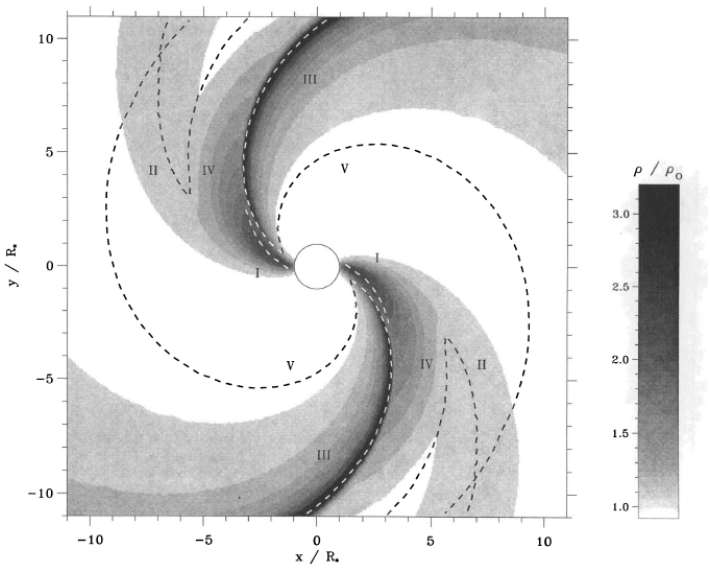

Figure 1.12: Grayscale of normalized density for bright spot model. Dashed lines are tracing the (I) direct spot enhancement, (II) prograde precursor, (III) CIR compression, (IV) CIR rarefaction and (V) radiative-acoustic Abbott kink. (Cranmer & Owocki, 1996)

where v_{th} is the fiducial ion thermal speed and the Castor, Abbott and Klein (CAK) parameters α and k are related to the normalization and slope of the power-law ensemble of lines (Castor et al., 1975). The Sobolev approximation assumes a monotonically accelerating velocity field. Stellar winds that have non-monotonic velocities will also have nonlocal line forces, which Cranmer & Owocki (1996) do not treat directly. Next, they introduced azimuthal structures in the models by varying the Sobolev line force over a star spot that was localized in the lower wind. This increase or decrease over a small area is equivalent to assuming a bright or dark region on the photosphere of the star. The line driving grows weaker for a dark spot in the wind and closer to the photosphere. An example of the resulting density structure in the wind is shown in Figures 1.12 and 1.13.

Cranmer & Owocki (1996) generated theoretical P Cygni profiles from their calculated optical depth distributions, showing several trends observed in DACs: (1) The slowly accelerating DAC features in the models fit well with a $\beta \approx 2$ - 4. However, no significant correlation between DAC acceleration timescales and the star's rotation rate was found. The CIRs in the model, however, are linked to the rotating surface, causing a correlation between the recurrence timescale of DACs and v_e (rotational velocity of the star). (2)

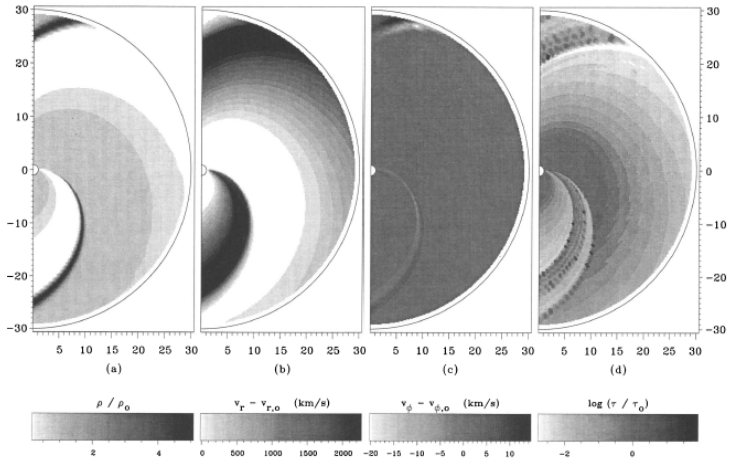

Figure 1.13: Model of a CIR structure assuming a dark spot on the star. The normalized (a) density, (b) radial velocity, (c) azimuthal velocity and (d) radial Sobolev optical depth are all shown. (Cranmer & Owocki, 1996)

The amplitude of the modeled spot perturbation is not dependent on the line velocity of the center of the DAC. (3) The column density and optical depth of the DAC can help determine the amplitude of the initial surface perturbation. The column density during a DAC evolution could provide more information on the azimuthal size of the initial perturbation. These models were able to produce DACs similar to those seen in real observations of massive-star winds.

While there have been many advances in the study of these hot, massive stars, it is still unclear what is happening below the photosphere to generate the extra line force that produces these large-scale structures within their winds. Studying these small and large scale variabilities will make it easier to understand how these stars evolve and how they will eventually die. These objects with high mass-loss rates have a major impact on the interstellar medium surrounding them and affect the star birth rate within our universe. With long-term studies of these winds and determining if these large-scale structures are periodic, these objects become less mysterious and their lives are unveiled.

CHAPTER 2

FIRST DETECTION OF A CIR LIFETIME IN A ROTATING WR STAR

E. J. Aldoretta[1], N. St-Louis[1], N. D. Richardson[1], A. F. J. Moffat[1], T. Eversberg[2,3], F. Bolduan[4], F. Díaz[4], P. Dubreuil[4,5], D. Fuchs[4], T. Garrel[4,5], G. Grutzeck[4], G. M. Hill[6], J. Kubát[7], D. Küsters[4], M. Langenbrink[3,4], R. Leadbeater[4,8], D. Li[4], A. Lopez[4,5], R. Maltais-Tariant[1], B. Mauclaire[4], T. Moldenhower[3,4], M. Muñoz[1], H. Pablo[1], M. Potter[4], T. Ramiaramantsoa[1], A. Richard-Laferrière[1], D. Sablowski[4], E. Santos[4], L. Schann[3,4], J. Schmidt[3,4], H. Sieske[3,4], S. Simón-Díaz[9], L. St-Jean[1], J. Strachan[3,4], E. Stinner[3,4], P. Stinner[3,4], B. Stöber[3,4], K. Strandbeck[4], B. Šurlan[7], D. Verilhac[4,5], U. Waldschläger[3,4], D. Weiss[4,5], A. Wendt[4]

To be submitted to Monthly Notices of the Royal Astronomical Society
November 2015

[1]Département de Physique, Université de Montréal, C.P. 6128 Succ. Centre-ville, Montréal, QC, H3C 3J7, Canada
[2]Schnörringen Telescope Science Institute, Waldbröl, Germany
[3]VdS Section Spectroscopy, Germany (http://spektroskopie.fg-vds.de/index_e.htm)
[4]Teide Pro-Am Collaboration
[5]Astronomical Ring for Access to Spectroscopy (ARAS), France (http://www.astrosurf.com/aras/)
[6]W. M. Keck Observatory, 65-1120 Mamalahoa Highway, Kamuela, HI 96743, USA
[7]Astronomický ústav, Akademie věd České Republiky, 251 65 Ondřejov, Czech Republic
[8]Three Hills Observatory, The Birches, Torpenhow, Wigton, CA7 1JF, UK
[9]Instituto de Astrofísica de Canarias, E-38200 La Laguna, Tenerife, Spain

2.1 ABSTRACT

Wolf-Rayet stars have been studied using various methods in order to understand the many physical phenomena taking place in their dense outflows. In the case of variability that is not strictly periodic or for epoch-dependent changes, the challenge is to observe for sufficiently long intervals of time and with a high enough time sampling to be able to understand the underlying phenomena. During the summer of 2013, professional and amateur astronomers from around the world contributed to a 4-month long campaign, mainly in spectroscopy but also in photometry, polarimetry and interferometry, to observe the first 3 Wolf-Rayet stars discovered: WR 134 (WN6b), WR 135 (WC8) and WR 137 (WC7pd+O9). Each of these stars are interesting in their own way, showing a variety of stellar wind structures. The spectroscopic data from this campaign have been reduced and analyzed for the presumably single star, WR 134, in order to better understand its behavior and long-term periodicity in the context of co-rotating interaction regions (CIRs) in the wind. By analyzing the variability of the He II λ5411 emission line, the period of the changes, which we believe is very likely the rotation period of the star, was calculated to be $P = 2.255 \pm 0.008$ days. The coherency time of the variability which we associate with the lifetime of the CIR was deduced to be $\sim$ 40 days, or 18 cycles, by cross-correlating the variability patterns as a function of time. When comparing the grayscale difference images with CIR models, we find that two CIRs were likely present within the wind of WR 134 during our campaign. A separation in longitude of $\Delta\phi \simeq 90^\circ$ was determined between the two CIRs detected and the different maximum velocities that they reach most likely indicate that they emerge from different latitudes as well. We have also been able to detect the CIRs in other spectral lines. Particularly interesting is the detection, for the first time, of a DAC in an optical line (He I λ5876) which confirms the geometry of the CIRs detected in emission. Small-scale structures, or "clumps" also show a presence in the wind, simultaneously with the larger scale structures, showing that they do in fact co-exist.

Keywords: techniques: spectroscopic - instabilities - stars: massive - stars: Wolf-Rayet - stars: individual (WR 134) - methods: data analysis

2.2 INTRODUCTION

Corotating interaction regions (CIRs) form in the winds of hot stars because of a perturbation at the base of the wind, which causes more or less line driving and therefore different velocity flows that collide as the star rotates (Cranmer & Owocki, 1996). This phenomenon was first discovered within the solar wind (Mullan, 1984) and has since been seen in massive-star winds using several different observational methods. The exact cause of these structures could be associated with phenomena at the base of the wind, such as hotter or cooler regions linked with magnetic fields or non-radial pulsations. Most, if not all, O-type stars show Narrow Absorption Components (NACs), which are most likely a snapshot of Discrete Absorption Components (DACs), within their UV P Cygni lines, a clear observational signature of these structures (Cranmer & Owocki, 1996). Conversely, only a few Wolf-Rayet (WR) stars have been shown to have CIRs mainly using optical spectroscopy. Thus far, the only demonstrated examples are WR 1, WR 6 and WR 134 (Chené & St-Louis, 2010; Morel et al., 1997, 1999). Using photometry, spectroscopy and polarimetry it is possible to learn more about the geometry of these features and place constraints on how they are formed.

Morel et al. (1999) studied the variability of the WN6 star WR 134. An intensive spectroscopic and photometric campaign of this star took place in order to reveal the nature of these variations. A coherent 2.25 $\pm$ 0.05 day periodicity in changes of the He II λ4686 emission line was confirmed. The global pattern of variability, however, was found to change with each epoch. While this period was strongly detected within the spectroscopic data, it was only marginally detected in the photometric data (see page 33). Morel et al. (1999) performed simulated line-profile variations caused by the orbital revolution of a local and strong ionized wind cavity from a collapsed companion. They were able to obtain a reasonable fit between the observed and modeled phase-dependent line profiles. However, the predicted X-ray flux from this cavity can only be reconciled with the observed one if the accretion onto the collapsed companion is significantly inhibited, which would then not produce the cavity required to generate the line profile changes. Therefore, these authors conclude that an interpretation based on rotational modulation of a large-scale structure in the wind offers greater consistency with their data. In an attempt to better understand the periodic changes found in the spectroscopic data, we

organized a collaboration between amateur and professional astronomers.

During the summer of 2013, a 4-month WR campaign began on WR 134, WR 135 and WR 137, the first three WR stars discovered by Wolf & Rayet (1867). Each of these targets was chosen in order to observe different features: WR 134 is known to show corotating interaction regions (CIRs) in the spectral lines (Morel et al., 1999), WR 135 is known to have a strongly clumped wind (Lepine et al., 1996) and WR 137 is a long-period WR+O binary system with possible CIRs (Lefèvre et al., 2005). All three of these stars could benefit from long-term observations and are relatively easy for amateurs to observe due to their brightnesses ($V \sim 8.1$, $V \sim 8.1$ and $V \sim 7.9$, respectively). Several types of data were collected, including interferometry from the CHARA Array, optical photometry, broad-band polarimetry and in particular high-resolution optical spectroscopy. Data was collected from 10 unique sites, the majority of which were collected on the island of Tenerife. The spectroscopic data for WR 134 have been analyzed and the results are presented here.

2.3 OBSERVATIONS

In order to better understand the evolution of CIRs in the wind of WR 134, an international spectroscopic campaign was initiated and carried out by professional and amateur astronomers. Several companies have begun producing affordable observing equipment and the amateur community worldwide has begun to utilize spectroscopic techniques, producing exceptional results. The spectrographs designed by the French company Shelyak[10] is one example of a cost-effective tool for astronomers who own their equipment. One of the great advantages of collaborating with the amateur community is the access to long-term observations. With these astronomers located all around the world and their willingness to stay on a single target for several weeks, long campaigns are possible. Communication between all astronomers involved in world-wide projects becomes easy with online amateur communities, such as the Amateur Astronomer Association (VDS; Germany)[11] and the Astronomical Ring for Access to Spectroscopy (ARAS; France)[12]. Due to the telescope and instrument capabilities, however, these intensive campaigns involving

[10]http://www.shelyak.com/?lang=2
[11]http://spektroskopie.fg-vds.de/
[12]http://www.astrosurf.com/aras/

amateur astronomers are only realistic for bright objects.

The previous WR campaign involving a professional and amateur collaboration involved spectroscopic monitoring of the binary system WR 140 for four months during its periastron passage in January 2009 (Fahed et al., 2011), taking place in six locations. This system is well known for its colliding-wind WR+O binary system and has a long orbital period ($\sim$8 years) along with a high eccentricity ($\sim$ 0.9). Fahed et al. (2011) were able to provide updated orbital parameters of this system, along with new estimations for the WR and O star masses and new constraints on the mass-loss rates and the colliding-wind shock cone. This collaboration is an example of how valuable amateur data are for massive star research. The radial velocity curve obtained during this campaign is reproduced in Figure 2.1.

The data collected for this project were taken by a large group of astronomers from 25 May 2013 to 06 October 2013. Ten different observatories contributed to the spectroscopic data for these three WR stars, six of which are professional facilities. The majority of the data were collected at the Teide Observatory of the Instituto de Astrofísica de Canarias (IAC) in Tenerife using the 0.8m telescope and an echelle spectrograph combined with a fiber-fed CCD, both supplied by Berthold Stöber. This facility houses several telescopes, while all other equipment (spectrograph, CCD and computer) must be supplied by the observing group. The remaining amateurs collected the data using their own telescopes and single-grating spectrographs in several locations around the world: U.K. (John Strachan, Robin Leadbeater[13]), China (Dong Li) and Maryland, U.S.A. (Mike Potter).

The remaining data were collected at five professional observatories: (1) the Nordic Optical Telescope (NOT) located at Roque de los Muchachos Observatory, La Palma in the Canary Islands, (2) the Dominion Astrophysical Observatory (DAO) in British Columbia, Canada, (3) the Ondřejov Observatory of the Astronomical Institute of The Czech Academy of Sciences in the Czech Republic, (4) the Observatoire du Mont-Mégantic (OMM) located in Québec, Canada and (5) the Keck Observatory located in Hawai'i, USA. All observers participating in the campaign observed at least the He II λ5411 emission line where the CIR perturbations can be easily detected due to the strength of the line along with its relative isolation. Table 2.1 provides the instrument information for each

[13]http://www.threehillsobservatory.co.uk/astro/astro.htm

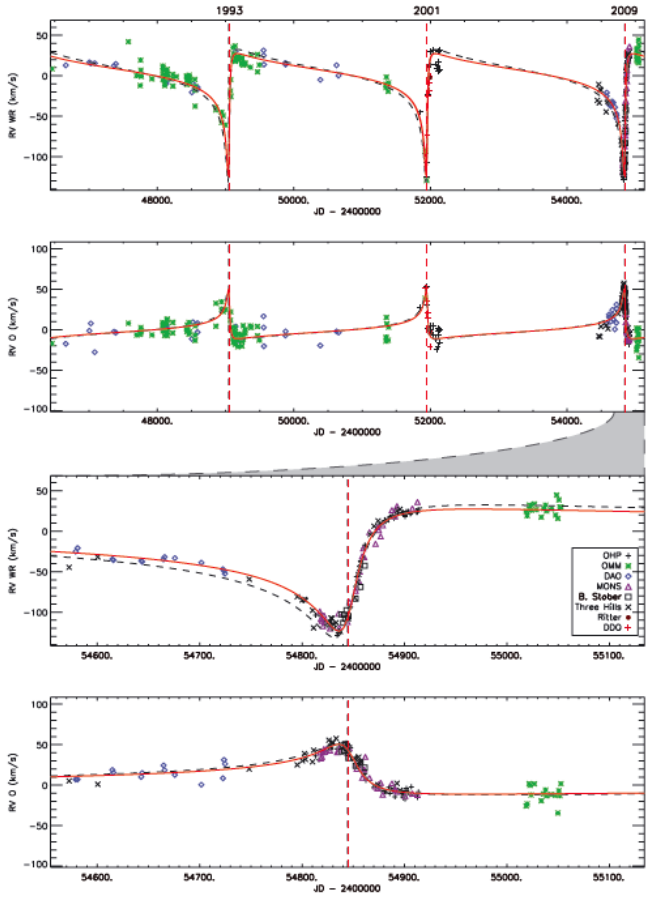

Figure 2.1: Top two panels show measured radial velocities of the WR star of WR 140 and its O-star companion with the fit for the orbital solution (solid line). The data from the 2001 periastron passage is also included, with the black dashed line indicating the 2001 orbital solution. The dashed vertical lines show the position of the new periastron passage. Bottom two panels show the same plots that are zoomed on the 2009 campaign. The legend indicates where each data point was obtained. (Fahed et al., 2011)

Observatory	Telescope	Spectrograph	CCD
Professional Facilities			
OMM	1.6m	Cassegrain	STA0520 Bleu
DAO	1.8m	Cassegrain	SITe-2
NOT	2.5m	FIES	EEV 2k x 2k
Ondřejov	ZEISS (2m)	Coude700 eshel	PyLoN 2048x512 BX
Keck	Keck II (10m)	ESI	MIT-LL W62C2
Teide	0.8m	eshel	Nova3200
Amateur Contributors			
Potter	C14 (0.36m)	LHIRES III	SBIG ST-8
Li	C11 (0.28m)	LHIRES III	QHYIMG2P
Strachan	0.25m	LHIRES III	ArtemisHSC
Leadbeater	C11 (0.28m)	APLY 600	ATIK-314L+

Table 2.I: List of each observatory that contributed to the campaign along with corresponding telescope, spectrograph and CCD information.

observatory.

2.4 DATA REDUCTION

All datasets for this campaign were analyzed by a single person (E.A.), allowing for any issues to be handled in a uniform manner. Each observer provided a set of dark, bias and flat field images each night along with a comparison image after each exposure for wavelength calibration. A discussion of the reduction process for both the professional and amateur data will follow. Table 2.II provides the information on the final reduced spectra for each observatory. A total of 395 spectra of WR 134 were used for this study.

2.4.1 Professional Data

While the Teide data provided the majority of the spectra for this campaign, several professional observatories also contributed. Two separate observing runs took place at OMM during the months of July and September/October. For the July data, a 1200 grooves mm^{-1} grating was used with the single-slit Cassegrain spectrograph, resulting in a resolving power of $\sim$ 5,300. These images were obtained in three groups of 3 x 300s and wavelength calibrated using both a Neon (Ne) and a Helium-Argon (HeAr) emission

spectra due to the broad wavelength coverage. The second data set from OMM was taken with a 2160 grooves mm^{-1} grating, limiting the wavelength range but increasing the overall resolving power to $\sim$ 7,000. A Copper-Helium-Argon lamp was used for the wavelength calibration. All of these data were reduced using the standard IRAF[14] reduction package. Both datasets had an average S/N of $\sim$ 350 per resolution element after each group of 3 spectra were combined.

Ondřejov Observatory provided 21 spectra of WR 134. Each target had 3 - 4 spectra obtained ($\sim$ 900s each) which were later combined for a higher S/N ratio. Each night, a telluric standard spectrum was also observed (ζ Aql), along with bias, dark and flat field frames. The standard IRAF reduction package was utilized to correct for these effects and a ThAr spectrum was used for the wavelength calibration. The remaining professional data (NOT, DAO and Keck) were sent having already been bias, dark and flat-field corrected with only the normalization needed before the measurements could begin. All these data were normalized using the same continuum regions as the amateur data. Figure 2.3 shows a superposition of the 395 spectra of WR 134 in the wavelength region surrounding the He II λ5411 line.

2.4.2 Amateur Data From the Teide Observatory

The largest source of optical spectroscopy came from the Instituto de Astrofísica de Canarias 0.8m telescope located at the Teide Observatory. Having several observing teams resulted in a nearly continuous four-month run. An *eShel* spectrograph[15] was installed on the telescope, along with a Nova3200 CCD. Spectra were recorded in groups of 3 x 600s exposures, allowing for a signal-to-noise (S/N) of 200 per resolution element or better near the center of a given order. The S/N on the edge of each order, however, was significantly lower than in the center due to a decrease in sensitivity at the detector's edge. Once the groups were combined, a total of three exposures of each campaign star were obtained each night, along with a spectrum of Regulus (B8IVn, $v = 1.4$) or ζ Aquilae (A0IV - Vnn, $v = 2.99$). These two stars were used to determine the blaze function and telluric

[14]IRAF is distributed by the National Optical Astronomy Observatory, which is operated by the Associated Universities for Research in Astronomy, Inc., under cooperative agreement with the National Science Foundation.

[15]http://www.shelyak.com/dossier.php?id_dossier=47

Observatory	**HJD - 2,450,000**	N_{spec}	**Resolving Power** $\left(\frac{\lambda}{\Delta\lambda}\right)$	λ **coverage (Å)**	**S/N**
Professional Facilities					
OMM (1)	6485 - 6496	19	5,300	4500 - 6700	350
OMM (2)	6561 - 6567	19	7,000	4750 - 6000	350
DAO	6473 - 6482	58	5,500	5100 - 6000	350
NOT	6468	1	11,800	3500 - 6800	350
Ondřejov	6452 - 6549	21	10,000	5200 - 5800	300
Keck	6517	3	13,000	4000 - 10000	300
Teide	6438 - 6550	184	10,500	4500 - 7400	250
Amateur Contributors					
Potter	6443 - 6572	36	7,500	5300 - 5900	200
Li	6489 - 6563	27	5,300	5200 - 5600	200
Strachan	6496 - 6505	17	5,300	5300 - 5700	200
Leadbeater	6484 - 6507	10	5,300	5200 - 5600	200

Table 2.II: List of each observatory that contributed to the campaign, including the corresponding HJD interval at which the spectra were taken, the total number of spectra, the resolving power, the wavelength coverage and the average S/N ratio. The two rows for OMM represent the two separate runs, each using different gratings. The information listed for the Keck data is only including the 6^{th} order in which the He II λ5411 line is present.

contamination in the regions of interest.

The raw frames showed that $\sim$ 10 - 20% of the images on a given night had readout errors. These errors presented themselves as a rectangular portion of the upper chip being placed on the opposite side. In order to correct for this effect, a median dark frame was created which was constructed from 10 - 25 unaffected dark frames on the same night. More hot pixels were present than normally seen in CCDs cooled with nitrogen due to the electronic cooling system, with at least 5 - 10 per row. This allowed for a cross-correlation to be performed in a row-by-row analysis, recovering and re-assembling the images correctly for reduction (see Figure 2.2). The new images were then reduced using standard echelle spectroscopy routines in IRAF, where the data were corrected for bias, dark, and flat fielding effects. The images were wavelength calibrated using Thorium-Argon (ThAr) emission spectra taken before and after each observation. This resulted in a well defined wavelength solution which was checked against known diffuse interstellar bands and telluric absorption lines. In total, 184 spectra were obtained of WR 134 at Teide between 25 May 2013 and 14 September 2013, spread over 91 nights, contributing roughly half of the spectroscopic data.

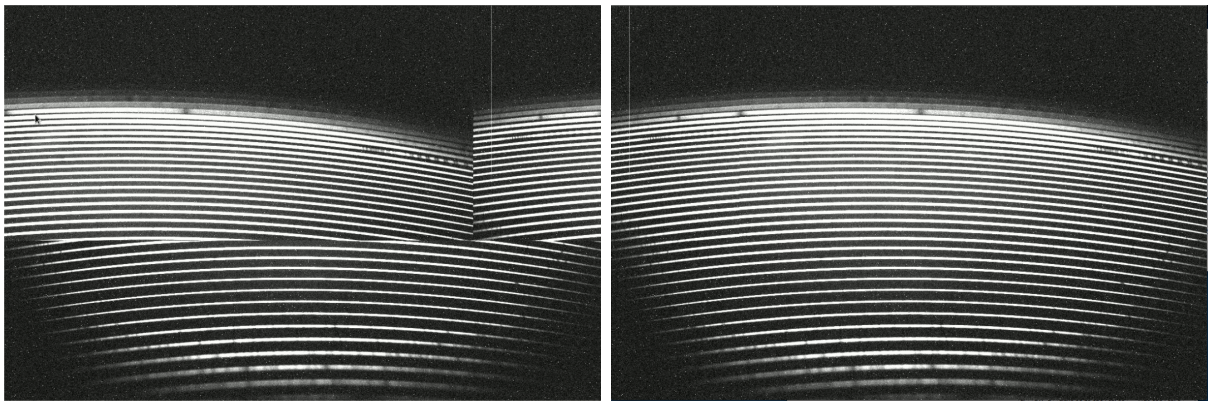

Figure 2.2: The left image shows the Teide data before the correction was applied, while the right images shows after correction.

2.4.3 Other Amateur Data

The additional amateur data (observers: Potter, Li, Strachan and Leadbeater) were all reduced in a similar manner. Each observer provided the necessary calibration frames

(bias, dark and flat) to run the reduction packages in IRAF. Spectra of telluric standard stars (either Regulus or ζ Aql) were also provided by the amateurs for each night of their observations. ThAr emission spectra were taken for wavelength calibration. Several exposures of WR 134 were obtained each night, which were combined in order to reach an average S/N ratio of $\sim$ 200 per resolution element. Each exposure lasted between 600 - 3600s depending on the observer and their instruments. The resolution for these instruments ranged between $\sim$ 5,300 - 7,500 using 1200 grooves mm^{-1} gratings. These setups and exposure times allowed for the high S/N needed in order to detect the CIRs moving across the line. The wide variety in resolving powers resulted from the difficulty in obtaining a good collimator focus for an LHIRES III spectrograph. All spectra of WR 134 were normalized around the following continuum regions: 5305 - 5340 Å, 5540 - 5629 Å and 6755 - 6775 Å. In total, the additional amateur astronomers contributed 90 spectra, filling in data gaps from Teide and the professional observatories, allowing for almost continuous coverage during this campaign.

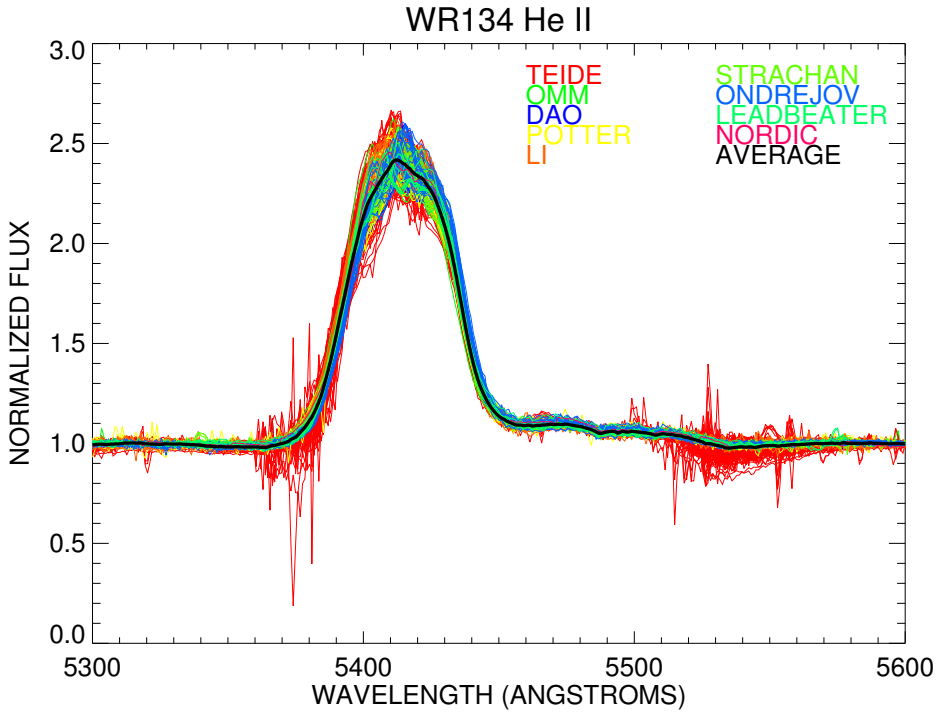

Figure 2.3: Superposition of all 395 spectra obtained around He II λ5411. Different data sources/observers and an average profile are shown related to the plot legend. The noise in the Teide data (red) is due to the edges of the echelle orders.

2.5 MEASUREMENTS

In their extensive study of WR 134, Morel et al. (1999) made several measurements involving the various moments of the spectral lines to characterize the spectroscopic variability. We made similar measurements on our dataset. However, before any calculations could be made, the spectra were rebinned on a log λ, heliocentric wavelength scale to a spectral resolution of $R = 6,300$. Once all the spectra were properly rebinned, we constructed grayscale images of the differences from the mean as a function of time for the spectral region around the He II λ5411 emission line. Variability is clearly detected, as can be seen in an example presented in Figure 2.4. By calculating the moments of this line, the exact period of the spectral variability can be measured on both short and long timescales.

2.5.1 Calculating Moments

Statistical analysis plays a major role in determining the shapes of emission lines. Both large and small scale variabilities that are present in WR winds have different effects on these broad lines and their symmetries over time. With the presence of a corotating interaction region (CIR) having been previously found (Morel et al., 1999), the 4-month spectroscopic data were expected to show these large features moving across the top of the He II λ5411 emission line. Calculating the normalized, low-order moments are an effective way to characterize the global shapes of the spectral lines. The central n^{th} moment can be calculated by

$$\mu_n = \frac{\Sigma_j(\lambda_j - \bar{\lambda})^n I_j}{\Sigma_j I_j}, \tag{2.1}$$

where

$$\bar{\lambda} = \frac{\Sigma_j \lambda_j I_j}{\Sigma_j I_j}, \tag{2.2}$$

with I_j being the intensity of the line, j being the summing index across the line profile and λ_j is the wavelength. Two dimensionless quantities can be calculated from these moments: the Skewness by $\mu_3/\mu_2^{3/2}$ and the Kurtosis by μ_4/μ_2^2. While the skewness defines the line asymmetry from the central wavelength, the kurtosis measures how peaked the line is. These, along with several other quantities, were calculated for each spectrum in the entire dataset for the λ5360 - 5455 Å wavelength region. The mean skewness and the standard

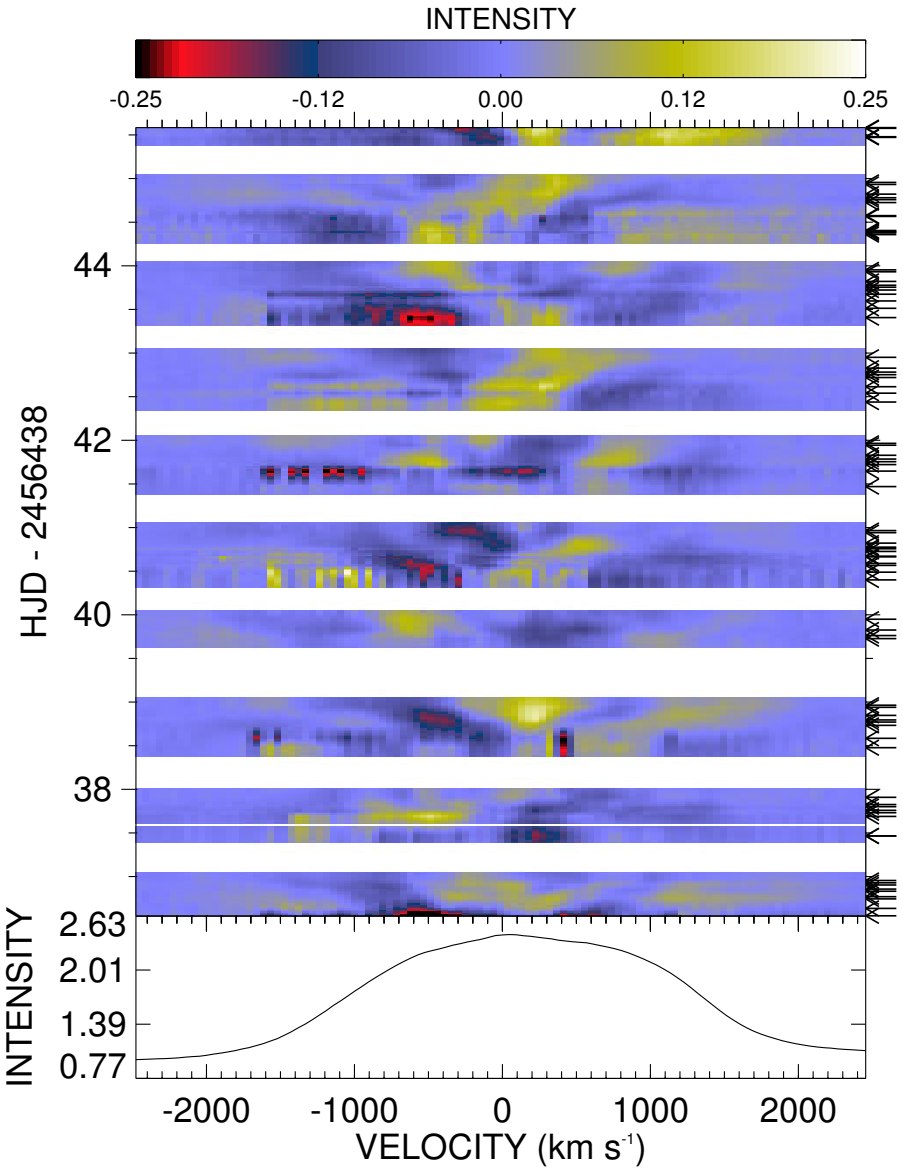

Figure 2.4: A difference plot from the mean He II λ5411 spectrum for a sample of the dataset. The top panel shows the intensity scale while the bottom panel shows the mean spectrum in velocity space. The arrows indicate the location of each spectrum in time. The starting HJD is the beginning of the campaign. The remaining difference plots can be found in Appendix I.

deviation from the mean, which gives an idea of the variability level, is -0.186 ± 0.016, while the mean kurtosis and standard deviation gives 2.231 ± 0.013. The equivalent width (EW), flux-weighted velocity, the bisector and the full width at half maximum (FWHM) were also calculated in the same wavelength region for each spectrum. The EW measurements were calculated by integrating the function $(1 - I_j)$, with I_j being the rectified line flux. A mean value and standard deviation of -61.67 ± 2.34 was found. The flux-weighted velocity (km s^{-1}) of the emission line was calculated using

$$v_{flux} = \frac{\bar{\lambda} - \lambda_0}{\lambda_0} c, \tag{2.3}$$

where $\bar{\lambda}$ is defined in Eq. 2.2 and λ_0 is the rest wavelength of the transition (5411.524 Å). The mean value gives -73.62 km s^{-1} with a standard deviation of 11.25 km s^{-1}. For the bisector and FWHM calculations, the velocity at each wavelength was determined, with the rest wavelength at $v = 0$. These velocity values were then linearly interpolated with the normalized flux values for both the red side (-3000 to 0 km s^{-1}) and the blue side (0 to $+3000$ km s^{-1}) of the emission line. The bisector was calculated by

$$B = \frac{(v_r + v_b)}{2}, \tag{2.4}$$

where v_r and v_b represent the velocity values on the red and blue side of the line with a mean value over the normalized line flux interval from 1.0 to 1.4 of 143.16 and a standard deviation of 34.09 km s^{-1}. The FWHM values (mean of 2932.40 km s^{-1} and standard deviation of 59.66 km s^{-1}) were determined by subtracting the interpolated velocity values on the red side of the line from the values on the blue side of the line at a rectified flux level of 1.4. A complete table of these values (EW, skewness, kurtosis, flux velocity, bisector and FWHM) for each spectrum can be found in Appendix II.

2.5.2 Period Search

From each of these five series of measurements, a Scargle (1982) periodogram was calculated to search for a periodicity within the variability of these quantities. Figure 2.5 shows these periodograms as a function of time, using 10-day intervals, for the entire dataset. While the values of the detected periods for each of the five moments are seen

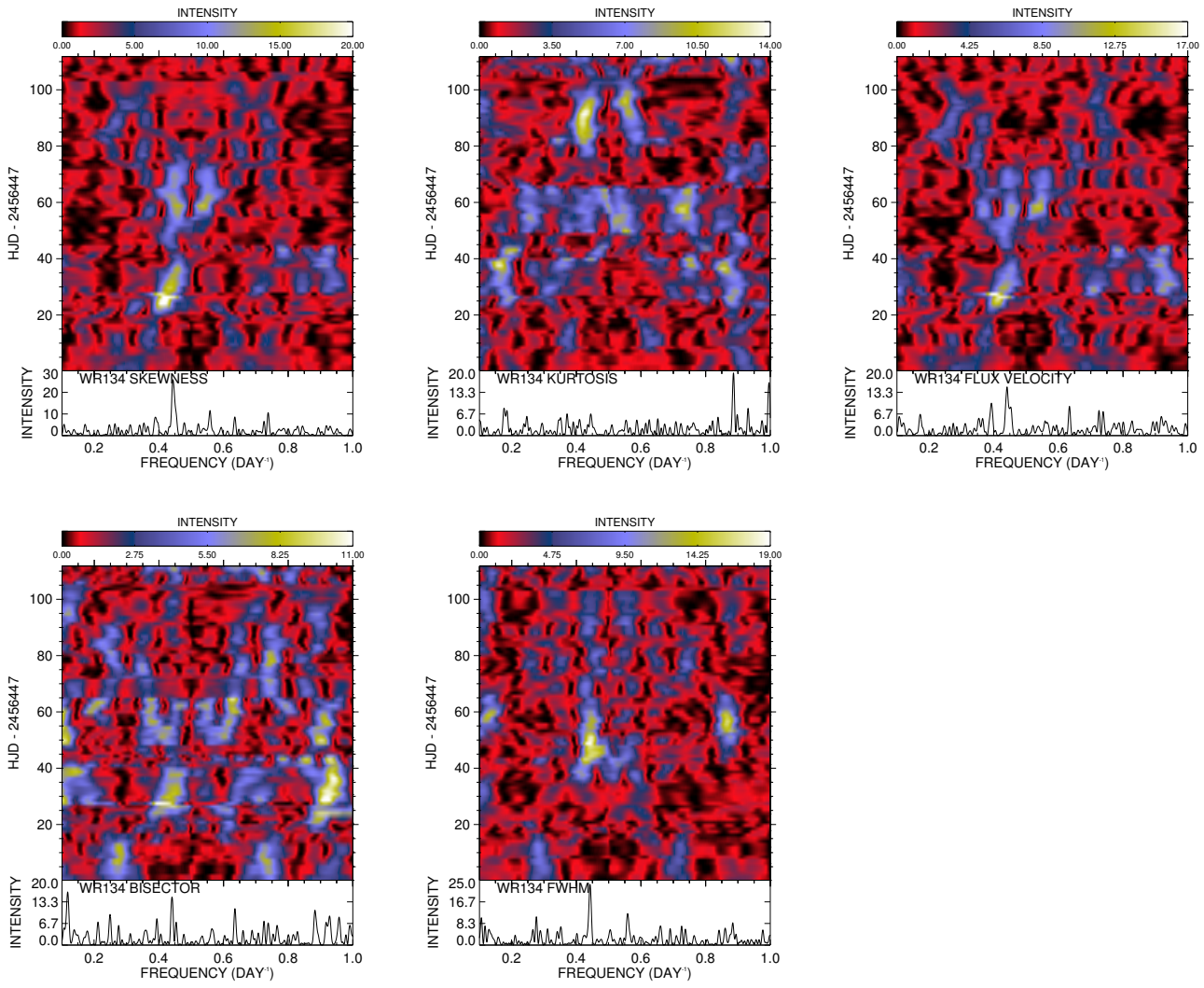

Figure 2.5: Time-dependent Scargle analysis for the Skewness, the Kurtosis, the flux-weighted velocity, bisector and FWHM of the He II λ5411 emission line. The bottom panels show the Scargle periodogram for the entire dataset while the top panels show the Scargle analysis as a function of time using $\sim$ 10-day bins.

to fluctuate over the four month time frame, there are clear time intervals that show stronger intensities. Along with a Scargle analysis, a period was searched for using a phase determination minimization (PDM) analysis (Stellingwerf, 1978). Table 2.III lists the average period found using these two methods for each of the five measurements calculated. The overall average period was calculated to be $P = 2.255 \pm 0.008$ days using all ten Scargle and PDM values previously determined.

Moment	**Scargle analysis (day^{-1})**	**PDM analysis (day^{-1})**
Skewness	0.4452	0.4451
Kurtosis	0.4432	0.4450
Flux Velocity	0.4449	0.4437
Bisector	0.4418	0.4409
FWHM	0.4427	0.4428

Table 2.III: List of the five measurements for both a Scargle (1982) and PDM (Stellingwerf, 1978) analysis.

Once the overall period was determined using the measurements of the He II λ5411 emission line, we calculated a 2-dimensional Scargle (1982) periodogram for this line in velocity space. This analysis shows that a frequency of ~ 0.4435 day^{-1} ($P = 2.255$ days) has the strongest peak across most of the profile, as can be seen in Figure 2.6. Along with the strongest frequency, both its first harmonic ($2f$) and their aliases, (1 - f) and (1 - $2f$), have strong peaks as well. Morel et al. (1999) created a similar CLEANed 2-dimensional power spectrum (PS) around the He II λ4686 emission line. Their results showed that their highest frequency peak was ~ 0.444 day^{-1} ($P = 2.25 \pm 0.05$ days). We were able to confirm this period within the errors to a more precise value. Each of the five measurements were then phased according to our 2.255-day period (P):

$$phase = \mod \left[\frac{t - t_0}{P}\right], \tag{2.5}$$

with t_0 being the first day of the campaign (HJD 2456438) as the arbitrarily assigned origin of the phases. To illustrate the phase-dependent behaviour of the five measured quantities, we plot in Figure 2.7 the measurements phased to this period for two sets of 5 cycles of the dataset. It can be seen that the skewness values display a single sine curve

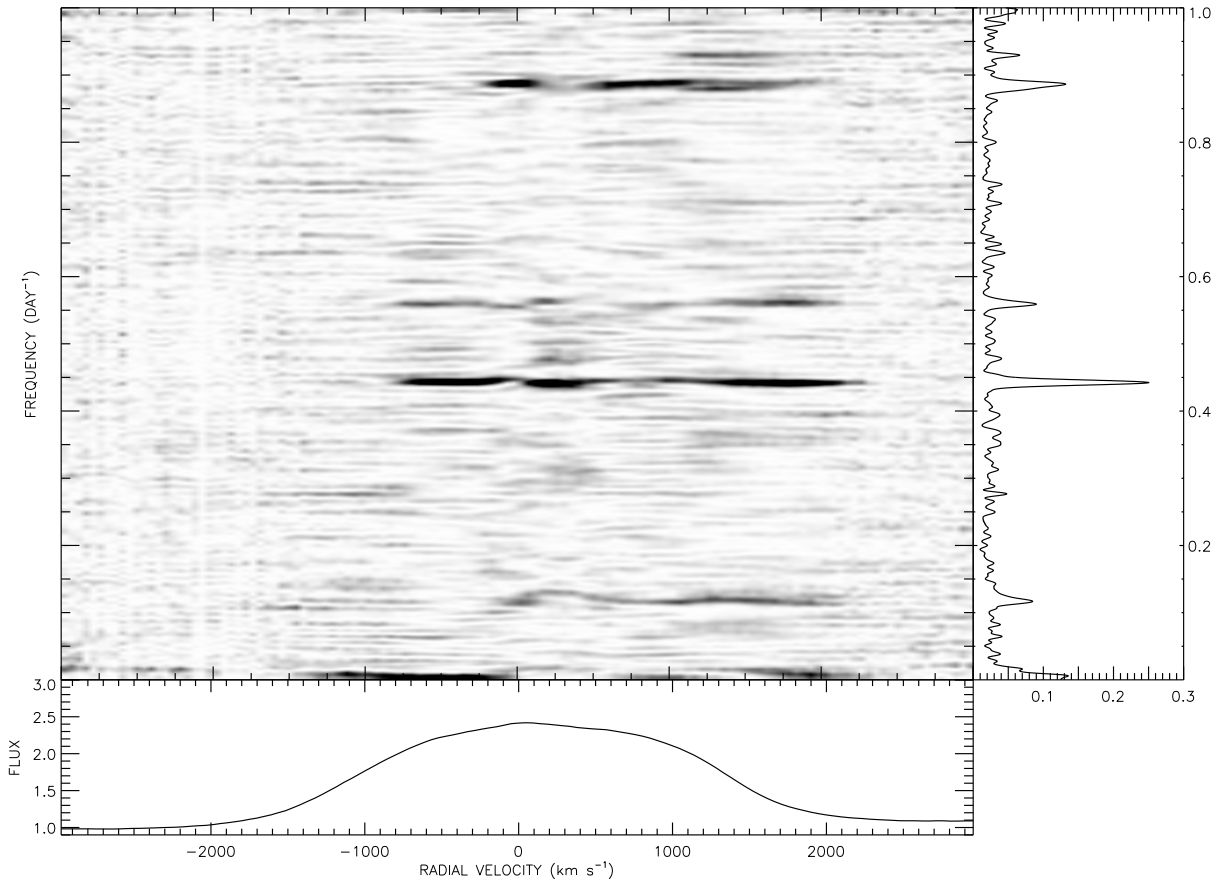

Figure 2.6: The 2-D Scargle (1982) periodogram around He II λ5411 line. The bottom panel shows the average spectrum of the entire dataset while the right panel shows the Scargle periodogram averaged over the entire line. The middle panel shows the grayscale of the Scargle analysis for each velocity bin. It can be seen that the frequency of ~ 0.4435 is the strongest peak.

with phase, which is expected for this calculation for one sub peak moving from one side of the profile to the other. On the other hand, Figure 2.7 also shows that the kurtosis values display a double sine curve, which is also expected for one rotation in the same situation. The equivalent width (EW) values were also calculated for this emission line and the scatter is clearly above the typical error bar. The measurements did not show any trend with phase, as can be seen in Figure 2.8.

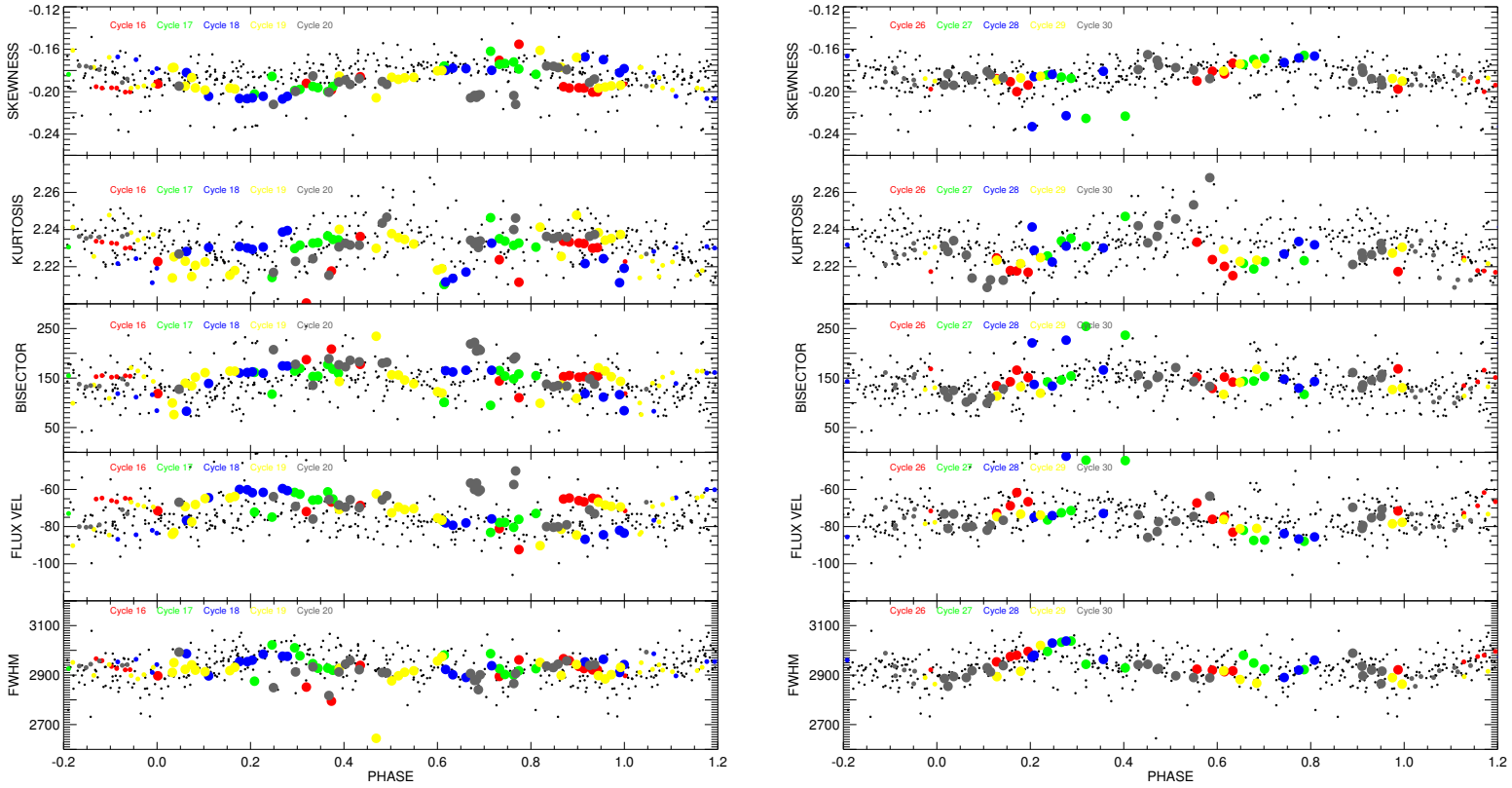

Figure 2.7: The phased measurements for certain cycles using the 2.255-day period. Each panel shows all 395 measurements as small black dots for each moment, while also showing certain cycles as colored dots (see legends). The smaller colored dots represent the overlapping phase. The remaining phased moments for the entire dataset can be found in Appendix III.

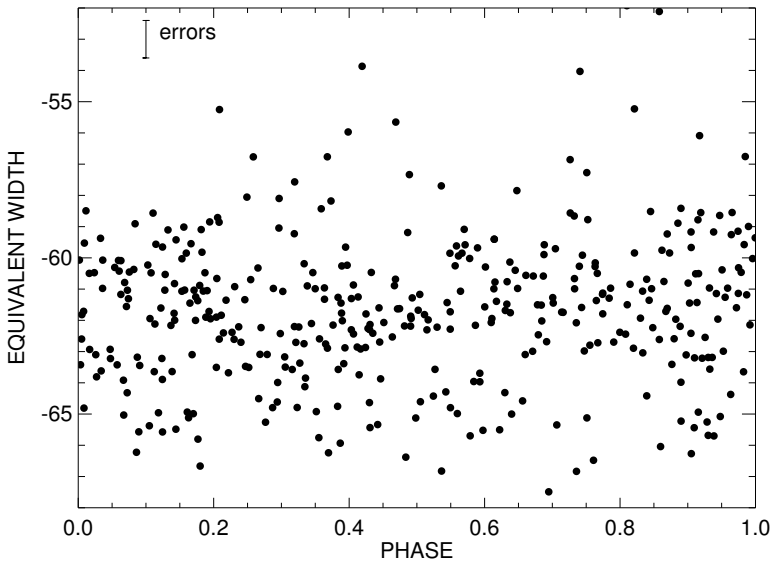

Figure 2.8: The EW measurements of the He II λ5411 emission line plotted as a function of phase using the 2.255-day period for all spectra in our dataset. The average calculated error for these values is displayed.

2.6 RESULTS

Along with the moments, the spectra for the entire dataset were phased on the 2.255-day timescale. Figure 2.9 shows how the intensity of the line changes with phase. There is a strong CIR present within this line, spanning a velocity range of −600 to 600 km s^{-1} and describing a single sinusoid per cycle (hereafter referred to as the "central" CIR). However, there also appears to be another CIR present within this line, which extends out to $\sim$ 1500 km s^{-1} from phase 0 - 0.35. This feature and the central CIR reach peak velocities at different phases with a shift of Δphase $\sim$ 0.25, which indicates that they are, in fact, located at different longitudes on the star with a separation of $\Delta\phi \simeq 90°$. Note that because we are using differences from the mean in these grayscale plots, each feature in emission is associated with a feature in absorption at any given wavelength of velocity. This leads to what we could call a *shadowing effect*, i.e. each bright trace is accompanied by an associated dark trace, which gives the plot a characteristic appearance. In the next section, we present an analysis conducted on the dataset to search for changes within the phased grayscale image with time.

2.6.1 Cross-Correlation Analysis

In order to determine if any changes occurred within the central CIR over the timespan of the campaign, a cross-correlation analysis was conducted on several phased grayscale images (similar to Figure 2.9). For every 5 days ($\sim$ 2 cycles), a new phased grayscale image was created, for a total of 23 for the entire data set. Three arbitrary grayscale reference images were chosen, from which a normalized 2-dimensional cross-correlation function (CCF) was calculated from the images before and after the reference image. The correlations were quantified using

$$XC_{i'i} = \frac{\Sigma_{jk} I_{i'jk} \times I_{ijk}}{\Sigma_{jk} I^2_{i'jk}}, \tag{2.6}$$

with i' referring to the fixed image, while j and k refer to the pixel locations. The three reference images were chosen based on their good phase coverage. Figure 2.10 displays the value of $XC_{i'i}$ as a function of time using the three difference reference images. Once the cross-correlation analysis was carried out for each reference image, a Gaussian function

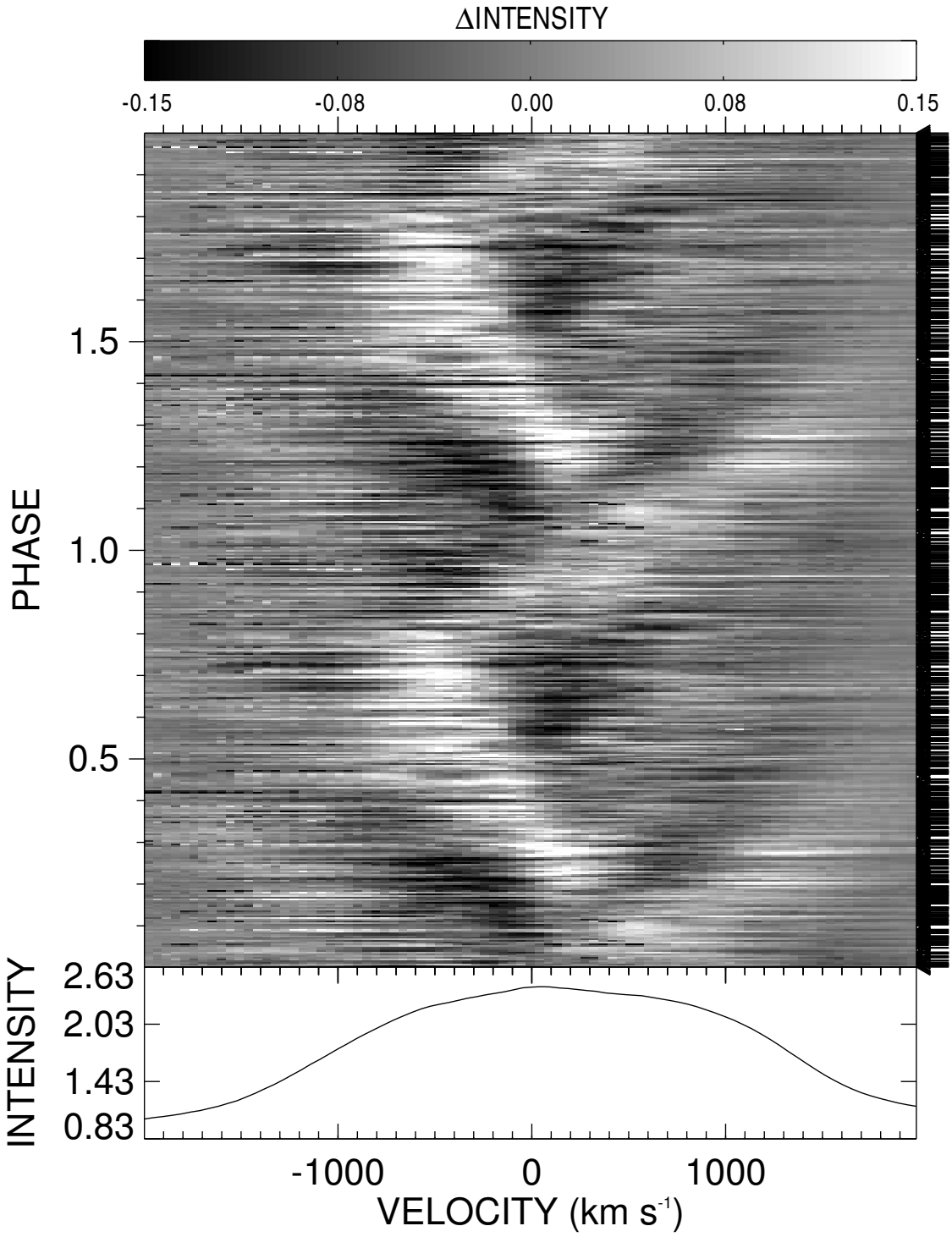

Figure 2.9: The phased difference spectra for the entire dataset using the 2.255-day period. The top panel shows the grayscale difference image from the mean of the phased spectra, while the bottom panel shows the mean spectrum of the He II λ5411 line in velocity space for the entire campaign.

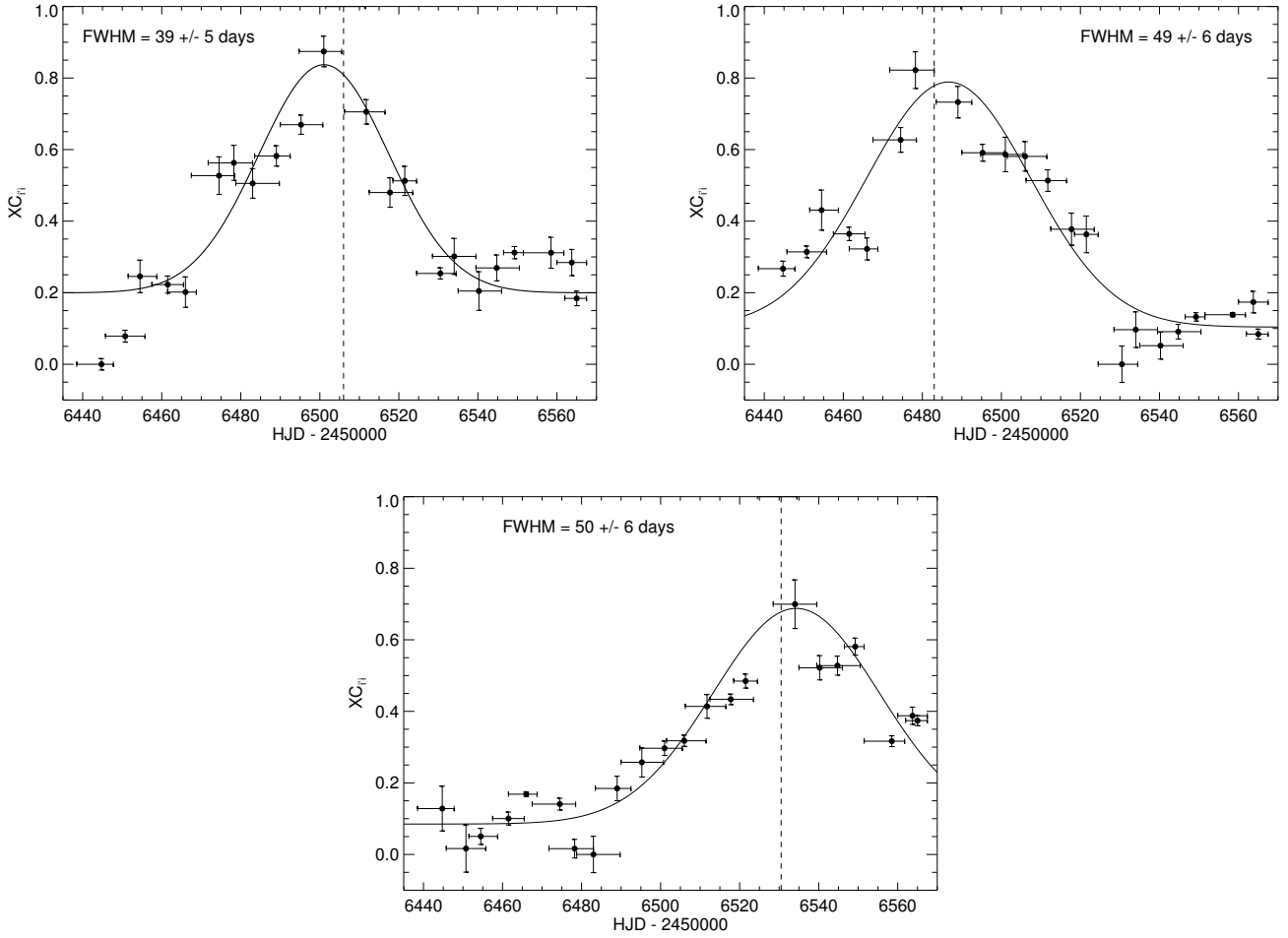

Figure 2.10: The cross-correlation analysis for each of the three reference images (*dashed vertical line*). The x-axis error bars show the time covered by each image, while the y-axis error bars display the $XC_{i'i}$ errors. The solid line is the Gaussian function that was fitted for each analysis.

plus a constant background was fit to the ensemble of data for a given reference image, ignoring the artificial correlation of the i' image with itself (i.e. for $i = i'$). The average FWHM for the three separate Gaussian fits is $\sim$ 40 days ($\sim$ 18 cycles). This value can be interpreted as the length of time for which the variability pattern, as seen in the grayscale plots of the difference spectra, remains constant. After this time, these grayscale plots look significantly different and are considered uncorrelated.

Following this result, a set of phased grayscale difference images was created for the dataset in 40-day segments for a total of 3 images. These images are presented in Figure 2.11, which illustrates clearly the coherence timescale of $\sim$ 40 days. Indeed, it is immediately clear that the three images have significantly different aspects. One can clearly see the main CIR in the central image, but for the last 40-days of the campaign, the main CIR is no longer a strong presence in the He II λ5411 line.

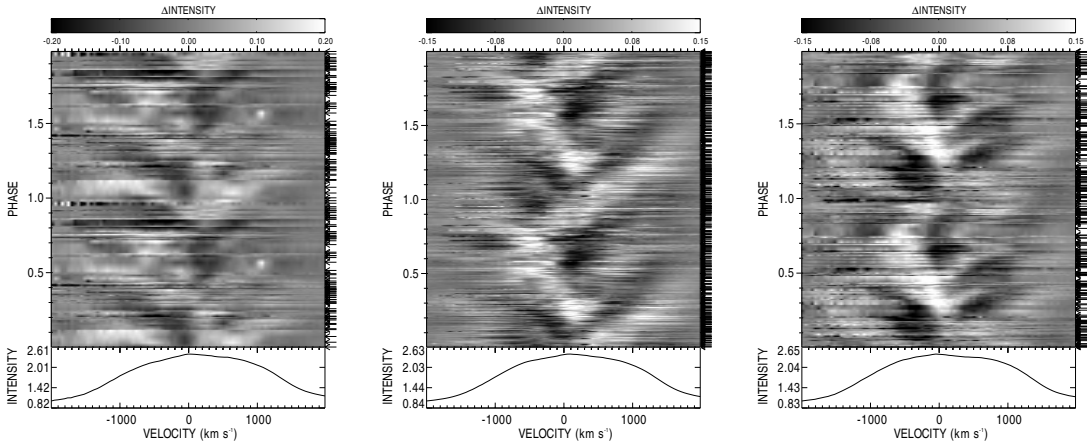

Figure 2.11: Examples of difference grayscale images of the spectra. The images are increasing with time from left to right and are grouped in 40-day (18 cycle) segments.

2.6.2 Comparison with Theoretical Calculations

Dessart & Chesneau (2002) used the radiation hydrodynamical model of Cranmer & Owocki (1996) to generate synthetic emission-line profiles resulting from two CIRs created as a consequence of the presence on the surface of the star of two bright spots located at opposite longitudes at the base of an optically thin, radiatively-driven stellar wind. Examples of these profiles are displayed on the left side of Figure 2.12 for two

different inclinations with respect to the line-of-sight. Our grayscale difference image for the entire campaign is reproduced on the right side of Figure 2.12 for comparison purposes. Although the model was reproduced for a system with two CIRs with a 180° separation, our difference image clearly shows a similar brightness pattern, strongly suggesting that this is a reasonably good model to represent the observations. The images used to create the middle phased grayscale difference plot in Figure 2.11 were used to determine the kinematics of the CIR in the wind due to their intense phase coverage.

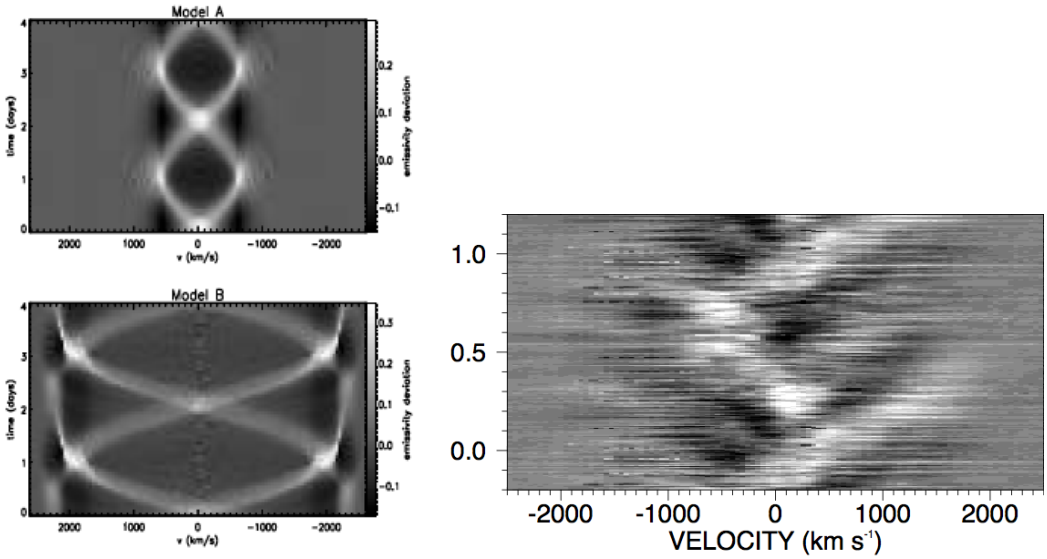

Figure 2.12: The left panel shows the image of the model created by Dessart & Chesneau (2002) for two CIRs with a 180° separation within WR-star winds for both (A) a 20° and (B) a 70° inclination angle of the rotation axis of the star with respect to the line-of-sight. The right panel displays the difference image used to determine the kinematics of the central CIR from the data presented in this paper. It can be seen that more than one CIR is present within the wind of WR 134 with different inclination angles.

2.6.3 Kinematics of the CIR

In order to better understand more about the movement of the central CIR in the wind of WR 134, its velocities were measured using the difference spectra used to create the second image shown in Figure 2.11 (HJD 2456478 - 2456518). First, a total of 20 new difference spectra were created by binning the original difference spectra to increase the S/N of each spectra (see Table 2.IV for number of spectra in each bin). Then a Gaussian

function was fit to each binned spectrum using

$$f(x) = A_0 e^{-z^2/2}, \tag{2.7}$$

where

$$z = \frac{x - A_1}{A_2}, \tag{2.8}$$

with A_0 being the height of the Gaussian, A_1 its center, A_2 its width and x the velocity calculated for the He II λ5411 emission line. The rest velocity of this transition was used as the zero point for each fit. Each of these Gaussian fits established the velocity of the peak of the difference spectrum, indicating where the CIR was present within the emission line. In order to distinguish between the multiple CIRs when present, each peak was chosen by eye using the second grayscale image in Figure 2.11 to ensure the correct velocities were calculated. Table 2.IV lists each velocity that was determined using this method, along with the corresponding phase, the number of spectra per bin and the weight of each bin (based on the inverse of the velocity errors determined by the Gaussian fitting).

Once the velocities of the central CIR were determined for these binned spectra, a sinusoidal curve was fit to the data, showing how the apparent velocity of the central CIR changes with phase as the star rotates. Figure 2.13 shows this fitted curve with the binned spectra while Figure 2.14 shows the curve overplotted on the difference grayscale images (from Figure 2.11). If i is the angle between the stellar rotation axis and the line of sight and β is the angle between the rotation axis and the CIR, assuming it emerges radially, then the angle between the velocity vector of the gas in the CIR and the observer at time t is

$$\cos\theta(t) = \cos i \cos\beta + \sin i \sin\beta \cos\left(\frac{2\pi t}{P}\right), \tag{2.9}$$

where P is the rotation period and where we have assumed that the maximum velocity is reached at $t = 0, P, 2P, ...$

At any given time, the velocity of the excess emission peak will be $v_{e(t)} = v_{CIR}\cos\theta(t)$. Note that v_{CIR} is not necessarily the terminal velocity of the wind. Indeed, as predicted by Cranmer & Owocki (1996), for a bright spot the velocity of the gas in a CIR, although mainly radial, can be considerably smaller than the unperturbed wind velocity. Note that, in principle, Eq. 2.9 is the function we should have fit to the v_e values instead of a simple

Phase	$\mathbf{V}_{obs}$	$\mathbf{N}_{spec}$**/bin**	**Weight**
0.025442132	952.84492	8	0.05
0.071805760	415.57481	8	0.18
0.12431499	581.53620	12	0.11
0.17151666	264.81918	11	0.15
0.22482750	38.044514	9	0.04
0.27846556	-604.05684	7	0.07
0.32430017	64.717880	8	0.05
0.37973759	-437.83476	9	0.12
0.42328038	-580.20040	8	0.06
0.47394798	-493.45871	9	0.15
0.52947549	-484.65148	10	0.38
0.62375542	-509.14667	7	0.09
0.67820033	-539.91494	9	0.12
0.72471388	-47.382968	6	0.07
0.77003406	315.16239	10	0.05
0.82561179	300.43825	7	0.12
0.87619053	156.46829	8	0.04
0.92691676	693.14553	12	0.06
0.97241153	732.93838	11	0.08

Table 2.IV: The list of the phases, observed velocities (km s^{-1}), number of spectra in each bin and the weight of each bin inputted into the FORTRAN code *sbcm* for calculating the kinematics model.

sinusoid. However, carrying out a proper fit is outside the scope of this paper. It should be done using hydrodynamic calculations like those of Cranmer & Owocki (1996) to accurately capture the velocity distribution of the gas in the CIR and its density distribution within the curved pattern.

Nevertheless, inspection of Figure 2.9 leads us to several conclusions. First, since the maximum velocity of the two CIRs we detected are different, they either emerge at different angles from the rotation axis or they have a different velocity (v_{CIR}). Also, the median velocity of the main CIR is very close to $v = 0$. This indicates that either this CIR is located at $\beta = 90°$ or that inclination of the rotation axis is 90°. Since the second CIR is only partially detected, we are unfortunately not able to confirm if the latter interpretation is the correct one. Note finally that as mentioned previously, because the maximum velocity of these two CIRs is not reached at the same phase, we can conclude that they do not emerge from the same longitude on the star. From the phase difference, we found that they are separated by $\simeq 90°$.

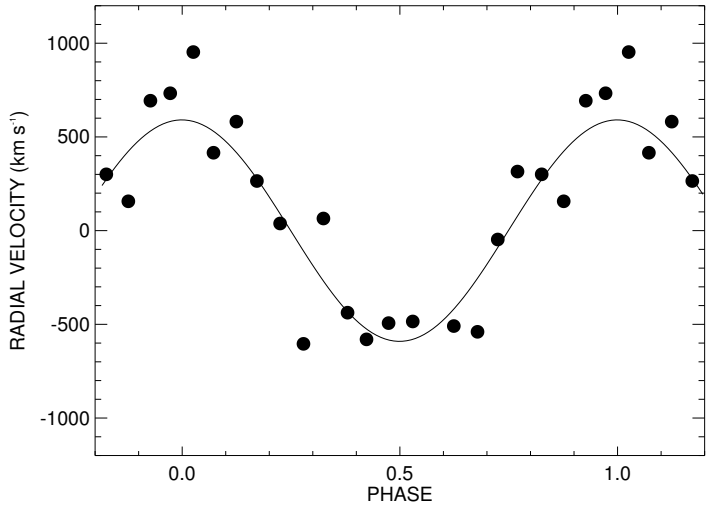

Figure 2.13: Radial velocity versus phase for the central CIR seen during one 40-day segment in Figure 2.10. The points represent the observed velocities calculated for the binned difference spectra with the sinusoidal fit overplotted.

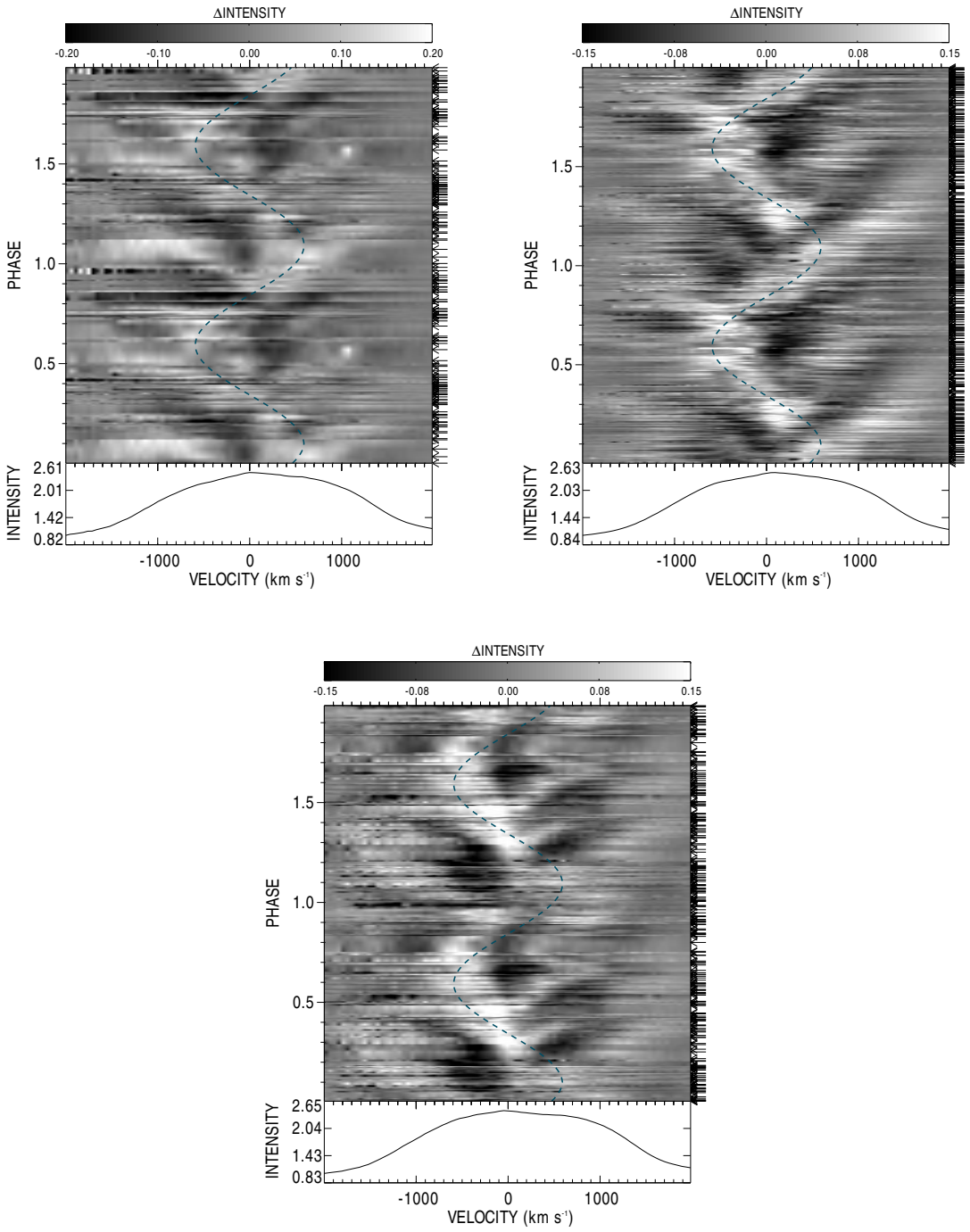

Figure 2.14: Difference grayscale images of the spectra are shown with the kinematics model over plotted as a blue dashed line. The images are increasing with time, from top left, top right to bottom and are grouped in 40-day (18 cycle) segments.

2.6.4 Variations in Other Spectral Lines

The He II λ5411 emission line is the least-blended and therefore will give the clearest results. It is, also, relatively strong. However, two other emission lines were also analyzed in order to search for similar CIR patterns. Two phased grayscale difference images were created during the time period of HJD 2456478 - 2456518, when the central CIR was the strongest; one of the C IV λ5802/5812 Å doublet and the other of He I λ5876 Å. These are displayed in Figure 2.15. Because the amateur astronomers did not focus on these lines, only the professional data were used in order to make these comparisons (see Table 2.I for a full list of the professional observatories).

The C IV emission line displays the same central CIR that is detectable in the He II line, but this line is much fainter than He II λ5411 and thus the data appear more noisy and the CIR is more difficult to see on the grayscale images. For comparison purposes, we have superposed on the C IV grayscale image the fit of the He II main CIR. The agreement is very good. This is not surprising since those two transitions have similar ionization energies (see Table 2.V) and are formed in very similar regions of the wind. This can be seen in Figure 2.16, which displays the line formation zones of each of the three emission lines as a function of both radial distance and velocity using the line-blanketing non-LTE models found in Gräfener et al. (2002) and Hamann & Gräfener (2003) tailored for WR 134. The He I emission line also faintly displays the strong CIR seen in He II, but in addition shows a DAC-like feature on the blue side of the line, moving from $v \simeq -1200$ km s^{-1} at $\phi = 0.90$ to $v \simeq -1600$ km s^{-1} at $\phi = 1.65$ (or -0.10 to 0.65). We have added red crosses to Figure 2.15 to indicate the position of the DAC. The velocity of this absorption feature is compatible with that of the second incomplete CIR and therefore we associate the DAC to this CIR rather than with the central one. Furthermore, it appears around phase 0.85, which is approximately where the CIR in emission would appear if it were complete.

One interesting feature of the faint CIR seen in emission in this transition is that it appears shifted in phase by ~ 0.15 compared to the fit of the He II grayscale. This shift is most likely due to the line formation zone of He I being located further out in the wind than that of He II (see Figure 2.17) and therefore the CIR feature will show a slight delay as it rotates. Such a shift in phase for lines formed at different distances in the wind was

in fact predicted by Dessart & Chesneau (2002) in their theoretical modelling of CIRs. Figure 2.16 displays both the C IV and He I lines on one grayscale image showing how the CIR feature within the C IV line effects the DAC features within the blue side of the He I line due to their close proximity. One can see that the absorption pattern of He I λ5876 is partially filled in by the emission pattern of C IV λ5802/5812 near phase 0.4.

Ionization energy		
Line	**eV**	**cm^{-1}**
He I	24.58	198310.67
He II	54.42	438908.88
C IV	64.49	520178.16

Table 2.V: List of three analyzed emission lines and their corresponding ionization energy values.

2.6.5 Small-scale structures

WR 134 was first discovered to present small-scale structures within its wind by Moffat et al. (1988), who also observed the He II λ5411 emission line. They observed this star using the Canada-France-Hawaii Telescope (CFHT), along with another WN6 star, WR 136, and their data had an average S/N ratio of $\sim$ 300. Data were collected over one night and small structures were seen moving away from the line center on timescales of hours, through analysis of the difference spectra. The star WR 136, however, did not show such features at the time due to insufficient S/N. In order to search for these structures within our campaign data, two conditions had to be met: 1) the data must all be taken continuously with no large time gaps and 2) the S/N ratio and resolution must be high enough to rule out any possibility of noise hindering the detection. Because the Teide data had an order merge within the emission line, they became unreliable for the study of the small-scale structures as this increased the noise significantly. This left only the Keck data that met the conditions needed for this study, with a total of 35 spectra obtained using an echelle spectrograph (see Tables 2.I and 2.II) during a single night in three groups. The 6^{th} order of the spectra included the He II λ5411 emission line, covering a wavelength interval of 5100 - 6000 Å. Figure 2.18 displays the average of each of the 3 data groups for this line.

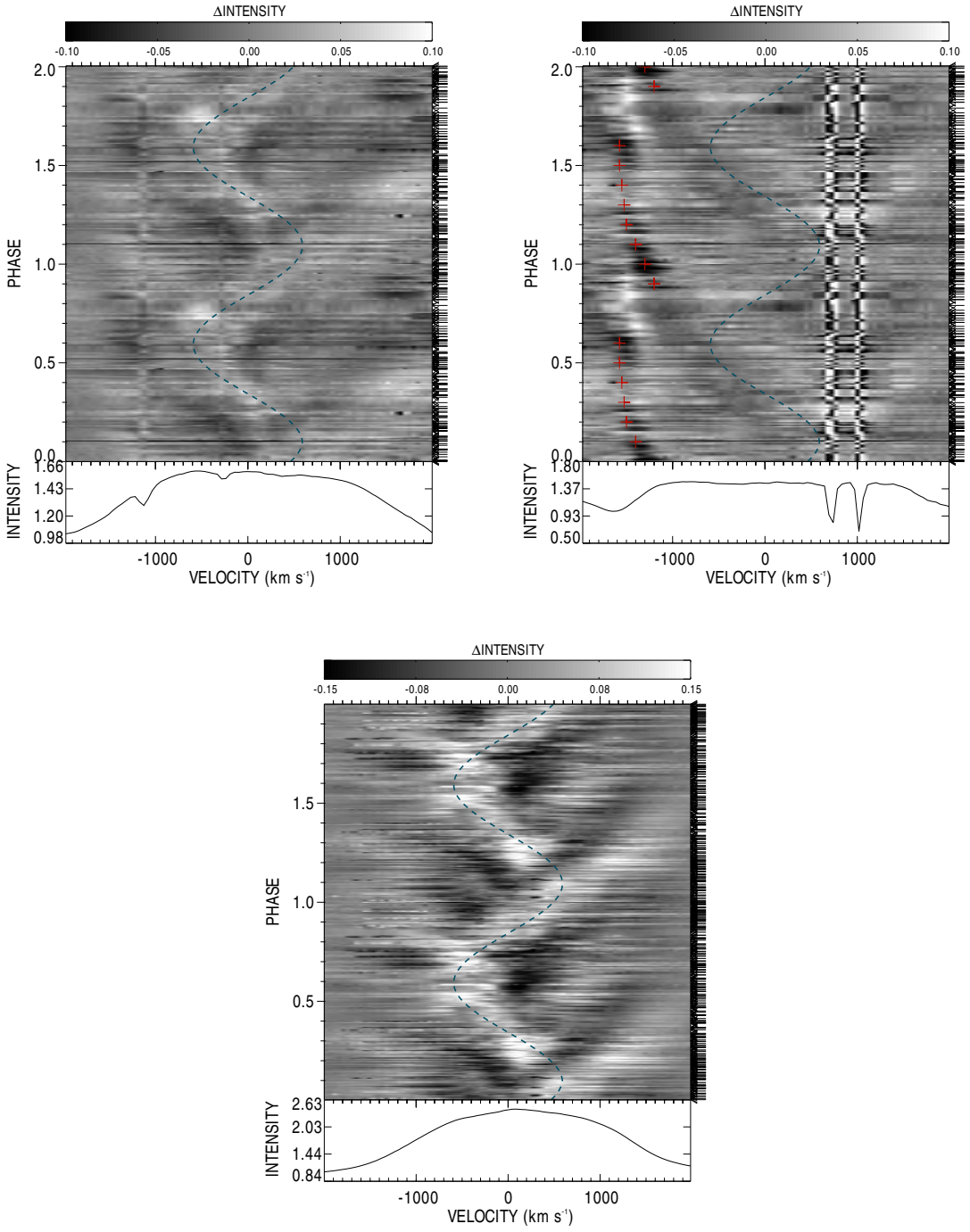

Figure 2.15: The phased difference grayscale images of the C IV λ5802,5812 doublet, with a mean wavelength of λ5806 adopted (*top left*), the He I λ5876 (*top right*) and He II λ5411 (*bottom*) emission lines during the second 40-day period of the campaign. The DAC-like feature is outlined (*red crosses*) at negative velocities in the He I λ5876 line. The dashed blue line represents the kinematics model calculated in section 2.6.2.

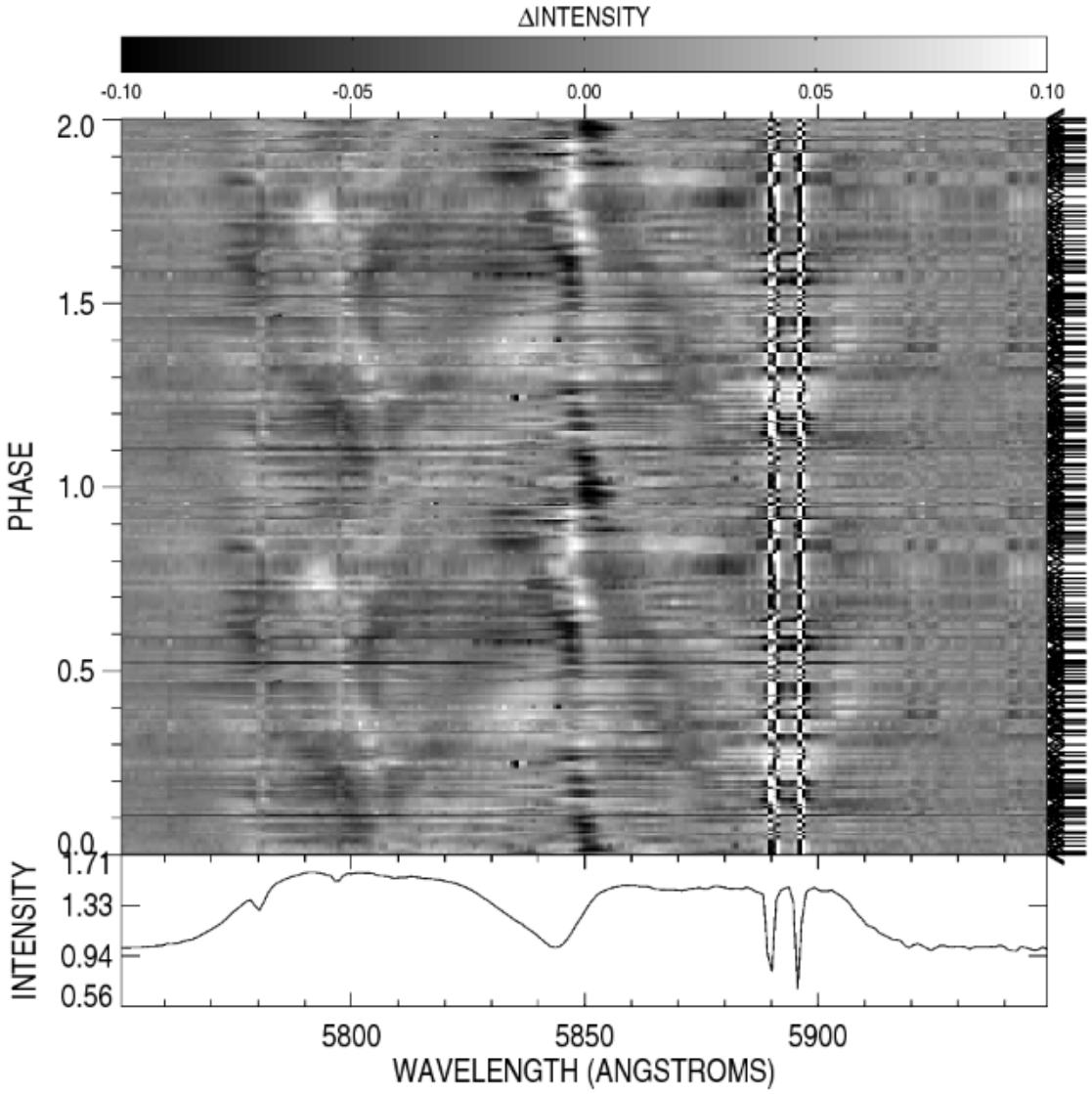

Figure 2.16: Phased difference grayscale image of both the C IV λ5802,5812 doublet and the He I λ5876 lines. This image displays how the CIRs within the C IV line affects the DAC features present within the He I line.

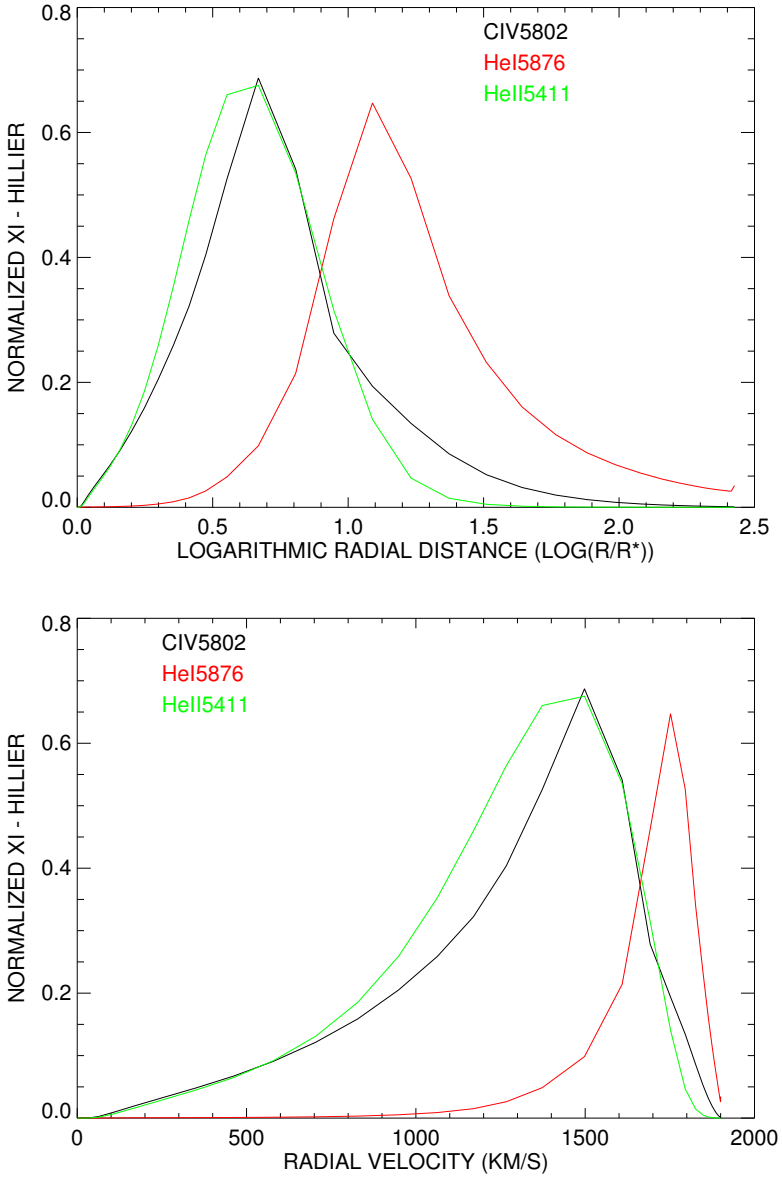

Figure 2.17: Results of the Hamann & Gräfener (2003) line-blanketing non-LTE model for WR 134 using $v_\infty \sim 1900$ km s^{-1} (Shenare, private communication). The top plot displays the formation regions of each of the three emission lines analyzed in this work as a function of radial distance, while the bottom plot shows the formation regions as a function of velocity. It can be seen that the He I formation zone is the furthest out from the star of the three lines.

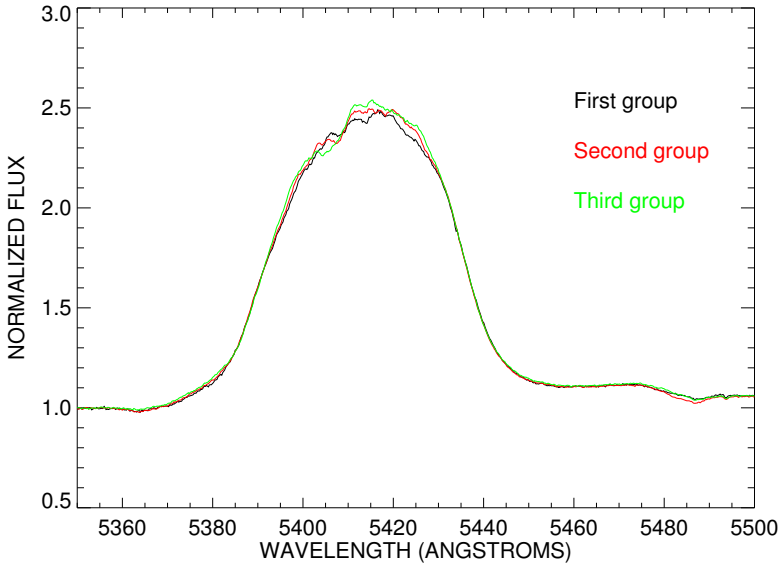

Figure 2.18: Plot of the three binned sets of Keck spectra of the He II λ5411 emission line. The time sequence is indicated in the legend.

In order to identify variations caused by clumps, we must first understand the changes due to the CIRs within this observing night. From Figure 2.18, the intensity change of the CIR can be clearly seen as a gradual increase of the flux during the night on the red-side of the line while the blue-side remains relatively constant. In order to search for clumps, none of the Keck data were combined. Difference spectra were then calculated using the mean spectrum of the Keck data alone, which rendered the search for any short timescale changes in the emission line easier. This is presented in Figure 2.19. In this figure, the effect of the CIR is visible once more on the red side of the line by a gradual passage from mainly negative flux differences in group 1 to mainly positive flux differences in group 3. In addition, and in spite of the paucity of the data, several clumps are detected on the red-side and blue-side of the central line and are found to move red-ward and blue-ward in time. These are displayed as dashed lines in Figure 2.19.

WR 134 has previously shown clumpy structures within its wind (Moffat et al., 1988). One question that we aimed to answer during this campaign is whether these clumpy structures are always present and if they can be detected while the CIR has a strong presence within the wind. With this dataset, we have been able to determine that clumps

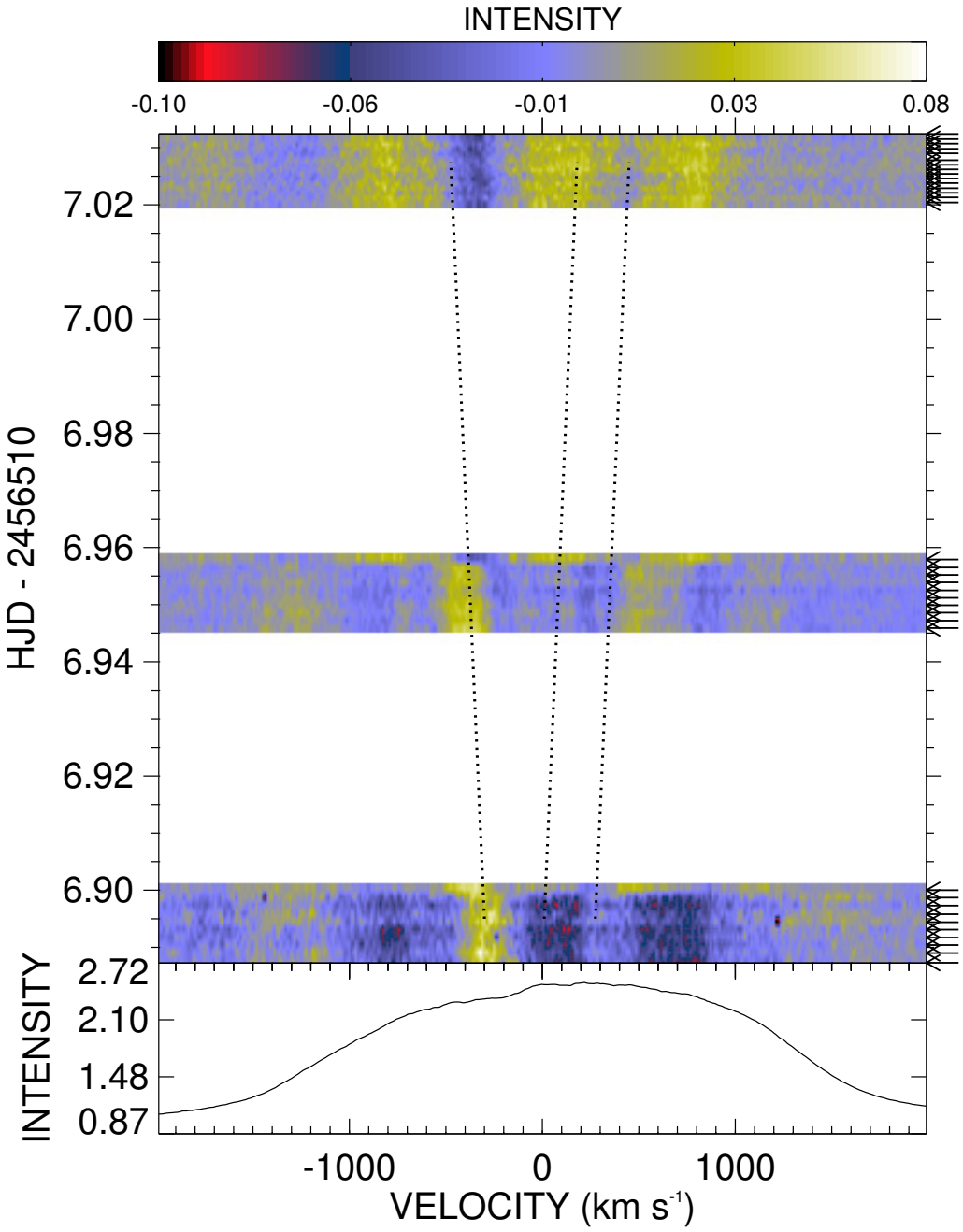

Figure 2.19: Difference spectra from the mean of the Keck data. The top panel shows the intensity of each spectrum, while the bottom panel shows the mean Keck spectrum of the He II λ5411 emission line in velocity space. The dotted lines indicate the movement of clumps over the night, while vertical arrows indicate the exact position of each spectrum in time.

and CIRs do indeed co-exist, although we were unable to study the details of the kinematics of the clumps with respect to that of the CIR due to the sparsity of our data within a given observing night.

2.7 CONCLUSION

Although the photospheres of massive, Wolf-Rayet (WR) stars are not visible due to their strong stellar winds and high mass-loss rates, studying the variabilities within their winds will make it easier to understand what is happening near their hydrostatic cores. While most WR stars show small-scale structures, or clumps, within their winds, only a few stars are currently known to show co-rotating interaction regions (CIRs). These features are formed when fast material collides with slower material, or vise-versa, as the star rotates. Because of this, the rotational period of a CIR that is present within the wind is associated with the rotational period of the star itself. They are easily detected using spectroscopic observations of their broad emission lines. Previously, no long-term study had been conducted in order to investigate the life-span of these large-scale structures. Because WR 134 has been known to show CIRs in its spectral lines (Morel et al., 1999), it was chosen along with WR 135 and WR 137 for a 4-month long professional and amateur collaboration during the summer of 2013.

A CIR period of 2.255 $\pm$ 0.008 days was found after reducing the spectroscopic data of the He II λ5411 emission line by calculating the moments of the line (Appendix II) and calculating a Scargle (1982) periodogram in velocity space (Figure 2.6). This line was chosen due to its relative isolation where no blending could occur with other emission lines. Using this calculated period, the spectra were organized by phase and difference grayscale plots were created in order to search for long-term variability. After a two-dimensional cross-correlation function (CCF) was applied to these difference plots, a $\sim$ 40-day time-coherency was seen after fitting a Gaussian function to the CCF (Figure 2.9). A time-dependent Scargle (1982) analysis of each moment also showed stronger intensities for a 40-day time interval near the center of the campaign (Figure 2.5), concluding that the CIR feature has an overall life time of $\sim$ 40 days, or 18 cycles. The difference images were compared with the CIR models created by Dessart & Chesneau (2002), leading us to conclude that it is an acceptable model to reproduce our observations and that

there were in fact two CIRs present within the wind of WR 134 during our observing campaign (Figure 2.12). The emission traces of these two CIRs reached different maximum velocities, strongly hinting that they emerge from different latitudes on the surface of the star. Furthermore, these different maximum velocities were reached at different phases. The phase shift of Δphase $\simeq$ 0.25 lead us to conclude that the CIRs are not found at the same longitude on the star but instead have a separation of $\Delta\phi \simeq 90°$. After also analyzing the C IV λ5806 and He I λ5876 emission lines, it was determined that the strong CIR is also detectable within the C IV line, while a DAC-like feature can be seen on the blue side of the He I line along with the central CIR which for that line is slightly shifted in phase compared to what is seen in the other two lines (Figure 2.14). This difference in phase is in qualitative agreement with the calculated models of Gräfener et al. (2002) and Hamann & Gräfener (2003), showing the formation regions of the three emission lines analyzed (Figure 2.17).

Small-scale features have been previously detected in this star (Moffat et al., 1988) and were also studied using this spectroscopic dataset. Only a small portion of our observations was usable for this particular study, due to the difficulty in detecting clumps with a strong CIR present in the wind. The spectra provided by Keck Observatory had a high enough resolution and S/N ratio, with a total of 35 obtained in a single night. A difference plot was created using the mean spectra of the Keck data (Figure 2.19), showing smaller features in the wind.

Not only were spectroscopic data taken of WR 134, but photometric and polarimetric data as well. These observations, along with the observations of WR 135 and WR 137 must still be analyzed. The target WR 135 was observed in order to observe its small-scale structures that are present within the wind, while WR 137 is a known long-period WR+O binary system with possible CIRs present. Each of these three targets will help us to better understand the nature of WR stars as a whole. The results presented on WR 134 have provoked astronomers to ask many more questions on the nature of hot-star winds, but has also shed light on the life cycle of these large-scale structures. These results would not have been possible without the enthusiasm of the amateur astronomer community.

CHAPTER 3

CONCLUSION

Although the photospheres of massive, Wolf-Rayet (WR) stars are not visible due to their strong stellar winds and high mass-loss rates, studying the variabilities within their winds will make it easier to understand what is happening near their hydrostatic cores. While most WR stars show small-scale structures, or clumps, within their winds, only a few stars are currently known to show co-rotating interaction regions (CIRs). These features are formed when fast material collides with slower material, or vise-versa, as the star rotates. Because of this, the rotational period of a CIR that is present within the wind is associated with the rotational period of the star itself. They are easily detected using spectroscopic observations of their broad emission lines. Previously, no long-term study had been conducted in order to investigate the life-span of these large-scale structures. Because WR 134 has been known to show CIRs in its spectral lines (Morel et al., 1999), it was chosen along with WR 135 and WR 137 for a 4-month long professional and amateur collaboration during the summer of 2013.

A CIR period of 2.255 $\pm$ 0.008 days was found after reducing the spectroscopic data of the He II λ5411 emission line by calculating the moments of the line (Appendix II) and calculating a Scargle (1982) periodogram in velocity space (Figure 2.6). This line was chosen due to its relative isolation where no blending could occur with other emission lines. Using this calculated period, the spectra were organized by phase and difference grayscale plots were created in order to search for long-term variability. After a two-dimensional cross-correlation function (CCF) was applied to these difference plots, a $\sim$ 40-day time-coherency was seen after fitting a Gaussian function to the CCF (Figure 2.9). A time-dependent Scargle (1982) analysis of each moment also showed stronger intensities for a 40-day time interval near the center of the campaign (Figure 2.5), concluding that the CIR feature has an overall life time of $\sim$ 40 days, or 18 cycles. The difference images were compared with the CIR models created by Dessart & Chesneau (2002), leading us to conclude that it is an acceptable model to reproduce our observations and that there were in fact two CIRs present within the wind of WR 134 during our observing

campaign (Figure 2.12). The emission traces of these two CIRs reached different maximum velocities, strongly hinting that they emerge from different latitudes on the surface of the star. Furthermore, these different maximum velocities were reached at different phases. The phase shift of $\Delta\text{phase} \simeq 0.25$ lead us to conclude that the CIRs are not found at the same longitude on the star but instead have a separation of $\Delta\phi \simeq 90°$. After also analyzing the C IV λ5806 and He I λ5876 emission lines, it was determined that the strong CIR is also detectable within the C IV line, while a DAC-like feature can be seen on the blue side of the He I line along with the central CIR which for that line is slightly shifted in phase compared to what is seen in the other two lines (Figure 2.14). This difference in phase is in qualitative agreement with the calculated models of Gräfener et al. (2002) and Hamann & Gräfener (2003), showing the formation regions of the three emission lines analyzed (Figure 2.17).

Small-scale features have been previously detected in this star (Moffat et al., 1988) and were also studied using this spectroscopic dataset. Only a small portion of our observations was usable for this particular study, due to the difficulty in detecting clumps with a strong CIR present in the wind. The spectra provided by Keck Observatory had a high enough resolution and S/N ratio, with a total of 35 obtained in a single night. A difference plot was created using the mean spectra of the Keck data (Figure 2.19), showing smaller features in the wind.

Not only were spectroscopic data taken of WR 134, but photometric and polarimetric data as well. These observations, along with the observations of WR 135 and WR 137 must still be analyzed. The target WR 135 was observed in order to observe its small-scale structures that are present within the wind, while WR 137 is a known long-period WR+O binary system with possible CIRs present. Each of these three targets will help us to better understand the nature of WR stars as a whole. The results presented on WR 134 have provoked astronomers to ask many more questions on the nature of hot-star winds, but has also shed light on the life cycle of these large-scale structures. These results would not have been possible without the enthusiasm of the amateur astronomer community.

BIBLIOGRAPHY

Cantiello, M., Langer, N., Brott, I., et al. 2009, A&A, 499, 279

Castor, J. I., Abbott, D. C., & Klein, R. I. 1975, ApJ, 195, 157

Chené, A.-N., & St-Louis, N. 2010, ApJ, 716, 929

Chené, A.-N., Moffat, A. F. J., Cameron, C., et al. 2011, ApJ, 735, 34

Cranmer, S. R., & Owocki, S. P. 1996, ApJ, 462, 469

Crowther, P., & Smartt, S. 2007, Astronomy and Geophysics, 48, 35

Crowther, P. A., & Bohannan, B. 1996, in Liege International Astrophysical Colloquia, Vol. 33, Liege International Astrophysical Colloquia, ed. J. M. Vreux, A. Detal, D. Fraipont-Caro, E. Gosset, & G. Rauw, 437

Dessart, L., & Chesneau, O. 2002, A&A, 395, 209

Drissen, L., Robert, C., Lamontagne, R., et al. 1989, ApJ, 343, 426

Ekström, S., Georgy, C., Eggenberger, P., et al. 2012, A&A, 537, A146

Fahed, R., Moffat, A. F. J., Zorec, J., et al. 2011, MNRAS, 418, 2

Gräfener, G., Koesterke, L., & Hamann, W.-R. 2002, A&A, 387, 244

Hamann, W.-R., & Gräfener, G. 2003, A&A, 410, 993

Howarth, I. D., & Prinja, R. K. 1996, Ap&SS, 237, 125

Howarth, I. D., Prinja, R. K., & Massa, D. 1995, ApJ, 452, L65

Ignace, R., St-Louis, N., & Proulx-Giraldeau, F. 2015, A&A, 575, A129

Lamers, H. J. G. L. M., & Cassinelli, J. P. 1999, Introduction to Stellar Winds

Lefèvre, L., Marchenko, S. V., Lépine, S., et al. 2005, MNRAS, 360, 141

Lepine, S., Moffat, A. F. J., & Henriksen, R. N. 1996, ApJ, 466, 392

Lobel, A., & Blomme, R. 2008, ApJ, 678, 408

Maeder, A., & Meynet, G. 1987, A&A, 182, 243

McCandliss, S. R., Bohannan, B., Robert, C., & Moffat, A. F. J. 1994, Ap&SS, 221, 155

Moffat, A. F. J., Drissen, L., Lamontagne, R., & Robert, C. 1988, ApJ, 334, 1038

Moffat, A. F. J., & Marchenko, S. V. 1993, AJ, 105, 339

Morel, T., St-Louis, N., & Marchenko, S. V. 1997, ApJ, 489, 1004

Morel, T., Marchenko, S. V., Eenens, P. R. J., et al. 1999, ApJ, 518, 428

Mullan, D. J. 1984, ApJ, 283, 303

Owocki, S. P., Castor, J. I., & Rybicki, G. B. 1988, ApJ, 335, 914

Owocki, S. P., & Rybicki, G. B. 1984, ApJ, 284, 337

—. 1985, ApJ, 299, 265

—. 1991, ApJ, 368, 261

Prinja, R. K., & Howarth, I. D. 1988, MNRAS, 233, 123

Robert, C., Moffat, A. F. J., Drissen, L., et al. 1992, ApJ, 397, 277

Scargle, J. D. 1982, ApJ, 263, 835

St-Louis, N., Dalton, M. J., Marchenko, S. V., Moffat, A. F. J., & Willis, A. J. 1995, ApJ, 452, L57

Stellingwerf, R. F. 1978, ApJ, 224, 953

van Genderen, A. M. 1985, A&A, 151, 349

Wolf, C. J. E., & Rayet, G. 1867, Comptes Rendus de l'Académie des sciences, 65, 292

Appendix I

Difference plots of He II λ5411 emission line

Difference plots from the mean He II λ5411 emission line for the entire data set of WR 134. Top panels show the intensity scale of each while the bottom panels show the mean spectrum in velocity space. The arrows indicate the location of each spectrum in time. The starting HJD represents the first night of the campaign.

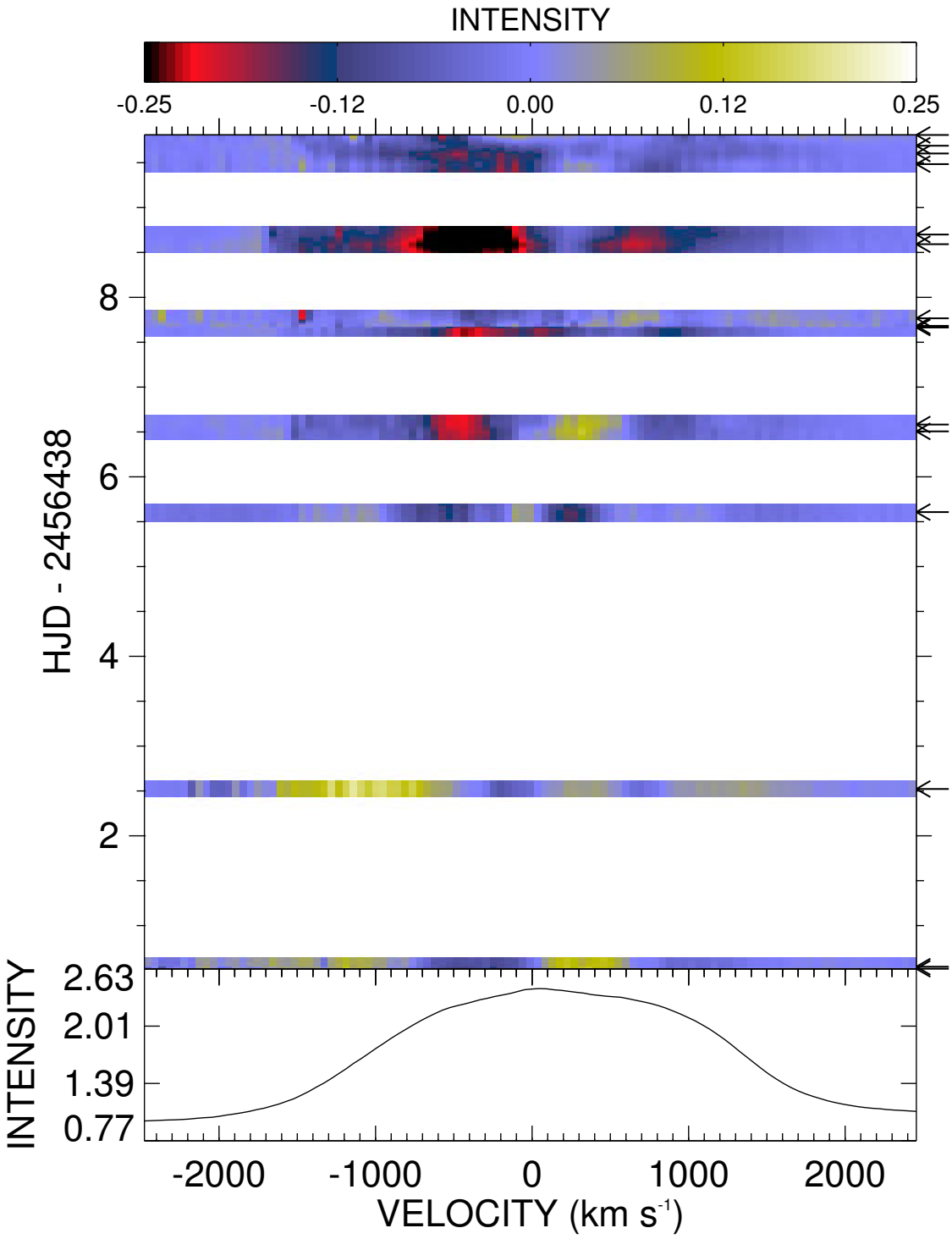
INTENSITY
-0.25
-0.12
0.00
0.12
0.25
HJD - 2456438
8
6
4
2
INTENSITY
2.63
2.01
1.39
0.77
-2000
-1000
0
1000
2000
VELOCITY (km s-1)

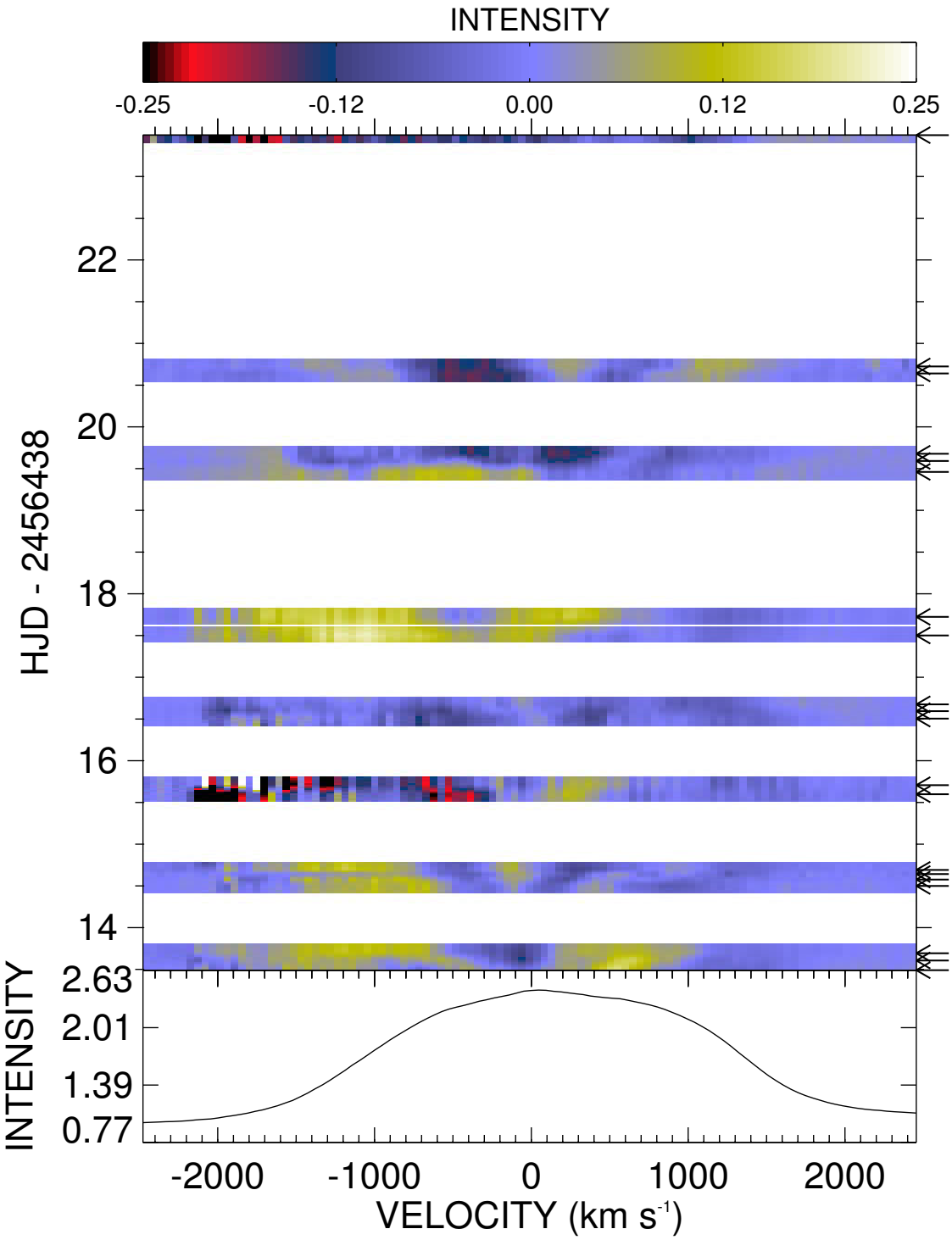
INTENSITY
-0.25
-0.12
0.00
0.12
0.25
HJD - 2456438
22
20
18
16
14
INTENSITY
2.63
2.01
1.39
0.77
-2000
-1000
0
1000
2000
VELOCITY (km s-1)

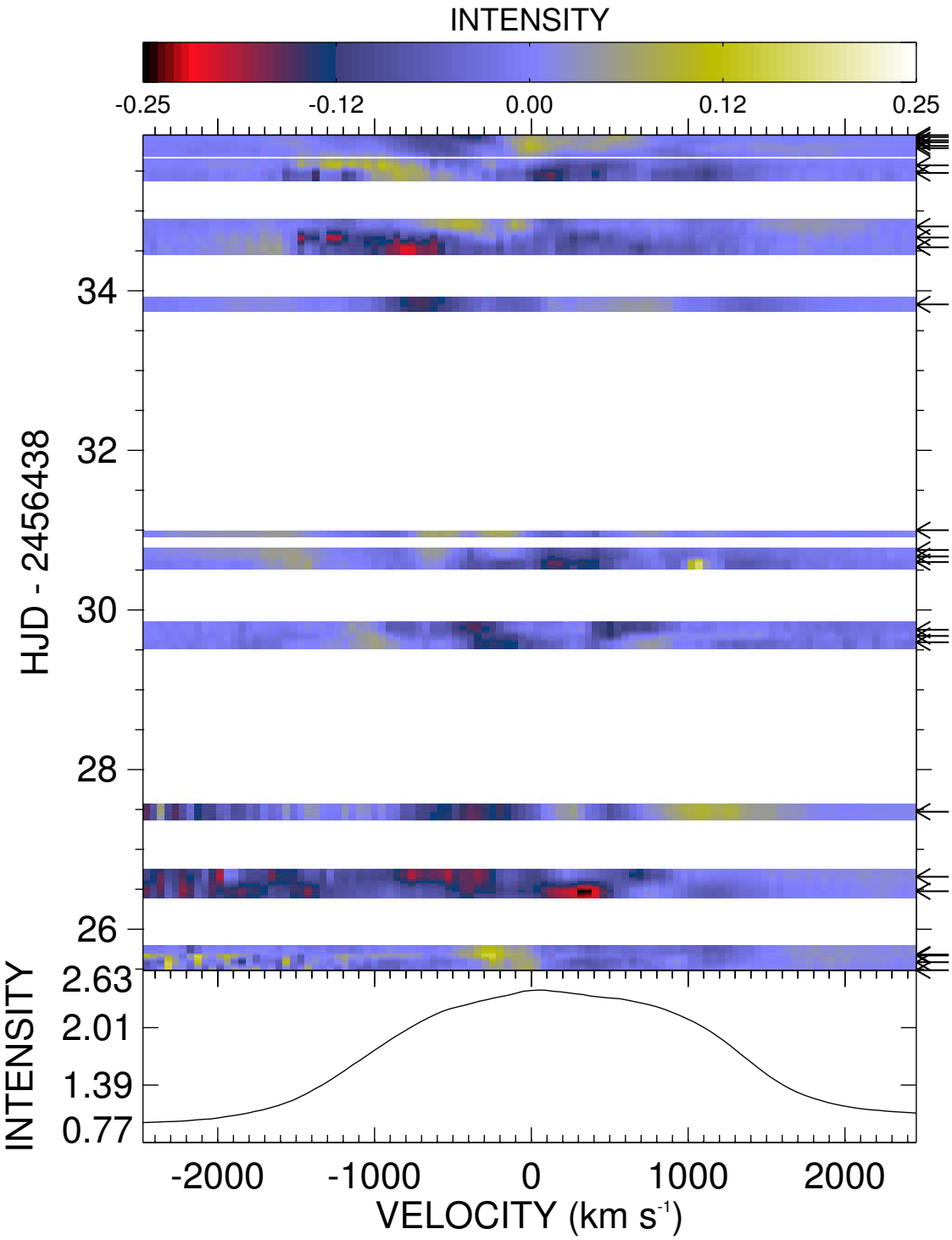
INTENSITY
-0.25
-0.12
0.00
0.12
0.25
34
32
30
28
26
HJD - 2456438
2.63
2.01
1.39
0.77
INTENSITY
-2000
-1000
0
1000
2000
VELOCITY (km s-1)

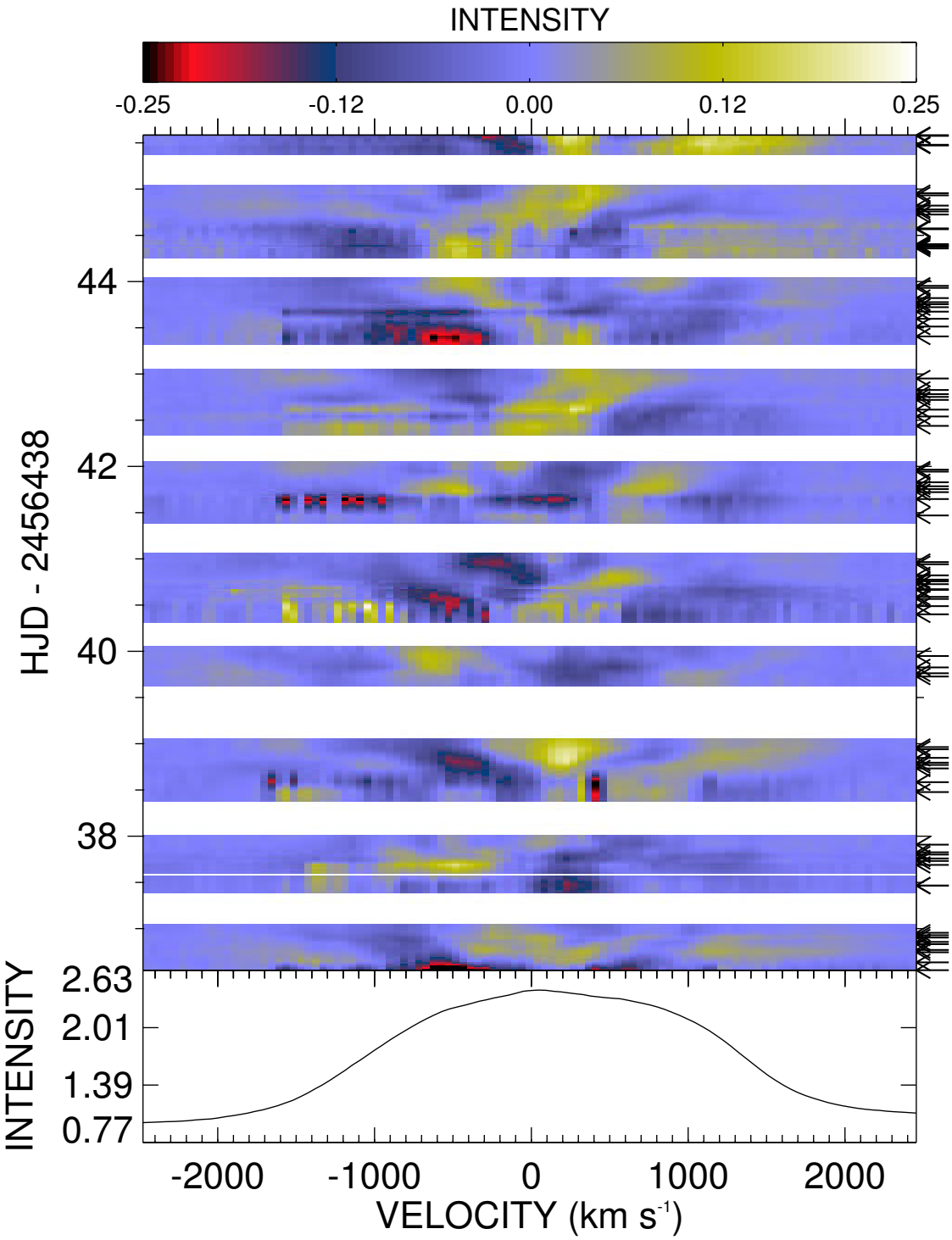
INTENSITY
-0.25
-0.12
0.00
0.12
0.25
HJD - 2456438
44
42
40
38
INTENSITY
2.63
2.01
1.39
0.77
-2000
-1000
0
1000
2000
VELOCITY (km s-1)

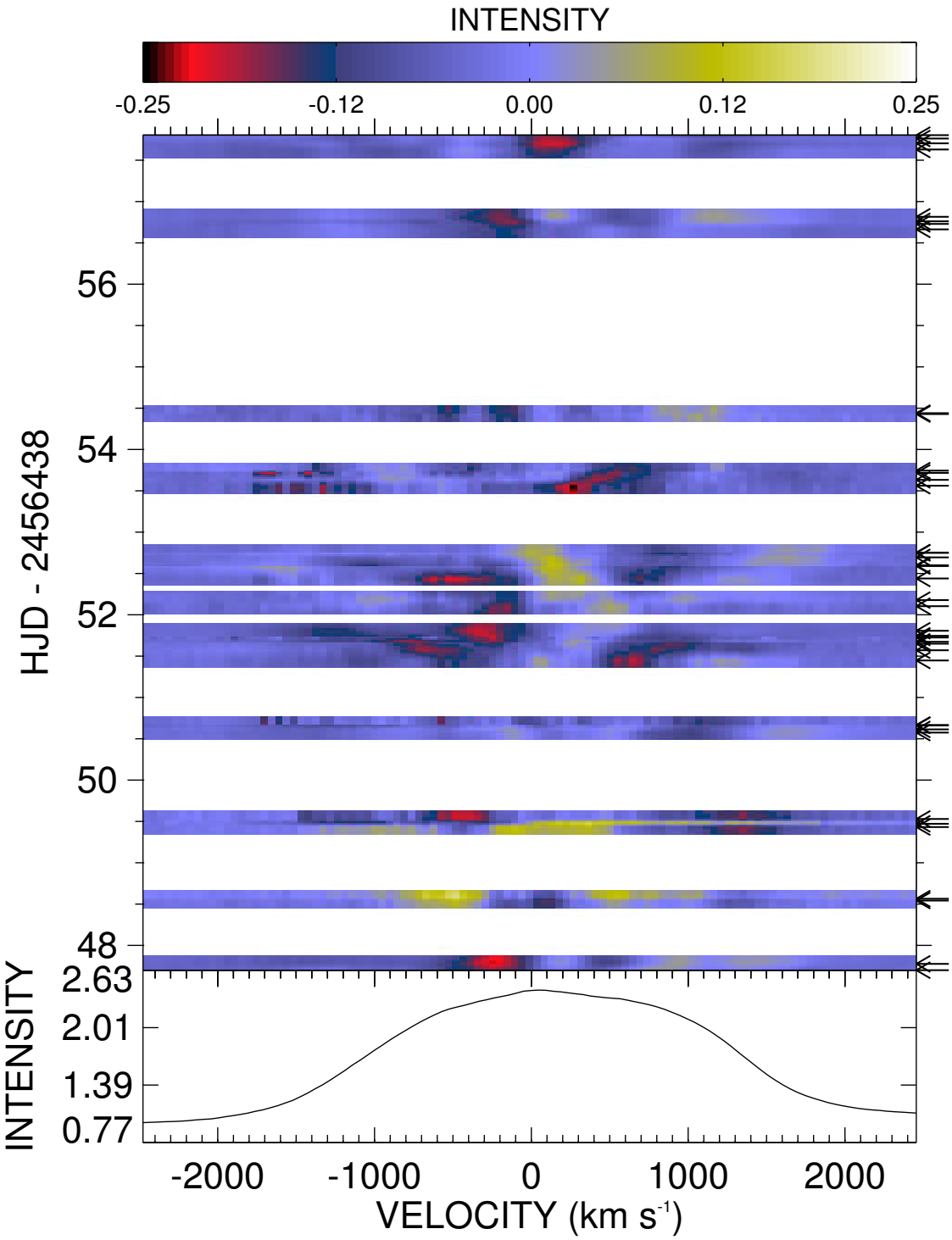
INTENSITY
-0.25
-0.12
0.00
0.12
0.25
HJD - 2456438
56
54
52
50
48
INTENSITY
2.63
2.01
1.39
0.77
-2000
-1000
0
1000
2000
VELOCITY (km s-1)

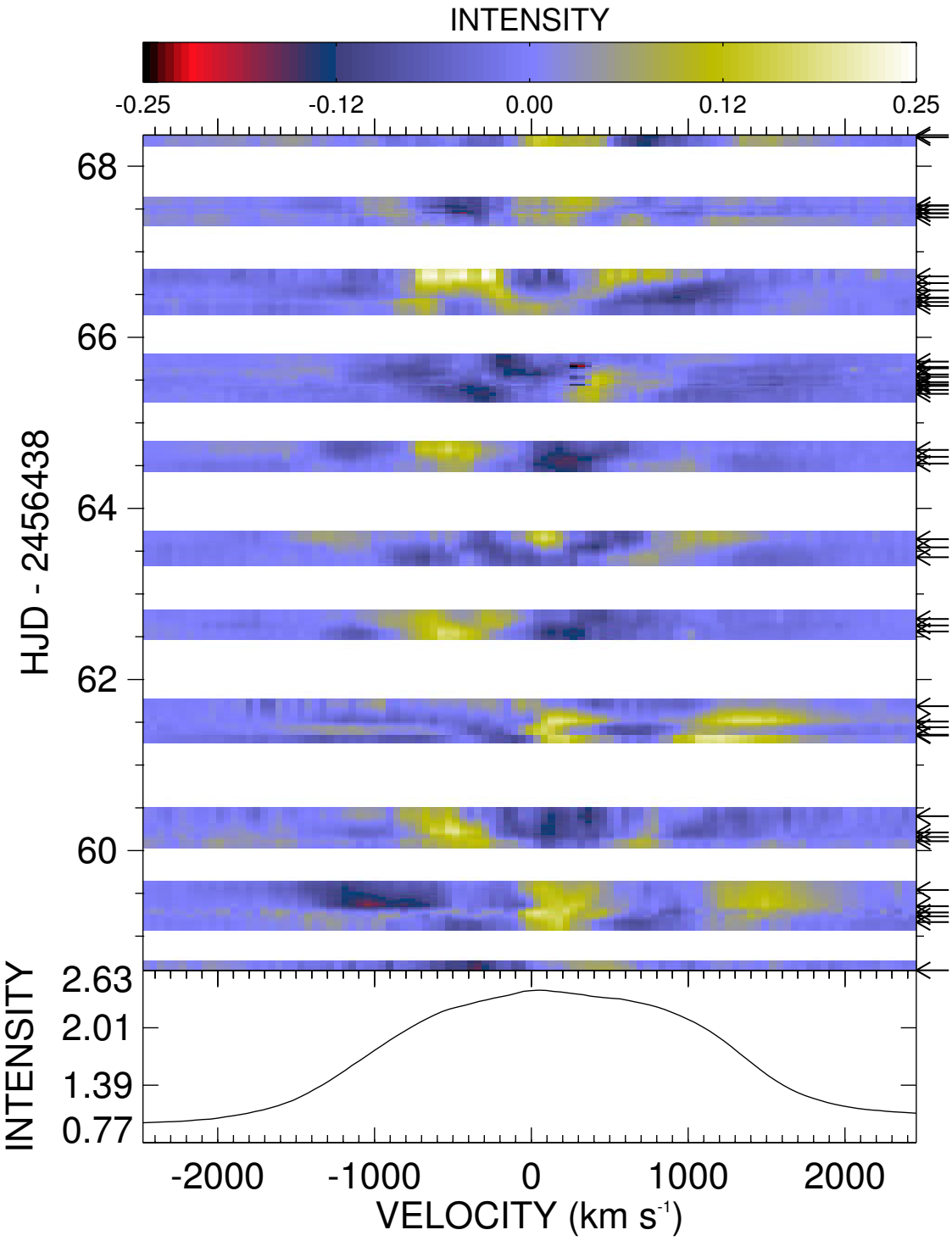
INTENSITY
-0.25
-0.12
0.00
0.12
0.25
68
66
64
62
60
HJD - 2456438
INTENSITY
2.63
2.01
1.39
0.77
-2000
-1000
0
1000
2000
VELOCITY (km s-1)

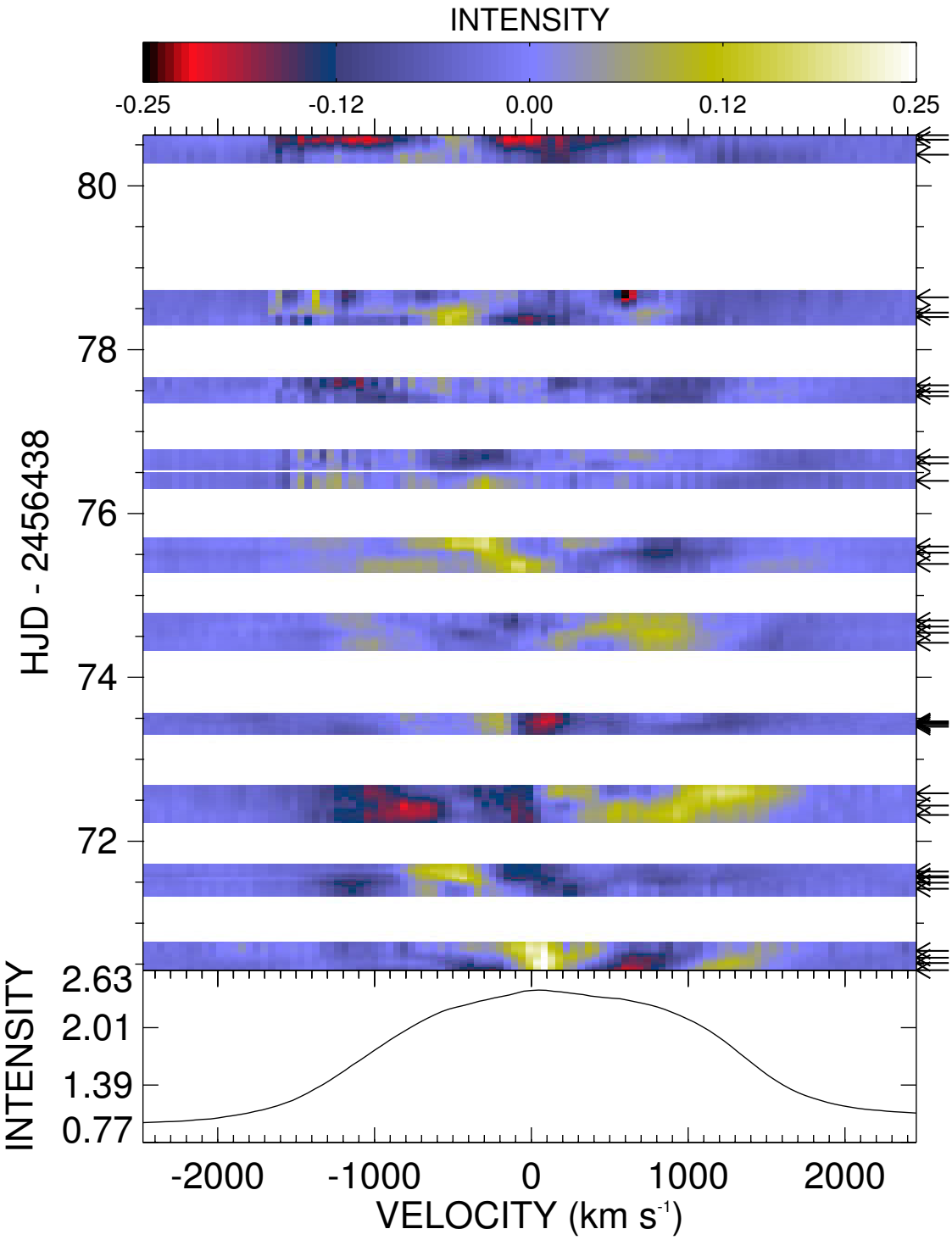
INTENSITY
-0.25
-0.12
0.00
0.12
0.25
80
78
76
74
72
HJD - 2456438
INTENSITY
2.63
2.01
1.39
0.77
-2000
-1000
0
1000
2000
VELOCITY (km s-1)

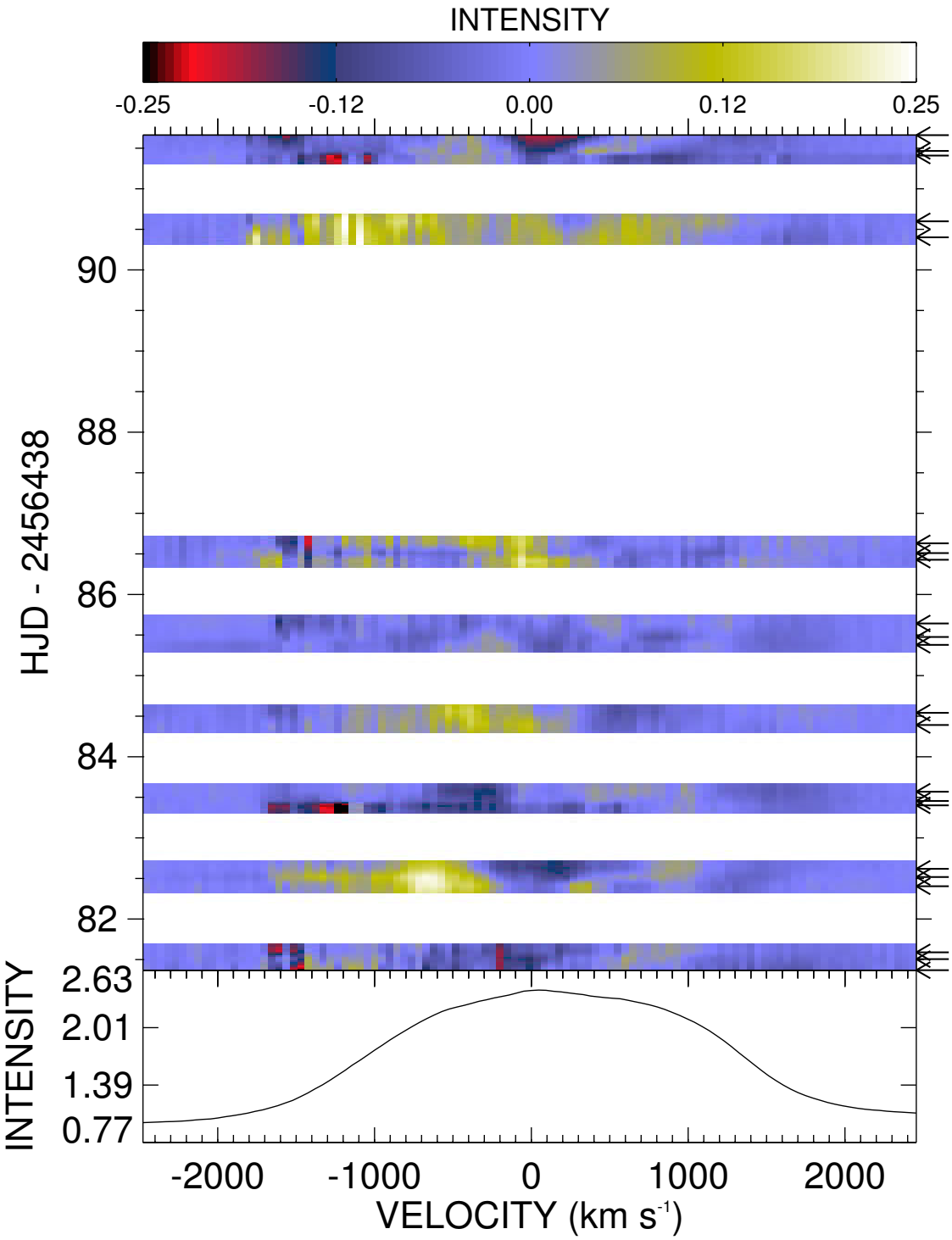
INTENSITY
-0.25
-0.12
0.00
0.12
0.25
HJD - 2456438
90
88
86
84
82
INTENSITY
2.63
2.01
1.39
0.77
-2000
-1000
0
1000
2000
VELOCITY (km s-1)

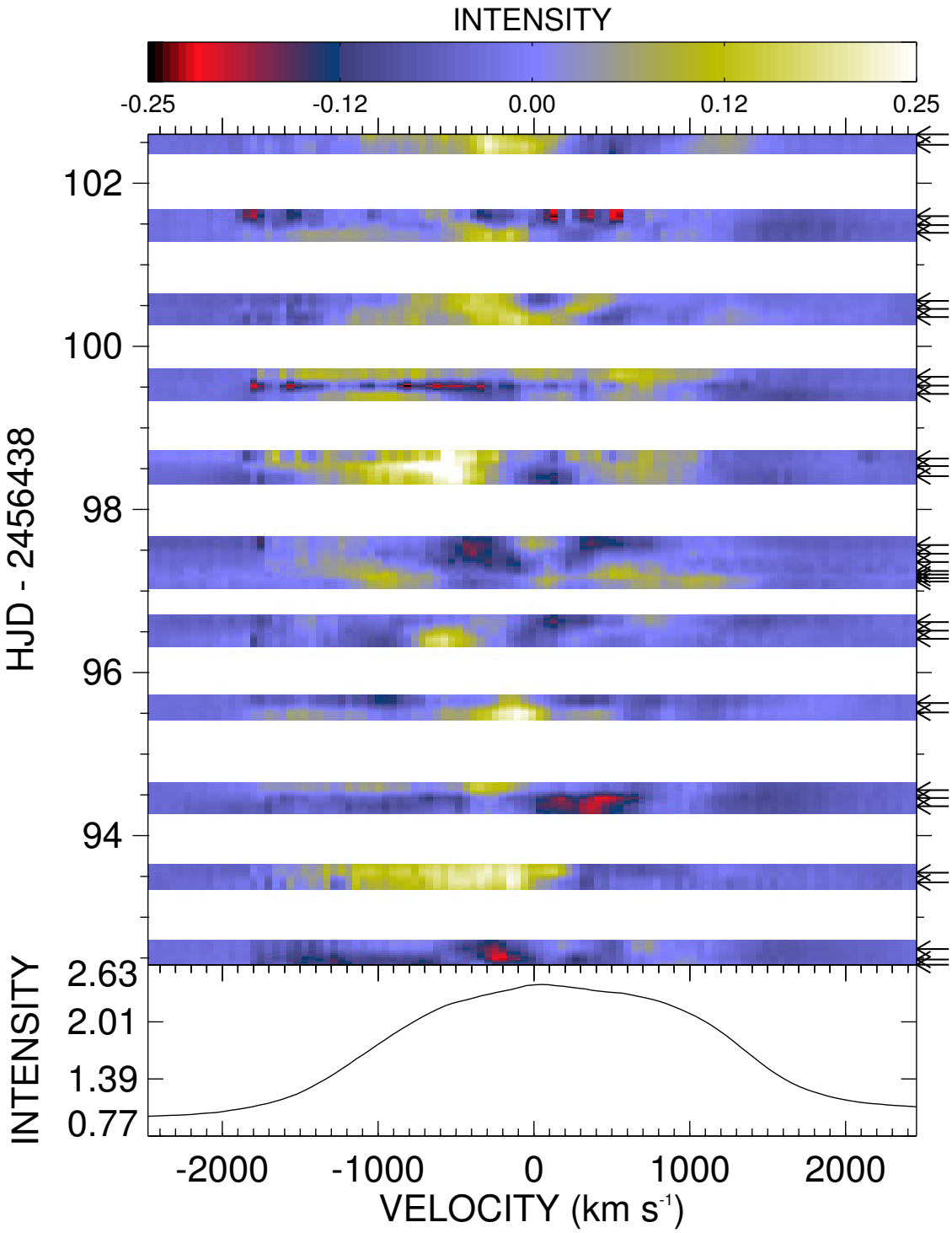
INTENSITY
-0.25
-0.12
0.00
0.12
0.25
102
100
98
96
94
HJD - 2456438
INTENSITY
2.63
2.01
1.39
0.77
-2000
-1000
0
1000
2000
VELOCITY (km s-1)

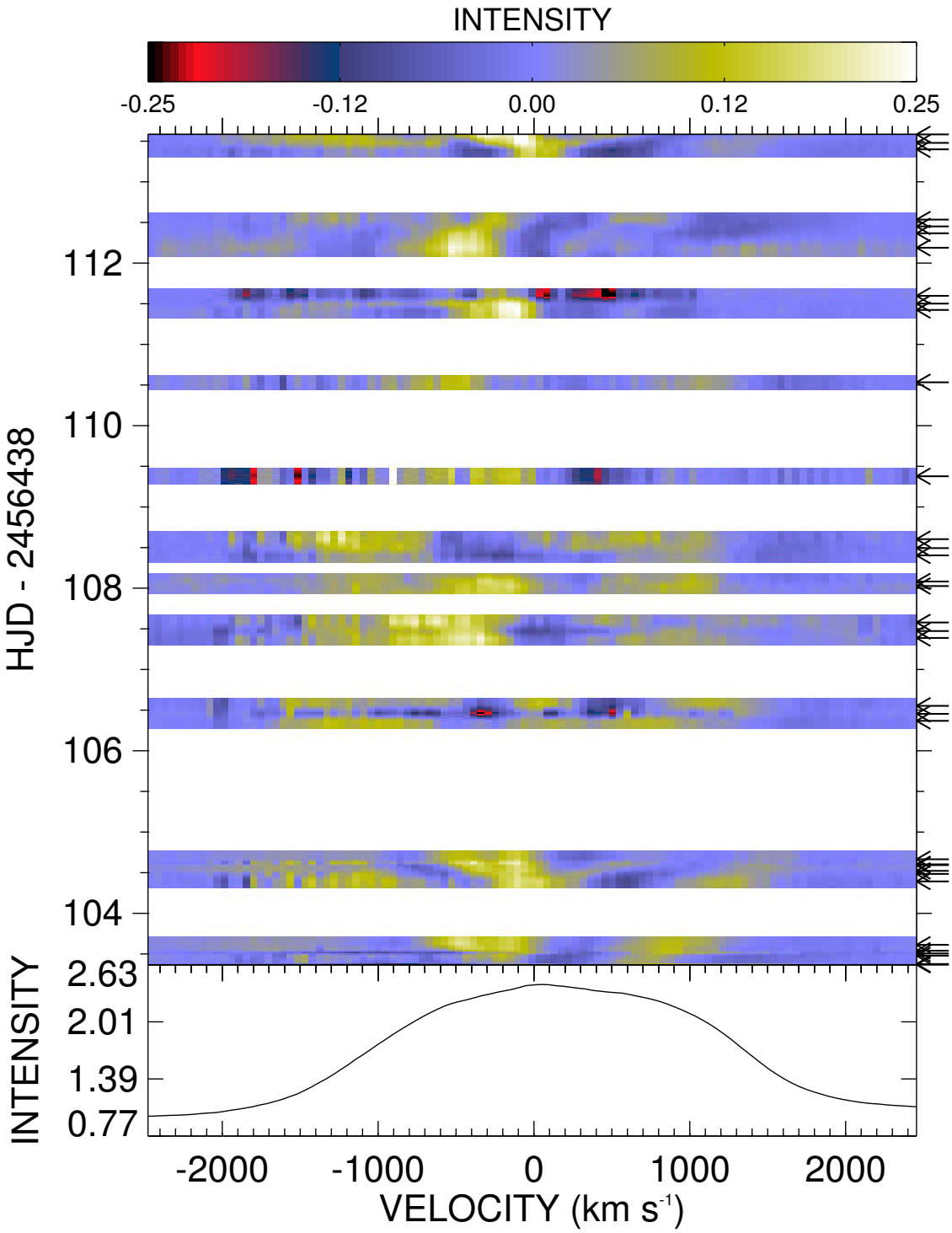
INTENSITY
-0.25
-0.12
0.00
0.12
0.25
HJD - 2456438
112
110
108
106
104
INTENSITY
2.63
2.01
1.39
0.77
-2000
-1000
0
1000
2000
VELOCITY (km s-1)

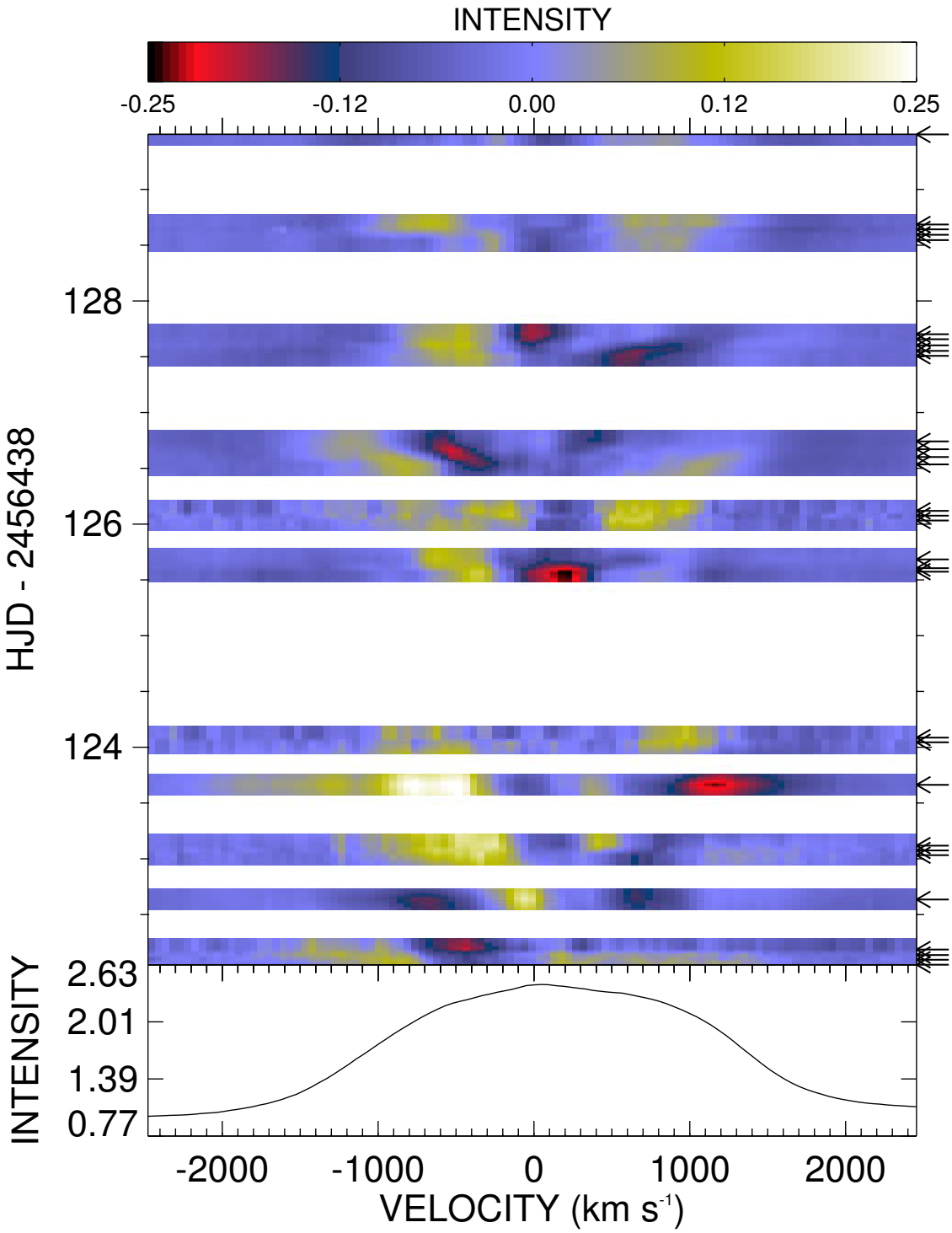
INTENSITY
-0.25
-0.12
0.00
0.12
0.25
128
126
124
HJD - 2456438
INTENSITY
2.63
2.01
1.39
0.77
-2000
-1000
0
1000
2000
VELOCITY (km s-1)

Appendix II

Moments values

Table of values for each moment of the He II λ5411 emission line of WR 134. Each corresponding HJD and location observed are also given.

Table II.I

HJD - 2450000	EW	SKEWNESS	SKEW ERR	KURTOSIS	KURT ERR	BISECTOR	FLUX VEL	FWHM	OBSERVER
6438.5190	-62.607803	-0.17594901	0.0015830999	2.2209218	0.0025473000	118.71126	-76.357269	3008.7715	Teide
6438.5415	-62.701847	-0.17180730	0.0011532000	2.2184494	0.0018507000	143.86746	-84.580971	2913.0647	Teide
6440.5220	-64.958946	-0.15859480	0.00096650003	2.2228892	0.0015588000	104.94848	-79.502899	3079.6392	Teide
6443.6069	-59.188412	-0.18196049	0.0013437000	2.2279646	0.0021742000	113.58641	-70.797455	2928.5801	Teide
6444.5068	-58.889858	-0.19139400	0.0019089000	2.2258694	0.0030807999	154.72630	-71.249428	2852.3083	Teide
6444.5830	-58.550873	-0.19291180	0.0018857000	2.2244613	0.0030406001	151.32875	-70.256645	2848.8108	Teide
6445.6636	-55.969688	-0.17576510	0.0026952000	2.1878581	0.0042388001	145.51569	-79.409119	2891.9585	Teide
6445.6816	-62.435829	-0.18043271	0.0046283002	2.2222357	0.0074517000	154.56253	-73.462944	2972.8901	Potter
6445.7666	-61.600597	-0.19099760	0.0033932000	2.2218218	0.0054657999	161.08357	-69.039658	2966.3044	Potter
6446.5918	-51.925636	-0.19179320	0.0038079999	2.1841965	0.0059715002	178.40433	-73.297798	2758.9055	Teide
6446.6997	-52.112705	-0.19203091	0.0034189001	2.1947784	0.0054000001	171.52049	-73.710258	2731.4143	Teide
6447.4839	-58.710373	-0.18100449	0.0015574000	2.2087264	0.0024868001	136.26028	-74.132370	2921.7639	Teide
6447.6030	-56.767082	-0.18583480	0.0015353000	2.2061212	0.0024458000	142.94780	-74.482239	2840.9690	Teide
6447.6890	-58.098461	-0.18362001	0.0015784000	2.2174981	0.0025329001	146.29626	-73.772652	2826.9673	Teide
6447.8091	-60.988171	-0.18774900	0.0038238000	2.2343585	0.0062068999	180.69113	-67.046989	2905.7310	Potter
6451.4902	-63.647572	-0.17453530	0.0011628000	2.2418685	0.0018956000	79.344620	-78.287674	3002.1819	Teide
6451.6064	-63.618862	-0.17038549	0.00092289998	2.2346749	0.0014990000	77.944305	-78.797897	3004.2290	Teide
6451.6929	-64.318459	-0.16172680	0.00079050002	2.2209206	0.0012724000	72.881859	-85.584930	3030.4856	Teide
6452.5000	-62.295700	-0.15813109	0.0012242000	2.2271295	0.0019745999	111.17108	-84.773727	3018.8743	Teide
6452.5757	-62.532112	-0.15895151	0.0011665000	2.2268074	0.0018816000	83.710884	-86.763603	3038.0618	Teide
6452.6421	-61.281258	-0.16950241	0.0025613999	2.2306559	0.0041434998	125.56682	-79.652824	2946.5994	Potter
6452.6909	-62.304001	-0.15038490	0.0010229000	2.2176528	0.0016408000	67.059425	-90.713844	3031.8799	Teide
6453.5986	-56.087536	-0.22944459	0.0025611999	2.3177404	0.0044058999	149.35255	-29.872833	2832.3040	Teide
6453.7070	-58.548161	-0.21447220	0.0032329999	2.2515345	0.0053074001	188.50082	-59.510605	2744.6113	Teide
6454.5044	-59.227283	-0.17687100	0.0015338000	2.2197645	0.0024643999	130.44379	-75.469170	2878.5188	Teide
6454.5942	-58.428631	-0.18675520	0.0012478000	2.2384911	0.0020303000	151.86810	-66.404221	2887.8928	Teide
6454.6753	-59.656223	-0.17997210	0.0012615999	2.2340515	0.0020458000	159.79964	-70.119743	2915.1702	Teide
6455.5005	-66.479996	-0.13004720	0.00092500000	2.2210116	0.0014840000	70.900208	-106.00752	3043.9910	Teide
6455.7241	-66.041245	-0.14277939	0.0013915000	2.2295878	0.0022472001	44.080318	-99.710373	3078.7886	Teide
6457.4604	-64.313919	-0.15807350	0.0010569000	2.2251809	0.0017020000	136.70622	-87.143127	3006.1365	Teide
6457.5918	-59.579540	-0.17613730	0.0019626000	2.2081585	0.0031287000	181.00749	-75.625275	2858.6946	Teide
6457.6782	-58.564003	-0.17235041	0.0023596000	2.1945925	0.0037263001	163.87595	-79.784454	2879.8201	Teide
6458.6401	-60.028393	-0.19542959	0.0027079000	2.2179830	0.0043620002	134.52882	-66.285896	2956.1592	Potter
6458.7241	-61.048725	-0.19146280	0.0024401001	2.2127872	0.0039152000	123.44920	-65.785065	3005.2190	Potter
6461.4951	-53.867085	-0.23548600	0.0029029001	2.2922602	0.0049190000	230.21156	-18.347893	2841.0061	Teide
6463.4863	-61.073956	-0.18220110	0.0013953000	2.2327371	0.0022636000	154.61446	-67.456497	2923.5508	Teide
6463.5859	-60.471527	-0.17588170	0.0014407000	2.2318656	0.0023342001	144.74760	-64.334343	2929.5503	Teide
6463.6709	-63.572220	-0.16122550	0.00098380004	2.2227952	0.0015801000	141.27846	-85.754303	2950.3315	Teide
6463.6816	-61.769299	-0.17149810	0.0022253001	2.2357566	0.0036106000	152.53139	-75.563927	2940.6848	Potter
6464.4756	-54.030792	-0.21212681	0.0024546999	2.2581608	0.0040652999	178.64835	-39.234600	2831.1321	Teide
6464.6567	-55.230083	-0.22004570	0.0025779000	2.2562256	0.0042662998	166.22636	-34.619335	2897.6431	Teide
6465.4722	-59.819408	-0.21044791	0.0014840000	2.2374344	0.0024290001	161.30566	-45.724197	2971.3567	Teide
6467.5957	-59.653393	-0.17423870	0.0036702999	2.2260733	0.0059262002	112.25697	-80.010002	2898.6897	Potter

Continued on next page

Table II.I – continued from previous page

HJD - 2450000	EW	SKEWNESS	SKEW ERR	KURTOSIS	KURT ERR	BISECTOR	FLUX VEL	FWHM	OBSERVER
6467.6748	-59.848007	-0.18342949	0.0022330000	2.2185996	0.0035919000	140.21687	-72.935829	2922.1643	Potter
6467.7529	-58.848274	-0.17681301	0.0026262000	2.2164903	0.0042129001	135.72787	-79.675163	2930.2349	Potter
6468.6001	-59.086948	-0.17129891	0.0025710999	2.2086966	0.0041045998	108.67224	-84.324326	2900.1980	Potter
6468.6709	-60.292198	-0.16176870	0.0014535000	2.2074003	0.0023135999	113.48098	-91.001808	2930.7131	Potter
6469.0000	-62.980324	-0.17713490	0.00040009999	2.2279193	0.00064629997	139.14330	-81.359474	2934.4800	NOT
6468.7524	-60.135231	-0.16466390	0.0028258001	2.2223377	0.0045411000	137.59512	-89.660416	2891.6296	Potter
6471.8286	-60.070045	-0.18865719	0.0012671000	2.2255101	0.0020460000	118.64844	-71.522614	2897.1128	DAO
6472.5454	-57.567623	-0.18990730	0.0022464001	2.2040408	0.0035734000	187.26498	-71.925346	2851.6311	Teide
6472.6665	-58.178867	-0.19493330	0.0021363001	2.2210522	0.0034370001	208.49973	-66.777420	2794.7380	Teide
6472.8057	-62.413643	-0.17943910	0.0019848000	2.2379951	0.0032287000	177.70293	-68.636574	2939.0305	DAO
6473.4766	-58.659340	-0.16696370	0.0020615000	2.2262919	0.0033229999	144.20351	-81.099106	2894.5845	Teide
6473.5713	-61.127712	-0.15222850	0.0014422000	2.2140586	0.0023054001	110.24128	-92.392265	2961.5181	Teide
6473.7861	-61.616562	-0.19249180	0.0012441000	2.2363396	0.0020244999	152.84267	-65.154625	2966.2671	DAO
6473.8145	-61.964523	-0.19435769	0.0011749000	2.2360823	0.0019118000	155.05904	-64.635506	2958.4504	DAO
6473.8604	-61.446075	-0.19457211	0.0011259000	2.2356136	0.0018315000	151.72014	-65.984917	2935.0137	DAO
6473.8853	-61.429722	-0.19456880	0.0010965000	2.2352717	0.0017829000	152.89661	-66.662216	2926.5681	DAO
6473.9268	-60.964317	-0.19401731	0.0011881000	2.2325652	0.0019282000	154.58504	-64.747002	2921.0874	DAO
6473.9497	-61.142612	-0.19344810	0.0010978000	2.2328014	0.0017816999	153.80887	-65.148422	2921.8557	DAO
6474.5503	-55.252110	-0.19974190	0.0028367999	2.1921058	0.0044832001	161.62672	-72.181702	2875.3296	Teide
6474.6348	-61.339157	-0.18307330	0.0012256000	2.2174757	0.0019691000	117.48516	-74.891769	3022.0002	Teide
6474.7441	-63.989662	-0.19000450	0.0012709000	2.2317462	0.0020621000	164.30042	-61.601654	3010.3748	DAO
6474.7695	-63.496342	-0.18908750	0.0012899000	2.2336054	0.0020949000	169.42058	-62.567032	2978.0161	DAO
6474.8315	-62.748154	-0.18918779	0.0013897000	2.2350988	0.0022585001	153.17416	-65.744415	2946.3293	DAO
6474.8564	-62.102097	-0.18997081	0.0014053000	2.2353158	0.0022835999	153.86407	-65.552299	2927.6248	DAO
6474.9038	-62.756737	-0.19163319	0.0011485000	2.2388003	0.0018708000	177.33182	-61.279991	2928.1316	DAO
6474.9282	-62.151657	-0.18696840	0.0011149000	2.2368531	0.0018128000	167.99068	-65.134865	2919.5808	DAO
6474.9551	-61.446991	-0.18136691	0.0011512000	2.2363379	0.0018703000	159.67432	-68.439941	2915.7224	DAO
6475.4653	-59.402950	-0.17290460	0.0017123000	2.2133522	0.0027425000	100.94471	-77.457947	2980.5188	Teide
6475.4653	-59.402950	-0.17290460	0.0017123000	2.2133522	0.0027425000	100.94471	-77.457947	2980.5188	Teide
6475.6895	-61.737610	-0.15850630	0.0013017000	2.2486756	0.0021293000	94.857735	-83.163841	2986.6304	Teide
6475.7324	-60.663475	-0.17162320	0.0017480000	2.2372220	0.0028393001	165.14304	-77.844681	2925.8904	DAO
6475.7588	-59.914364	-0.17193051	0.0015248000	2.2360804	0.0024751001	154.09065	-77.796425	2902.6194	DAO
6475.8008	-60.277912	-0.17073800	0.0014633000	2.2338479	0.0023717999	148.42230	-80.407768	2900.4583	DAO
6475.8257	-61.167042	-0.17750680	0.0013589000	2.2352216	0.0022058000	158.28616	-76.119865	2917.3325	DAO
6475.9082	-61.500679	-0.18035960	0.0015266000	2.2329068	0.0024750000	154.74770	-72.954620	2925.9395	DAO
6476.4771	-61.170277	-0.17932869	0.0014808000	2.2313623	0.0023993000	83.015663	-76.625511	2986.3010	Teide
6476.5840	-58.566818	-0.20188650	0.0022392999	2.2340403	0.0036386999	139.10081	-64.462341	2896.8147	Teide
6476.7329	-61.370098	-0.20302939	0.0012534000	2.2336395	0.0020401999	160.15082	-59.983967	2954.6152	DAO
6476.7705	-61.716354	-0.20303530	0.0011580000	2.2328091	0.0018835000	161.20648	-60.149998	2954.4929	DAO
6476.7949	-61.897858	-0.20313290	0.0012218000	2.2323050	0.0019862000	162.52312	-61.747631	2960.3494	DAO
6476.8472	-62.383507	-0.19990160	0.0011020000	2.2333417	0.0017921000	159.78297	-61.570347	2984.5679	DAO
6476.9404	-63.088787	-0.19952010	0.0012254000	2.2412326	0.0020012001	174.59097	-59.529057	2976.2849	DAO
6476.9639	-63.092533	-0.19666210	0.0012713000	2.2418246	0.0020763001	174.34077	-60.623360	2975.6399	DAO

Continued on next page

Table II.I – continued from previous page

HJD - 2450000	EW	SKEWNESS	SKEW ERR	KURTOSIS	KURT ERR	BISECTOR	FLUX VEL	FWHM	OBSERVER
6477.7275	-61.392281	-0.18066220	0.0012183000	2.2145002	0.0019533001	164.83333	-78.027855	2922.7981	DAO
6477.7622	-61.481678	-0.17817581	0.0020405001	2.2162635	0.0032736999	162.26283	-79.305092	2901.4324	DAO
6477.8257	-60.559711	-0.17636110	0.0013779000	2.2194924	0.0022137000	165.88309	-78.027565	2890.4441	DAO
6477.9497	-61.744537	-0.17945360	0.0013035000	2.2351506	0.0021162000	165.77399	-75.858658	2937.8086	DAO
6478.4004	-60.504215	-0.16410390	0.0030091000	2.2244706	0.0048457999	118.58092	-86.850273	2953.3396	Teide
6478.4888	-61.261627	-0.16677129	0.0029098000	2.2272220	0.0046983999	111.52592	-84.416290	2963.9539	Teide
6478.5669	-58.995338	-0.17762430	0.0020143001	2.2137814	0.0032233000	116.48006	-82.019386	2910.6829	Potter
6478.5889	-59.358070	-0.17583521	0.0014550000	2.2224867	0.0023413000	84.158859	-83.517776	2942.5007	Teide
6478.6641	-59.373257	-0.17754640	0.0013429000	2.2177532	0.0021543000	99.678078	-84.140877	2910.8259	Potter
6478.6714	-60.072083	-0.17450680	0.0012097000	2.2284923	0.0019545001	76.238716	-83.118568	2950.1438	Teide
6478.7261	-60.423809	-0.18968511	0.0013784000	2.2254899	0.0022260000	139.79184	-69.203125	2923.3621	DAO
6478.7573	-61.307755	-0.18333690	0.0014090000	2.2174199	0.0022612000	134.38776	-77.477089	2941.3958	Potter
6478.7749	-60.370537	-0.19222420	0.0010045000	2.2234483	0.0016207000	151.89709	-68.117668	2920.1155	DAO
6478.8218	-60.228600	-0.19619440	0.0010588000	2.2272377	0.0017136000	160.85568	-64.882927	2913.5559	DAO
6478.9414	-59.014584	-0.19479930	0.0011936000	2.2200468	0.0019232000	164.07167	-64.525078	2918.0383	DAO
6478.9653	-59.546341	-0.19036020	0.0012667000	2.2202346	0.0020403999	164.00023	-63.760170	2931.5950	DAO
6479.4692	-62.013096	-0.18253760	0.0010405000	2.2431252	0.0016992000	143.03835	-70.774857	2926.5945	Teide
6479.6475	-55.653015	-0.20360430	0.0034520000	2.2336063	0.0056015998	234.49467	-62.380646	2644.5852	Teide
6479.7222	-61.675159	-0.18057489	0.0011259000	2.2398963	0.0018334000	156.58562	-72.581467	2876.9014	DAO
6479.7549	-61.984352	-0.18418160	0.0012341000	2.2379251	0.0020087000	156.18056	-69.458931	2897.1460	DAO
6479.7847	-62.218941	-0.18181799	0.0012094000	2.2367713	0.0019668001	146.01924	-70.842278	2911.4404	DAO
6479.8286	-61.726856	-0.18442570	0.0012003999	2.2366910	0.0019528000	138.56770	-70.343132	2917.3181	DAO
6479.9434	-61.569427	-0.17304310	0.0012117000	2.2199392	0.0019484001	122.39507	-75.370842	2956.7263	DAO
6479.9648	-62.069050	-0.17301691	0.0010746000	2.2208323	0.0017288000	119.69964	-76.561310	2974.1514	DAO
6480.4385	-62.892868	-0.15870760	0.00087240001	2.2440670	0.0014215000	99.103004	-90.286247	2951.1672	Teide
6480.5400	-60.756481	-0.17495009	0.0015487000	2.2287154	0.0025003001	136.06107	-81.453369	2898.7832	Teide
6480.6143	-63.106480	-0.16470049	0.00081509998	2.2504666	0.0013342000	109.02478	-84.571198	2942.6055	Teide
6480.7197	-61.960876	-0.19776841	0.0011546999	2.2413440	0.0018849000	170.90672	-66.825424	2897.8401	DAO
6480.7524	-60.970055	-0.19848239	0.0010746000	2.2375064	0.0017500001	164.37556	-68.375214	2884.4434	DAO
6480.7817	-61.596737	-0.19664820	0.0011451000	2.2382598	0.0018656000	152.83002	-69.096024	2901.8250	DAO
6480.8267	-62.144264	-0.19370300	0.0010749000	2.2402573	0.0017535000	143.31129	-69.417130	2931.3252	DAO
6480.9512	-62.928215	-0.18688220	0.0010493000	2.2290206	0.0016993000	127.51490	-66.874809	2992.9312	DAO
6481.4067	-58.055309	-0.21008770	0.0020971000	2.2210217	0.0033787999	207.38998	-63.875156	2849.4011	Teide
6481.5132	-59.045643	-0.19747780	0.0016431001	2.2265162	0.0026538000	177.90891	-69.115440	2912.7971	Teide
6481.5972	-60.187790	-0.18308771	0.0011391999	2.2275898	0.0018398000	135.40331	-75.939812	2933.1438	Teide
6481.6743	-56.764133	-0.19900860	0.0020405999	2.2190380	0.0032800999	189.07590	-65.475655	2817.5237	Teide
6481.7227	-60.259090	-0.18503590	0.0011089999	2.2328551	0.0017981000	176.77910	-68.384491	2912.6807	DAO
6481.7544	-61.302715	-0.18350060	0.0011860000	2.2347667	0.0019252000	172.81750	-69.499016	2944.5730	DAO
6481.7769	-61.251434	-0.18764740	0.0010966000	2.2338433	0.0017801001	185.83795	-65.528381	2959.0967	DAO
6481.8208	-60.466393	-0.18188471	0.0012624000	2.2336521	0.0020472000	182.78110	-69.793640	2921.7800	DAO
6481.9316	-62.180138	-0.18850470	0.0011932000	2.2478063	0.0019541001	180.06628	-65.613525	2910.3594	DAO
6481.9536	-61.939926	-0.19071220	0.0011131000	2.2509272	0.0018274999	181.92564	-63.383450	2909.0459	DAO
6482.3579	-62.990719	-0.20389929	0.0028234001	2.2377439	0.0046017002	218.90782	-56.552921	2906.5117	Ondrejov

Continued on next page

Table II.I – continued from previous page

HJD - 2450000	EW	SKEWNESS	SKEW ERR	KURTOSIS	KURT ERR	BISECTOR	FLUX VEL	FWHM	OBSERVER
6482.3770	-62.463387	-0.20185129	0.0020457001	2.2360764	0.0033290000	222.24348	-60.030804	2878.1934	Ondrejov
6482.3867	-61.511814	-0.20252220	0.0022030999	2.2360108	0.0035858001	204.61978	-56.566105	2881.9607	Ondrejov
6482.3955	-59.895100	-0.20008120	0.0020911000	2.2329876	0.0033950999	209.11203	-61.143028	2841.0984	Ondrejov
6482.4043	-62.683731	-0.19988140	0.0019716001	2.2366524	0.0032087001	206.20419	-60.277851	2901.3611	Ondrejov
6482.5664	-60.159622	-0.20059660	0.0026789000	2.2425518	0.0043784999	188.76714	-57.346111	2866.0134	Ondrejov
6482.5752	-62.718002	-0.20935160	0.0028160999	2.2488134	0.0046263998	192.48970	-50.039291	2906.2207	Ondrejov
6482.7246	-63.040485	-0.16854720	0.0011704999	2.2380297	0.0019016000	137.70587	-80.024559	2936.5366	DAO
6482.7578	-62.234959	-0.16926689	0.0011401000	2.2370405	0.0018508000	132.40691	-80.367493	2930.5085	DAO
6482.7798	-62.613293	-0.17038980	0.0011255000	2.2380798	0.0018282000	134.81705	-80.069405	2944.0864	DAO
6482.8218	-63.409622	-0.17223860	0.0012632000	2.2378817	0.0020520999	133.71155	-79.030998	2957.3054	DAO
6482.9321	-62.545990	-0.18803670	0.0011202000	2.2408528	0.0018264001	148.40985	-70.939941	2939.2900	DAO
6482.9561	-63.186871	-0.18517549	0.0011011000	2.2418618	0.0017961001	137.52155	-73.089958	2942.1074	DAO
6483.4717	-61.449081	-0.23435950	0.0017891000	2.2367134	0.0029289001	219.85437	-37.563374	2950.6921	Ondrejov
6483.4790	-63.098389	-0.23223390	0.0019690001	2.2338352	0.0032168000	222.54672	-37.514233	3001.4993	Ondrejov
6483.5762	-61.836918	-0.23092569	0.0022728001	2.2313004	0.0037048999	220.61646	-40.739952	2965.7395	Ondrejov
6483.5835	-62.402378	-0.23028140	0.0022472001	2.2295437	0.0036583000	224.48235	-40.537376	2962.7893	Ondrejov
6485.7002	-61.068787	-0.19825760	0.0014224000	2.2226717	0.0022988999	148.46709	-64.036354	2963.8423	OMM
6485.7769	-60.476231	-0.20865589	0.0012356000	2.2209537	0.0019969000	188.77734	-55.131519	2957.4919	OMM
6486.5430	-63.569256	-0.17481640	0.0040513999	2.2339103	0.0065686000	133.06569	-78.214630	2953.4377	Leadbeater
6486.5649	-66.825409	-0.18073259	0.0041238000	2.2349091	0.0066956999	144.90211	-74.478966	3018.7871	Leadbeater
6487.4326	-63.213196	-0.16014311	0.00097380002	2.2545607	0.0015962000	75.322182	-96.190414	2895.4934	Teide
6487.4717	-65.700615	-0.23475130	0.0023451999	2.2492566	0.0038652001	236.19644	-35.187286	2964.2993	Ondrejov
6487.5293	-59.256302	-0.17960830	0.0016970000	2.2280028	0.0027377000	115.93427	-87.206718	2807.7573	Teide
6488.5747	-62.259209	-0.18487421	0.0017390000	2.2327991	0.0028206999	183.45744	-68.312309	2979.5122	OMM
6488.6138	-62.695118	-0.18668200	0.0016359000	2.2357578	0.0026589001	181.49776	-67.619102	2976.2532	OMM
6488.6626	-60.890244	-0.19540550	0.0017186000	2.2379816	0.0027997000	193.55865	-61.069115	2919.2881	OMM
6488.6665	-60.683983	-0.17992240	0.0017891000	2.2323332	0.0028986000	163.19946	-75.288017	2916.1370	Teide
6489.4473	-60.845150	-0.19383870	0.0020018001	2.2264738	0.0032360000	177.62701	-66.878845	2931.9685	Leadbeater
6489.5713	-59.235050	-0.17821170	0.0014630000	2.2180593	0.0023457000	131.40506	-82.616241	2915.2239	Potter
6489.6504	-59.170654	-0.17829570	0.0013031000	2.2238340	0.0020979000	137.50211	-79.546844	2894.3210	Potter
6489.6733	-58.781380	-0.20398220	0.0015572000	2.2267404	0.0025196001	181.67639	-62.762039	2879.2476	OMM
6489.7256	-59.171070	-0.18799689	0.0014085000	2.2264702	0.0022747000	167.85675	-71.493378	2871.0918	Potter
6489.7456	-58.642708	-0.20021920	0.0015564000	2.2298939	0.0025220001	174.03416	-66.646866	2850.1929	OMM
6489.8071	-59.146927	-0.20458800	0.0016621000	2.2324622	0.0027002001	180.75531	-63.823364	2844.9761	OMM
6490.1040	-61.943291	-0.18753821	0.0022984999	2.2278543	0.0037201999	133.04935	-73.520164	2941.9099	Li
6490.1777	-63.640335	-0.18887401	0.0017084000	2.2313595	0.0027715999	149.93230	-68.516838	2992.1382	Li
6490.4390	-60.696373	-0.19637880	0.0012832000	2.2239270	0.0020734000	150.19643	-66.561829	2994.7600	Teide
6490.5898	-62.705769	-0.17219789	0.0017857000	2.2200716	0.0028673001	145.33942	-87.956718	2984.9348	Potter
6490.5996	-62.212666	-0.19238280	0.0023953000	2.2260764	0.0038709999	183.89542	-65.746582	2981.7925	OMM
6490.6948	-62.891171	-0.18888129	0.0022317001	2.2347789	0.0036263999	195.36037	-65.062126	3000.4565	OMM
6490.7490	-63.386974	-0.17292890	0.0015164000	2.2262750	0.0024462999	149.03378	-81.803894	3022.4578	Potter
6490.7529	-62.880268	-0.18244781	0.0019596000	2.2360575	0.0031852999	180.49342	-67.240509	3017.7676	OMM
6491.5615	-58.776646	-0.18883820	0.0016396000	2.2322371	0.0026583001	165.77930	-70.990654	2853.2607	Teide

Continued on next page

Table II.I – continued from previous page

HJD - 2450000	EW	SKEWNESS	SKEW ERR	KURTOSIS	KURT ERR	BISECTOR	FLUX VEL	FWHM	OBSERVER
6491.6328	-61.290882	-0.17137210	0.0016262000	2.2301881	0.0026304000	131.86964	-84.379486	2908.6816	Potter
6491.7168	-59.843174	-0.18811370	0.0014466000	2.2433746	0.0023624001	160.48161	-70.904892	2844.9346	Teide
6491.7441	-61.065689	-0.17552100	0.0016444999	2.2180543	0.0026380999	155.52007	-86.933189	2870.5312	Potter
6492.4287	-62.162563	-0.20625231	0.0029517999	2.2287624	0.0047900002	156.04921	-61.330044	2955.2710	Leadbeater
6492.4390	-61.774750	-0.20623749	0.0035071000	2.2274177	0.0056860000	149.87788	-63.196819	2957.7827	Leadbeater
6494.6631	-61.034164	-0.18893890	0.0016619000	2.2285583	0.0026922000	134.70839	-72.774826	2953.5342	OMM
6494.7295	-61.030743	-0.18269120	0.0018474000	2.2210989	0.0029762001	142.62715	-68.806885	2975.0488	OMM
6494.7607	-61.035046	-0.19233520	0.0017415000	2.2210543	0.0028084000	165.96449	-61.678017	2980.2561	OMM
6494.8154	-61.949772	-0.18623079	0.0018071000	2.2203152	0.0029112999	151.09103	-66.591835	2995.6309	OMM
6495.6299	-60.253887	-0.19509380	0.0016982000	2.2376010	0.0027656001	151.92358	-67.285866	2923.9050	OMM
6495.7046	-59.679531	-0.18255880	0.0017774000	2.2275989	0.0028733001	129.05067	-76.090691	2919.8745	OMM
6495.7627	-60.774464	-0.17554741	0.0016364000	2.2232513	0.0026352000	152.08932	-74.656326	2913.7422	OMM
6495.8032	-60.763031	-0.16554300	0.0017571000	2.2182097	0.0028166999	141.95341	-83.050880	2917.1848	OMM
6496.6006	-61.182762	-0.20172630	0.0044177002	2.2212510	0.0071214000	168.57233	-71.577377	2921.3391	Strachan
6497.1641	-62.207184	-0.18363230	0.0033603001	2.2269611	0.0054338998	142.26463	-76.427635	2995.3765	Li
6497.2310	-64.506516	-0.18578020	0.0049121999	2.2371569	0.0079949005	146.04929	-72.540192	3032.7708	Li
6497.2773	-64.794815	-0.18376960	0.0053539998	2.2382886	0.0087138005	154.20444	-71.391914	3037.6848	Li
6497.3496	-62.199577	-0.22543509	0.0014488000	2.2353568	0.0023638001	254.39357	-44.212811	2943.5291	Ondrejov
6497.5391	-62.302517	-0.22432961	0.0015523999	2.2503254	0.0025563000	236.58101	-44.447105	2928.9807	Ondrejov
6498.1094	-64.578835	-0.17079890	0.0034707000	2.2247894	0.0055922000	143.46509	-82.023262	2979.9785	Li
6498.1592	-61.502438	-0.16703540	0.0033308000	2.2213957	0.0053511001	144.02563	-87.455460	2948.7395	Li
6498.2114	-61.446407	-0.16913740	0.0031971000	2.2255692	0.0051513002	153.26144	-87.235817	2924.5706	Li
6498.4023	-60.970669	-0.16872279	0.0036826001	2.2252605	0.0059372000	116.97846	-87.938652	2922.1267	Strachan
6499.3447	-63.506023	-0.23114219	0.0015317000	2.2441525	0.0025193000	221.03220	-36.244003	2972.5872	Ondrejov
6499.3545	-62.602158	-0.18722770	0.0018820000	2.2322991	0.0030556000	137.13120	-74.995491	2980.5063	Strachan
6499.4419	-63.473965	-0.18607950	0.0019059000	2.2259490	0.0030821001	133.73924	-74.108398	3029.4675	Strachan
6499.5088	-65.261658	-0.22316471	0.0015729000	2.2344086	0.0025675001	226.62094	-42.095566	3037.6980	Ondrejov
6499.6885	-62.592983	-0.18109991	0.0017782000	2.2332609	0.0028853000	166.35513	-72.944565	2963.5537	Teide
6500.5610	-61.588402	-0.17296940	0.0013706000	2.2308011	0.0022162001	147.77191	-83.761101	2890.3203	Potter
6500.6313	-61.791492	-0.16875070	0.0015623000	2.2373090	0.0025362000	129.74738	-86.716553	2920.1226	Potter
6500.7075	-62.441982	-0.16430600	0.0014467000	2.2341795	0.0023439999	143.10033	-85.579414	2960.4531	Potter
6501.4297	-60.530983	-0.18852440	0.0012787000	2.2269239	0.0020679000	113.70551	-74.644768	2893.7949	Teide
6501.5444	-60.883144	-0.18786120	0.0014147999	2.2252228	0.0022865001	132.47762	-73.283936	2915.2793	Teide
6501.6401	-63.679028	-0.18661740	0.0013377001	2.2284667	0.0021664000	119.46307	-73.814445	3020.1316	Teide
6502.5239	-60.991169	-0.18064369	0.0012033000	2.2325938	0.0019519000	117.02227	-76.161346	2917.0779	Teide
6502.6030	-60.979053	-0.17442180	0.00093659997	2.2260528	0.0015111000	141.41827	-81.143555	2882.0710	Teide
6502.6836	-62.018974	-0.17508671	0.0010020999	2.2269068	0.0016174000	167.77348	-80.973633	2867.2568	Teide
6503.3384	-60.316582	-0.19108030	0.0014472000	2.2296236	0.0023425000	126.86525	-78.502235	2889.6477	Strachan
6503.3853	-60.023033	-0.19227250	0.0020448000	2.2327487	0.0033174001	130.47656	-77.704140	2863.6360	Strachan
6503.4316	-60.496197	-0.19436631	0.0014560000	2.2352216	0.0023672001	124.57029	-73.224770	2886.3052	Strachan
6503.4487	-60.474102	-0.18325099	0.0014088000	2.2316494	0.0022823999	111.26031	-81.014420	2854.6753	Teide
6503.4761	-60.976650	-0.19696730	0.0015852000	2.2377410	0.0025820001	125.02267	-73.254814	2894.2949	Strachan
6503.5371	-60.089336	-0.18520890	0.0012299001	2.2297533	0.0019908000	101.63320	-80.337624	2890.0457	Teide

Continued on next page

Table II.I – continued from previous page

HJD - 2450000	EW	SKEWNESS	SKEW ERR	KURTOSIS	KURT ERR	BISECTOR	FLUX VEL	FWHM	OBSERVER
6503.5649	-60.454063	-0.19234610	0.0013562000	2.2172599	0.0021786001	110.35085	-79.948708	2917.7869	Potter
6503.6377	-60.479347	-0.18098649	0.0019938000	2.2123334	0.0031884999	99.499672	-81.971458	2930.2563	Potter
6503.6538	-59.564232	-0.18490580	0.0010568000	2.2165685	0.0016965000	110.58375	-79.299911	2913.1489	Teide
6503.7153	-60.823944	-0.18754929	0.0013764000	2.2159441	0.0022100999	128.19170	-76.607018	2938.2490	Potter
6504.3667	-62.134106	-0.18066810	0.0028261000	2.2439103	0.0046148002	156.21169	-73.678284	2942.0154	Strachan
6504.4126	-62.069599	-0.16664749	0.0029192001	2.2356839	0.0047320002	136.44257	-85.835190	2943.5994	Strachan
6504.4580	-61.632557	-0.17031610	0.0025754999	2.2383132	0.0041820002	151.16856	-82.704056	2922.7710	Strachan
6504.4648	-61.626102	-0.17469960	0.00093789998	2.2451096	0.0015303000	153.31978	-77.345085	2927.1216	Teide
6504.5479	-61.816998	-0.17735180	0.00089680002	2.2487566	0.0014667000	171.14153	-77.083786	2897.3926	Teide
6504.6338	-62.282345	-0.18003480	0.00098040001	2.2564814	0.0016133999	142.98929	-74.525955	2890.2046	Teide
6504.7119	-63.958904	-0.18758090	0.0024782000	2.2710538	0.0041232002	133.24902	-63.593979	2888.8501	Teide
6505.4019	-63.981457	-0.19395530	0.0017880000	2.2255592	0.0028895000	161.12088	-69.647026	2988.5977	Strachan
6505.4468	-63.201012	-0.18088029	0.0021068000	2.2315722	0.0034117999	129.92575	-80.972939	2935.6733	Strachan
6505.4507	-60.510311	-0.18184289	0.0019707000	2.2280939	0.0031848999	136.43118	-79.396408	2897.3188	Teide
6505.4927	-63.188129	-0.19124480	0.0021180999	2.2309115	0.0034324999	145.40556	-75.260773	2920.4099	Strachan
6505.5386	-60.383968	-0.19002099	0.0011848001	2.2362225	0.0019262000	150.82706	-74.473038	2865.3567	Teide
6505.5430	-62.988369	-0.19257431	0.0018142000	2.2312369	0.0029412000	157.73730	-70.690338	2915.9197	Strachan
6506.3374	-63.170876	-0.18290780	0.0022340999	2.2218010	0.0035973999	157.35060	-77.791519	3018.6272	Strachan
6506.3623	-63.573044	-0.18826769	0.0023685000	2.2239606	0.0038202000	168.40791	-77.141273	3024.2908	Strachan
6508.4258	-60.921856	-0.19556110	0.0010864000	2.2302270	0.0017624000	147.79691	-67.342407	2967.2585	Teide
6508.5137	-62.233273	-0.19441681	0.0013099000	2.2416809	0.0021402000	154.66199	-67.691292	2972.2080	Teide
6508.5776	-62.423653	-0.19163190	0.0010954000	2.2444565	0.0017912000	163.64896	-70.602654	2950.1599	Teide
6508.6616	-63.848900	-0.18982591	0.0026310999	2.2508726	0.0043184999	170.71252	-70.149918	2956.7634	Teide
6509.4204	-60.581821	-0.18644600	0.0010523000	2.2314079	0.0017046999	164.02324	-74.829292	2847.4231	Teide
6509.4937	-59.707314	-0.18511660	0.0010485000	2.2370236	0.0017037001	182.30219	-75.290520	2811.3262	Teide
6509.5576	-60.989956	-0.17290510	0.0014537000	2.2262614	0.0023435000	150.45128	-85.947701	2884.0989	Potter
6509.5737	-60.268932	-0.18058580	0.00096330000	2.2415829	0.0015704000	164.90704	-74.730743	2849.0974	Teide
6509.6299	-61.366486	-0.17192300	0.0013606000	2.2316787	0.0022018999	137.91045	-84.704178	2899.8716	Potter
6510.3203	-61.557240	-0.23226950	0.0016322000	2.2344053	0.0026634999	201.60580	-47.930691	2860.9058	Ondrejov
6510.4351	-61.605904	-0.23547770	0.0016703000	2.2322974	0.0027246999	200.12700	-45.074188	2907.8105	Ondrejov
6510.5850	-61.899178	-0.23470131	0.0019274000	2.2365694	0.0031542000	232.55534	-39.216389	2923.6963	Ondrejov
6511.3975	-59.852131	-0.17725059	0.0022157000	2.2356901	0.0035961999	148.34534	-78.637245	2882.0562	Leadbeater
6511.4194	-59.618225	-0.17915690	0.0021653001	2.2344155	0.0035131001	142.94006	-79.975342	2871.1992	Leadbeater
6511.4375	-59.849842	-0.17688550	0.0025702000	2.2373779	0.0041760001	135.83461	-79.765305	2896.6101	Leadbeater
6511.4482	-59.582050	-0.18044411	0.0025430999	2.2383702	0.0041369000	143.58958	-77.102486	2864.4316	Leadbeater
6511.4634	-60.019402	-0.18031479	0.0022898000	2.2394013	0.0037285001	136.24310	-77.455833	2887.5649	Leadbeater
6512.4224	-63.422264	-0.18942490	0.0011600000	2.2392297	0.0018912000	119.44074	-75.964455	2895.5867	Teide
6512.5444	-63.424480	-0.20192780	0.0013066001	2.2430708	0.0021385001	133.94756	-66.556343	2894.0208	Teide
6512.6196	-63.445343	-0.19322351	0.0011817000	2.2353594	0.0019237000	125.82416	-72.826897	2928.5869	Teide
6512.6934	-63.220802	-0.19477829	0.0013654000	2.2363038	0.0022245999	126.95691	-70.851334	2946.5642	Teide
6513.3848	-64.633705	-0.17224979	0.0012154999	2.2377372	0.0019757000	147.77721	-79.736412	3024.8811	Teide
6513.5220	-61.866928	-0.17072110	0.0010492000	2.2361505	0.0017030000	133.87035	-79.805687	2979.7756	Teide
6513.5977	-64.425453	-0.16943540	0.0011102000	2.2414382	0.0018076000	128.64073	-84.178589	3009.1274	Teide

Continued on next page

Table II.I – continued from previous page

HJD - 2450000	EW	SKEWNESS	SKEW ERR	KURTOSIS	KURT ERR	BISECTOR	FLUX VEL	FWHM	OBSERVER
6514.3989	-62.589382	-0.17761740	0.0015599000	2.2486100	0.0025545000	93.859787	-83.139008	2952.2903	Teide
6514.6128	-61.137691	-0.18925540	0.0014588000	2.2309904	0.0023652001	132.56908	-76.638321	2900.6970	Teide
6514.6880	-61.711975	-0.19029850	0.0015899000	2.2306869	0.0025775000	138.48119	-77.012947	2889.3530	Teide
6515.4326	-60.897488	-0.18994340	0.0013474000	2.2302988	0.0021815000	167.03387	-74.599846	2948.4961	Teide
6515.4897	-61.325333	-0.18926960	0.0011913000	2.2343826	0.0019343999	179.99017	-71.851311	2931.3999	Teide
6515.5654	-60.235897	-0.18995669	0.0020526999	2.2381229	0.0033392000	214.72615	-71.445503	2846.5828	Teide
6516.3984	-60.496574	-0.18254641	0.0014612000	2.2336960	0.0023707000	121.95004	-78.064804	2927.4421	Teide
6516.4531	-62.696526	-0.17120500	0.0012593000	2.2379894	0.0020488999	93.724197	-84.531395	2986.6411	Teide
6516.6387	-59.843525	-0.18100570	0.0017521000	2.2393868	0.0028522999	126.58403	-79.848869	2890.9658	Teide
6518.3799	-60.397942	-0.17891040	0.0016486000	2.2361679	0.0026785000	115.55903	-81.255783	2891.8574	Teide
6518.5630	-56.855202	-0.20279470	0.0022627001	2.2182407	0.0036357001	217.70409	-67.964844	2778.1523	Teide
6518.6182	-57.270863	-0.19437911	0.0019968001	2.2143734	0.0031981000	190.30627	-74.211067	2813.0801	Teide
6519.3691	-58.908421	-0.18692020	0.0029094000	2.2363584	0.0047304002	74.509697	-80.617203	2943.8257	Teide
6519.5059	-59.422855	-0.18887711	0.0021215000	2.2261114	0.0034294999	131.54869	-77.849152	2879.3213	Teide
6519.5894	-59.094353	-0.20053101	0.0021205000	2.2333751	0.0034465000	141.11867	-68.931068	2883.2959	Teide
6520.4038	-64.290855	-0.16218990	0.0014063000	2.2478297	0.0022990999	124.88022	-87.866837	2962.9312	Teide
6520.5171	-63.966732	-0.15811740	0.0010579000	2.2357340	0.0017179000	71.020660	-89.871582	3004.4319	Teide
6520.6187	-61.755447	-0.16868210	0.0012868000	2.2185349	0.0020671000	108.14551	-86.968361	2943.4026	Teide
6521.4009	-56.756538	-0.22067870	0.0022932999	2.2394569	0.0037426001	199.34892	-59.332748	2733.1428	Teide
6521.4556	-59.526707	-0.19822040	0.0012696000	2.2373066	0.0020671000	128.81149	-74.052155	2845.4890	Teide
6521.5688	-60.082729	-0.19233461	0.0010927001	2.2334497	0.0017738000	116.79787	-78.899452	2852.1750	Teide
6522.3916	-62.868679	-0.17607020	0.0014476000	2.2521567	0.0023751999	145.96585	-78.657631	2947.4021	Teide
6522.5415	-62.185204	-0.17827210	0.0013948000	2.2517729	0.0022890000	145.68347	-74.549408	2962.3088	Teide
6523.3784	-59.755581	-0.18955310	0.0013557000	2.2417819	0.0022130001	122.07672	-74.092896	2877.5530	Teide
6523.4761	-59.668159	-0.18631691	0.0013240000	2.2324266	0.0021462999	123.73805	-78.597488	2876.0059	Teide
6523.6421	-60.463123	-0.19963171	0.0016253000	2.2397478	0.0026509000	154.38313	-70.024681	2846.0076	Teide
6524.4277	-63.368843	-0.18096200	0.0018456000	2.2464015	0.0030203999	128.92151	-76.491531	3005.2666	Teide
6524.5098	-60.961372	-0.18953580	0.0020912001	2.2422433	0.0034131999	145.48366	-71.422081	2944.7153	Teide
6524.6299	-62.917389	-0.18661830	0.0020802000	2.2616456	0.0034381000	146.04955	-69.223526	2972.6487	Teide
6528.4019	-65.568924	-0.16884740	0.0020122000	2.2464523	0.0032935000	73.556343	-90.704994	3002.5854	Teide
6528.5986	-65.803329	-0.17536120	0.0019318000	2.2470410	0.0031669000	87.824791	-81.292381	3054.8643	Teide
6529.4087	-57.695461	-0.19052190	0.0021813000	2.2464061	0.0035629999	194.38663	-80.506042	2778.5312	Teide
6529.4658	-59.939278	-0.19239371	0.0012852000	2.2449753	0.0021007999	157.35426	-73.770737	2833.3274	Teide
6529.6606	-57.846973	-0.19596200	0.0015821001	2.2372308	0.0025756999	134.46655	-69.198463	2853.2000	Teide
6530.4175	-59.575054	-0.20867270	0.0015905000	2.2341440	0.0025869999	172.48286	-66.003487	2820.9326	Teide
6530.4805	-58.493645	-0.20780601	0.0014300999	2.2330656	0.0023240999	165.61259	-67.747726	2806.2080	Teide
6530.6094	-60.788811	-0.19692720	0.0012589000	2.2377849	0.0020516999	127.56968	-73.799934	2898.2297	Teide
6531.4263	-65.433846	-0.16453150	0.0015310000	2.2613881	0.0025267999	112.37685	-85.788620	2998.1790	Teide
6531.5459	-66.380173	-0.15763950	0.0012014000	2.2657855	0.0019878000	103.76610	-89.576118	3010.0991	Teide
6532.3608	-58.516163	-0.18960010	0.0013103000	2.2332969	0.0021267000	126.97843	-76.243561	2861.1260	Teide
6532.4619	-58.414806	-0.18150580	0.0015044000	2.2235839	0.0024245000	123.50248	-82.106728	2856.8809	Teide
6532.5581	-63.562477	-0.16743070	0.00096500001	2.2441082	0.0015754000	88.964607	-90.384529	2942.0122	Teide
6533.5112	-65.756264	-0.17886101	0.00086889998	2.2523968	0.0014270000	122.22139	-77.879433	3038.4661	Teide

Continued on next page

Table II.I – continued from previous page

HJD - 2450000	EW	SKEWNESS	SKEW ERR	KURTOSIS	KURT ERR	BISECTOR	FLUX VEL	FWHM	OBSERVER
6533.6260	-60.868202	-0.19320419	0.0011292000	2.2408247	0.0018412000	166.63609	-69.014000	2897.5928	Teide
6534.4136	-62.795124	-0.18692321	0.0011154000	2.2438164	0.0018224000	146.95110	-77.141708	2917.0608	Teide
6534.5132	-62.382675	-0.18948001	0.00091280002	2.2451172	0.0014939000	134.81113	-73.478737	2940.1372	Teide
6534.6191	-60.987438	-0.18789950	0.0012920999	2.2432454	0.0021124000	111.53143	-74.214409	2923.7366	Teide
6535.1167	-65.032082	-0.19224340	0.0021003999	2.2362180	0.0034205001	137.33829	-75.615425	2939.5669	Li
6535.1587	-66.223900	-0.19024600	0.0021738000	2.2378211	0.0035439001	120.03124	-75.156952	2970.5505	Li
6535.2017	-65.375061	-0.18471140	0.0021283999	2.2341111	0.0034602000	113.44574	-78.070976	2990.9517	Li
6535.2451	-63.892723	-0.18257231	0.0031287000	2.2309306	0.0050745001	108.04412	-80.940956	2996.5508	Li
6535.3555	-62.001812	-0.18638811	0.0010825000	2.2217355	0.0017465000	110.44725	-76.816330	2987.0308	Teide
6535.4570	-61.354805	-0.19136150	0.0011474000	2.2223752	0.0018528000	120.52282	-71.957977	2996.1357	Teide
6535.5635	-60.324169	-0.18489639	0.00089949998	2.2350824	0.0014641000	114.52946	-73.166733	2954.7051	Teide
6536.4082	-65.001068	-0.17133340	0.0017374000	2.2592428	0.0028669001	89.180519	-82.750984	2954.0320	Teide
6536.5317	-67.489731	-0.15573309	0.0018470000	2.2460768	0.0030201001	86.735367	-93.136162	3019.6941	Teide
6536.6240	-66.834930	-0.17271890	0.0026954000	2.2491467	0.0044141002	108.04705	-91.515747	2971.4272	Teide
6537.4165	-63.180080	-0.17847469	0.0015000000	2.2443330	0.0024522000	86.191811	-87.348190	2943.3840	Teide
6537.5190	-59.105412	-0.21608910	0.0026884000	2.2413418	0.0043943999	138.83235	-61.807793	2905.5803	Teide
6537.6260	-66.665321	-0.18127970	0.0019006000	2.2480147	0.0031187001	63.354958	-81.784088	3070.9651	Teide
6538.3594	-64.605820	-0.18857171	0.0012700000	2.2650759	0.0021053001	155.72566	-66.995445	2983.8438	Teide
6538.4595	-64.796532	-0.18576230	0.0014417000	2.2641711	0.0023878000	146.27277	-70.305260	2954.9111	Teide
6538.5571	-63.693565	-0.19442780	0.0013689999	2.2683516	0.0022750001	147.79990	-65.243286	2930.2888	Teide
6539.3926	-64.372177	-0.17094480	0.0011357000	2.2425947	0.0018527000	77.575500	-91.470284	2983.6919	Teide
6539.4873	-61.818268	-0.18382880	0.0012556000	2.2429397	0.0020500000	112.61749	-83.779823	2900.3738	Teide
6539.5967	-60.306458	-0.19201951	0.0016653000	2.2340431	0.0027063000	122.75881	-74.051514	2916.4082	Teide
6540.4722	-65.337006	-0.18432079	0.00082740001	2.2517269	0.0013593000	150.57025	-74.799759	2963.6086	Teide
6540.5986	-65.126450	-0.18120380	0.00097589998	2.2539928	0.0016054000	143.27583	-76.169830	2962.9795	Teide
6541.3677	-60.685196	-0.22749980	0.0016603000	2.2496722	0.0027342001	187.06618	-53.566280	2898.6780	Ondrejov
6541.3760	-61.357323	-0.19269730	0.0015142000	2.2374449	0.0024643999	118.63622	-77.325310	2918.9897	Teide
6541.4790	-62.192120	-0.18509330	0.0013732000	2.2407115	0.0022382999	108.02535	-83.444931	2932.4419	Teide
6541.5059	-60.807423	-0.22695610	0.0022253999	2.2545540	0.0036766001	195.24934	-54.570789	2848.3596	Ondrejov
6541.5396	-64.939835	-0.18748130	0.0015687000	2.2428060	0.0025617999	128.67084	-81.568970	2933.7891	Potter
6541.6128	-65.079666	-0.18795960	0.0013901000	2.2461684	0.0022754001	127.05396	-79.408058	2955.1377	Potter
6542.3926	-64.614723	-0.17864950	0.0015173000	2.2414138	0.0024780999	83.383911	-80.188698	3060.5137	Teide
6542.4844	-64.124840	-0.17893609	0.0014142001	2.2368114	0.0023006999	143.49669	-80.634850	2981.0527	Teide
6542.5225	-64.922516	-0.17834590	0.0015959000	2.2306967	0.0025837000	141.52010	-82.489403	3013.5283	Potter
6542.5938	-64.753235	-0.18204430	0.0013893000	2.2332087	0.0022537000	142.08002	-77.957092	3011.8091	Potter
6542.6025	-65.932762	-0.17383340	0.0015841000	2.2508349	0.0025996999	90.498650	-82.486153	3050.3840	Teide
6542.6655	-63.743675	-0.17857620	0.0013166000	2.2355297	0.0021384000	149.97839	-79.926193	2999.2773	Potter
6544.3682	-64.988953	-0.18410160	0.0012390000	2.2457187	0.0020302001	85.616386	-80.634644	3013.3140	Teide
6544.4541	-58.857986	-0.20236990	0.0024643999	2.2100954	0.0039475001	140.75536	-67.727203	2956.0222	Teide
6544.5527	-63.507019	-0.18605150	0.0010778001	2.2321744	0.0017515999	94.150139	-75.692642	3038.3018	Teide
6545.3882	-65.503693	-0.17744650	0.0019950001	2.2553730	0.0032899999	113.43065	-72.023743	2997.8491	Teide
6545.4731	-63.095245	-0.17995140	0.0018428999	2.2439854	0.0030173999	103.32974	-70.462898	2998.3528	Teide
6545.5786	-65.348160	-0.17635480	0.0024875000	2.2491736	0.0040822001	97.033348	-75.398636	3063.9563	Teide

Continued on next page

Table II.I – continued from previous page

HJD - 2450000	EW	SKEWNESS	SKEW ERR	KURTOSIS	KURT ERR	BISECTOR	FLUX VEL	FWHM	OBSERVER
6546.0264	-66.268135	-0.18797010	0.0023274000	2.2480309	0.0038156000	126.51955	-77.403214	2986.7478	Li
6546.0825	-65.682625	-0.18250260	0.0031705000	2.2428989	0.0051779998	113.66336	-83.510284	2965.4673	Li
6546.4038	-61.036026	-0.19244990	0.0015489000	2.2336464	0.0025184001	99.758469	-74.165718	2936.6494	Teide
6546.4932	-63.643383	-0.18297809	0.0012175000	2.2370491	0.0019839001	91.769035	-81.157318	2966.4819	Teide
6546.6030	-64.937111	-0.17929460	0.0022374999	2.2331088	0.0036363001	82.542267	-83.388992	2997.9873	Teide
6547.3774	-61.170147	-0.19066960	0.0035019999	2.2612991	0.0057848999	142.96133	-71.216515	2894.2671	Teide
6548.5332	-62.932007	-0.18811411	0.0048026000	2.2436242	0.0078491000	132.00043	-79.426819	2884.2974	Teide
6549.4238	-62.855865	-0.18412749	0.0011802000	2.2457042	0.0019290000	131.73807	-80.129471	2979.5867	Teide
6549.5020	-63.873295	-0.17784190	0.00090789999	2.2530689	0.0014912999	124.80297	-81.498962	2980.6968	Teide
6549.5977	-57.334812	-0.19997500	0.0023924999	2.2302041	0.0038778000	165.84167	-64.362411	2894.4121	Teide
6550.1885	-65.123322	-0.17845280	0.0028595999	2.2314484	0.0046311999	170.25249	-77.728279	2951.8838	Li
6550.3672	-61.930752	-0.17753750	0.0010579000	2.2441578	0.0017262000	127.11568	-85.175667	2917.5735	Teide
6550.4517	-61.713299	-0.17694370	0.0010353000	2.2431796	0.0016886001	108.40527	-85.332581	2920.8411	Teide
6550.5352	-62.415913	-0.17937210	0.00099620002	2.2433529	0.0016264000	97.840645	-84.930527	2945.8789	Teide
6551.3999	-60.978947	-0.18947160	0.0015169000	2.2385697	0.0024724000	135.81364	-75.831543	2948.1289	Teide
6551.4790	-64.790543	-0.17206860	0.0012183000	2.2441461	0.0019904000	107.03655	-87.442596	3001.7649	Teide
6551.5835	-66.240623	-0.17180930	0.0012156999	2.2474387	0.0019900000	101.87906	-85.855309	3066.5298	Teide
6560.0508	-65.573502	-0.19432990	0.0025531000	2.2289784	0.0041409000	130.17570	-73.904694	3018.4924	Li
6560.0952	-65.485306	-0.18817590	0.0022972999	2.2257071	0.0037163999	120.15498	-76.899467	3042.2708	Li
6560.1372	-65.119179	-0.18608700	0.0020279000	2.2194057	0.0032663001	96.022926	-80.662994	3038.0066	Li
6560.1865	-61.063797	-0.18015251	0.0047239000	2.2160850	0.0075862999	77.058701	-87.731529	3019.9653	Li
6560.6353	-61.264923	-0.19203480	0.0018093000	2.2366350	0.0029428999	159.71910	-72.248611	2937.4224	OMM
6561.0322	-64.984985	-0.17658819	0.0024719001	2.2419295	0.0040318999	166.43028	-76.856346	2999.0647	Li
6561.0752	-65.697182	-0.17597070	0.0022462001	2.2448997	0.0036704000	162.30534	-77.654205	2974.8655	Li
6561.1177	-65.521133	-0.17617470	0.0034107999	2.2480791	0.0055840998	145.04546	-77.464500	2954.8601	Li
6561.6631	-64.417168	-0.12024310	0.0014096000	2.2392647	0.0022819000	41.230080	-122.98442	2939.3030	OMM
6562.0439	-64.809624	-0.19606850	0.0047730999	2.2428238	0.0078073000	132.30450	-75.369682	2930.5259	Li
6562.0859	-63.808830	-0.19625640	0.0062719001	2.2417202	0.010253000	132.45982	-73.181641	2912.8608	Li
6563.5737	-60.583164	-0.18217890	0.0014894000	2.2414248	0.0024295000	147.05066	-73.978958	2888.9531	OMM
6563.6050	-61.272202	-0.18522280	0.0015059001	2.2335997	0.0024458000	149.15732	-77.369942	2903.2603	OMM
6563.6836	-62.077797	-0.18232130	0.0017092000	2.2301991	0.0027683000	156.07745	-77.261040	2931.9788	OMM
6564.0322	-65.226791	-0.19139209	0.0034304999	2.2450902	0.0056139999	125.02145	-77.789383	2932.9104	Li
6564.0757	-65.437363	-0.19090180	0.0046114000	2.2489738	0.0075651999	109.89101	-77.411873	2962.5708	Li
6564.1187	-65.254662	-0.19421490	0.0063196998	2.2528241	0.010398900	122.53663	-73.727867	2968.3850	Li
6564.5352	-62.117577	-0.19287540	0.0015458000	2.2323184	0.0025132999	121.77564	-76.920937	2930.8010	OMM
6564.6011	-61.995441	-0.19118200	0.0019829001	2.2277048	0.0032142999	109.35891	-77.343292	2968.3076	OMM
6564.6714	-61.249588	-0.19303609	0.0018033000	2.2279572	0.0029233999	109.37758	-75.858696	2975.9973	OMM
6564.7417	-60.660824	-0.19199461	0.0019739000	2.2297311	0.0032041001	109.03210	-77.462364	2975.6274	OMM
6565.5083	-61.431396	-0.18223830	0.0013484000	2.2442582	0.0022026999	160.25017	-76.777397	2920.4353	OMM
6565.5527	-61.068508	-0.18200620	0.0014600999	2.2432423	0.0023830000	163.53856	-77.434814	2918.9631	OMM
6565.6025	-62.159370	-0.18274090	0.0012768999	2.2400579	0.0020804000	167.94952	-77.354263	2936.1621	OMM
6565.6572	-61.942112	-0.18992651	0.0015666001	2.2391107	0.0025533000	170.82310	-73.570702	2940.4446	OMM
6565.7021	-61.683826	-0.19004031	0.0015616000	2.2401505	0.0025468001	166.61726	-73.779755	2921.8181	OMM

Continued on next page

Table II.I – continued from previous page

HJD - 2450000	EW	SKEWNESS	SKEW ERR	KURTOSIS	KURT ERR	BISECTOR	FLUX VEL	FWHM	OBSERVER
6566.5464	-62.598476	-0.19834150	0.0011438000	2.2399197	0.0018671000	135.67819	-73.769493	2899.0269	OMM
6566.5933	-63.099598	-0.19341481	0.0014481000	2.2418706	0.0023660001	133.61140	-77.404434	2898.9827	OMM
6566.6421	-63.223587	-0.19181331	0.0017147000	2.2470157	0.0028115001	129.72690	-80.490463	2888.0542	OMM
6566.6855	-63.916782	-0.19791780	0.0012824000	2.2478487	0.0021051001	145.65192	-74.404549	2899.1555	OMM
6567.4932	-61.794865	-0.20423320	0.0011806000	2.2412488	0.0019296000	141.20743	-72.864914	2875.7483	OMM

Appendix III

Phased moments

The phased moments for the entire data set using the 2.255-day period. Each panel shows all 395 calculations as black dots for each moment, while also showing certain cycles as colored dots (see legends).

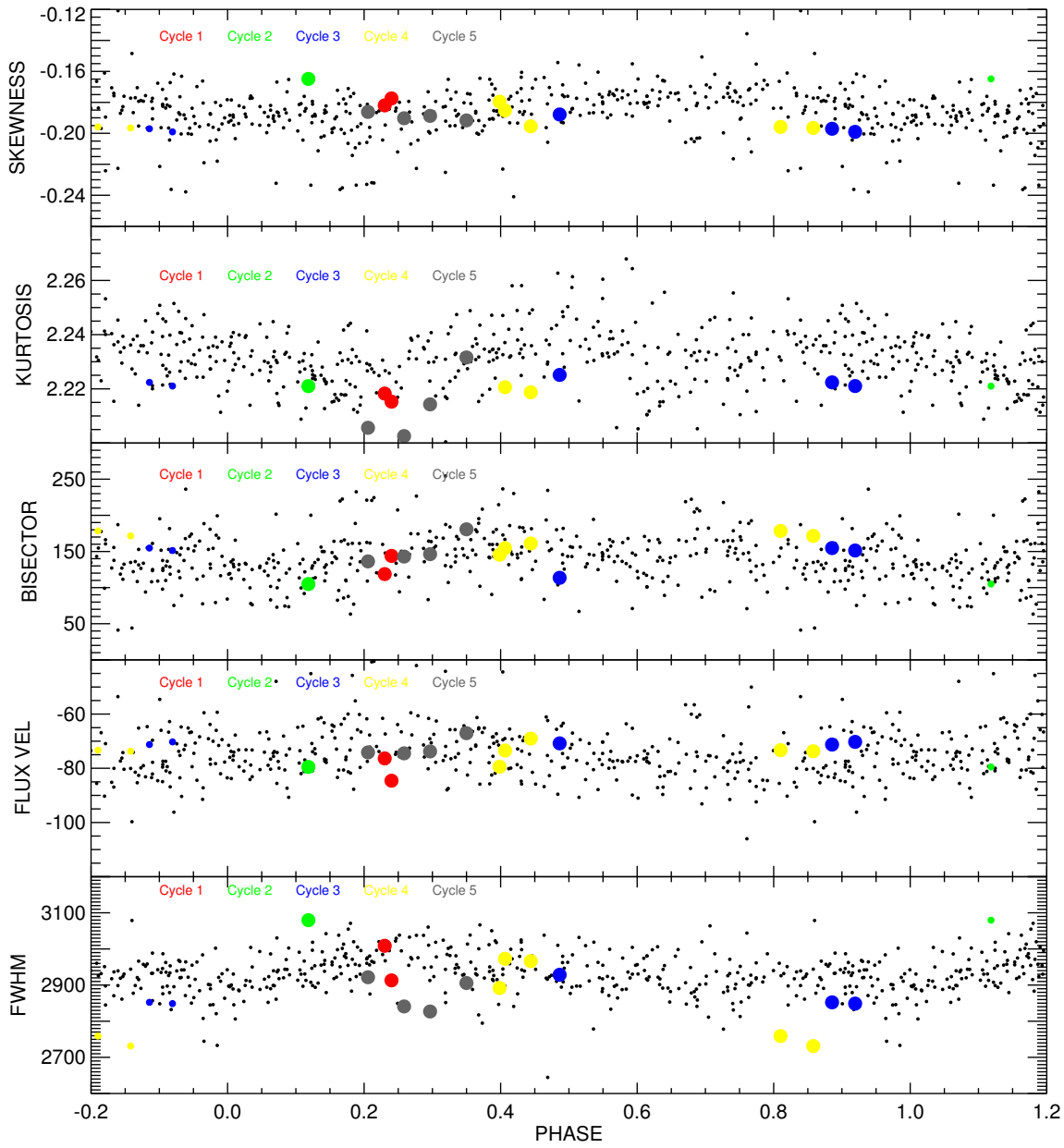
SKEWNESS
-0.12
-0.16
-0.20
-0.24
KURTOSIS
2.26
2.24
2.22
BISECTOR
250
150
50
FLUX VEL
-60
-80
-100
FWHM
3100
2900
2700
Cycle 1
Cycle 2
Cycle 3
Cycle 4
Cycle 5
-0.2
0.0
0.2
0.4
0.6
0.8
1.0
1.2
PHASE

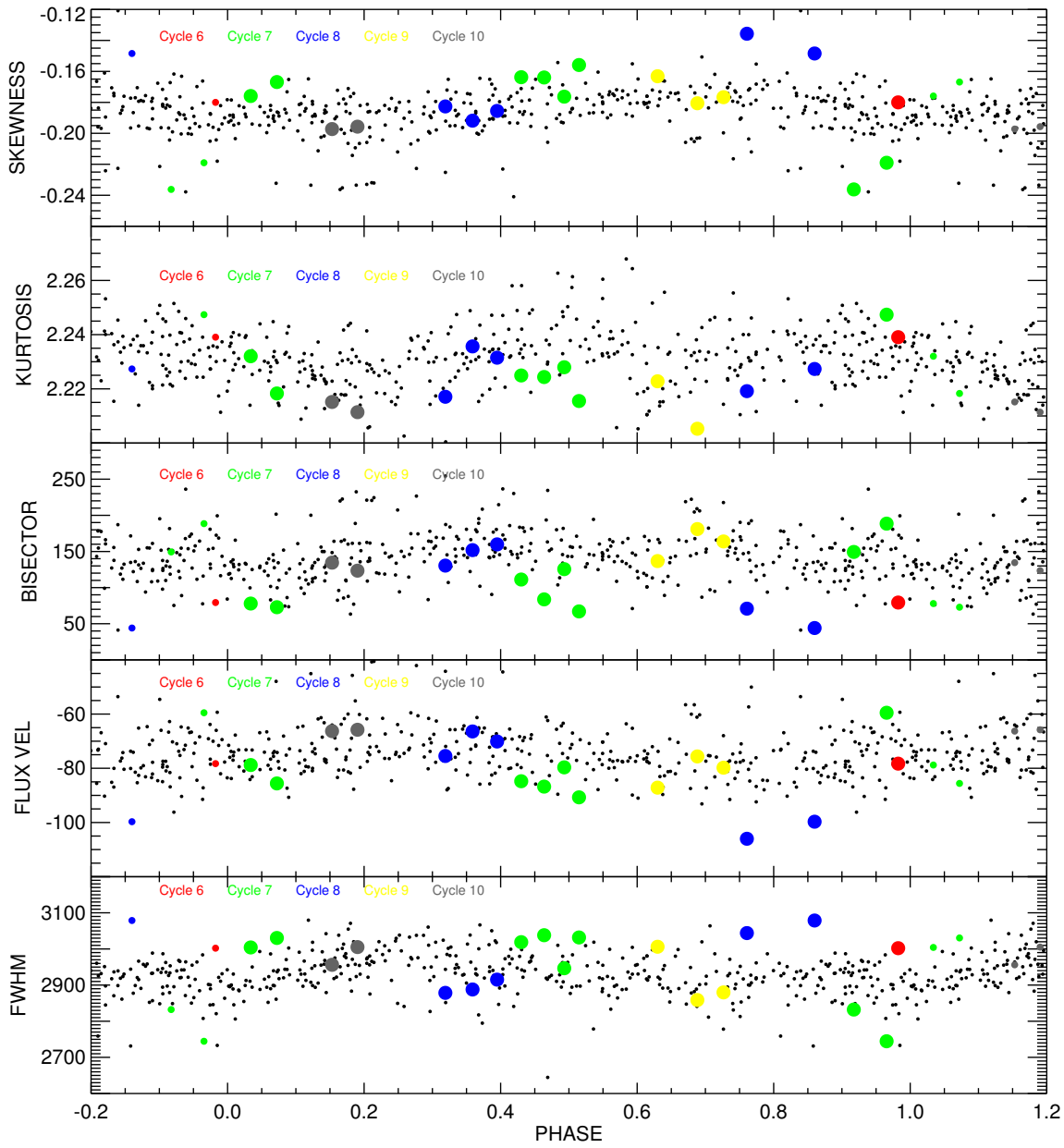
SKEWNESS
KURTOSIS
BISECTOR
FLUX VEL
FWHM
Cycle 6
Cycle 7
Cycle 8
Cycle 9
Cycle 10
PHASE

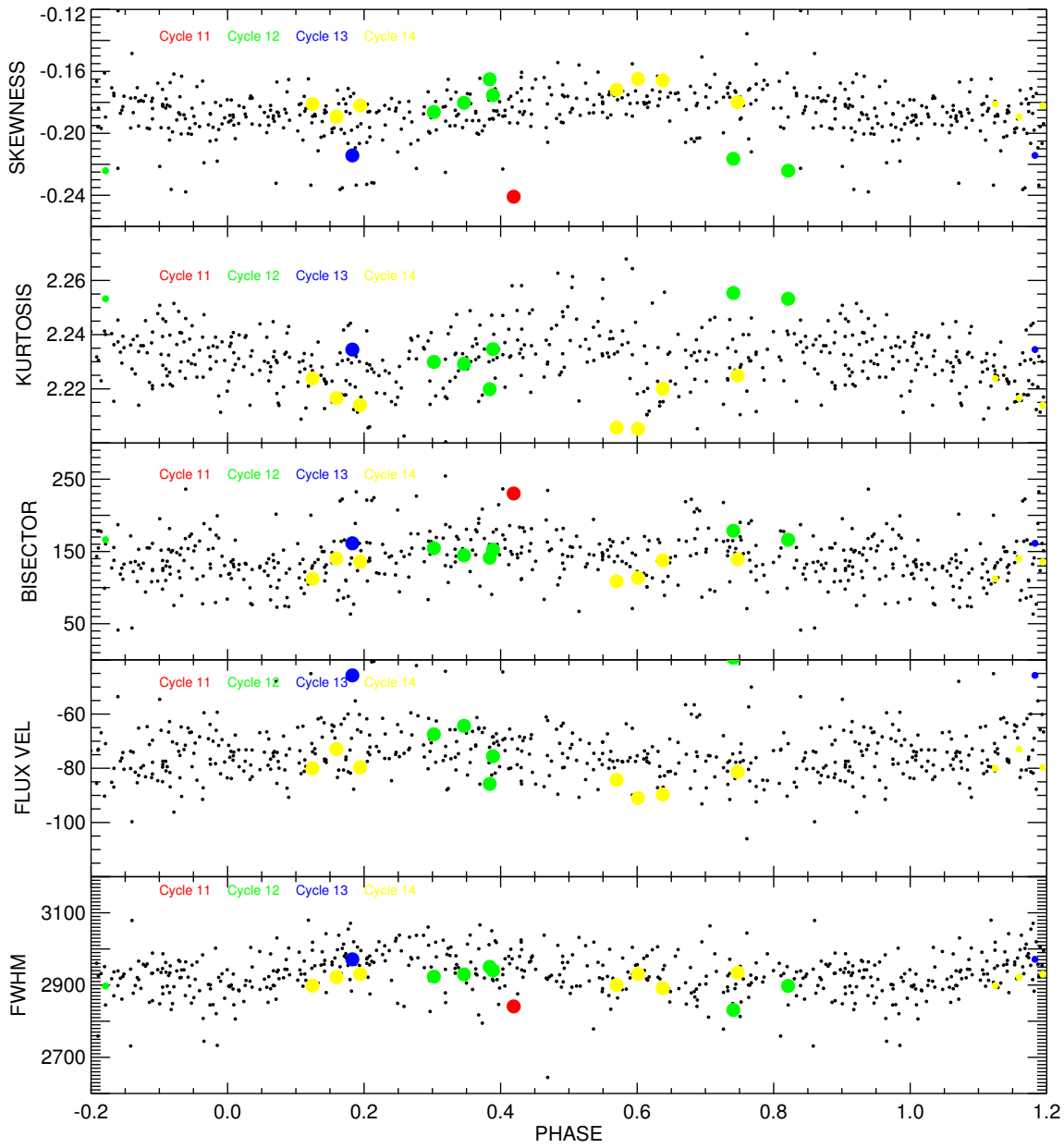
SKEWNESS
-0.12
-0.16
-0.20
-0.24
KURTOSIS
2.26
2.24
2.22
BISECTOR
250
150
50
FLUX VEL
-60
-80
-100
FWHM
3100
2900
2700
Cycle 11
Cycle 12
Cycle 13
Cycle 14
-0.2
0.0
0.2
0.4
0.6
0.8
1.0
1.2
PHASE

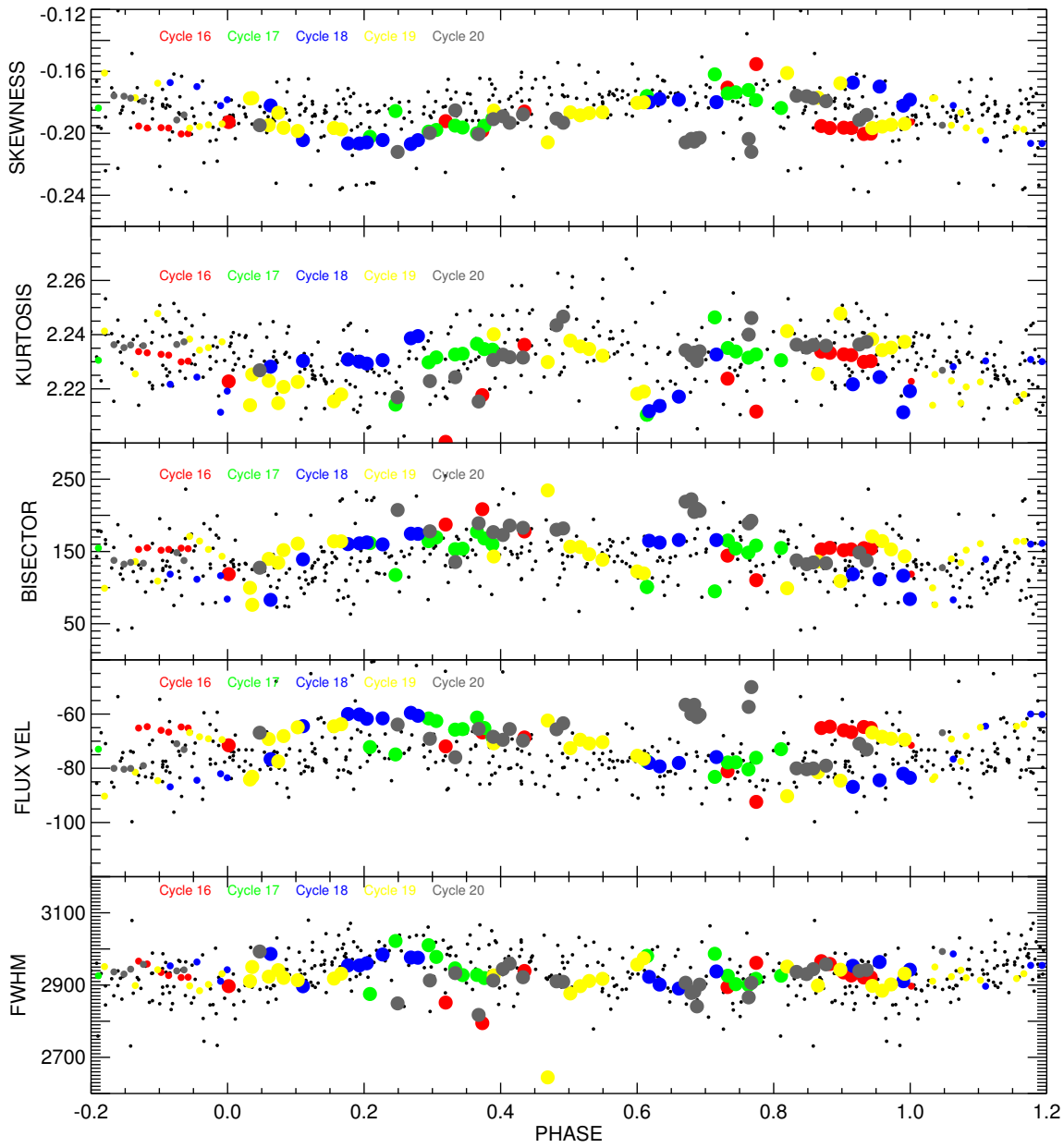
SKEWNESS
-0.12
-0.16
-0.20
-0.24
KURTOSIS
2.26
2.24
2.22
BISECTOR
250
150
50
FLUX VEL
-60
-80
-100
FWHM
3100
2900
2700
Cycle 16
Cycle 17
Cycle 18
Cycle 19
Cycle 20
-0.2
0.0
0.2
0.4
0.6
0.8
1.0
1.2
PHASE

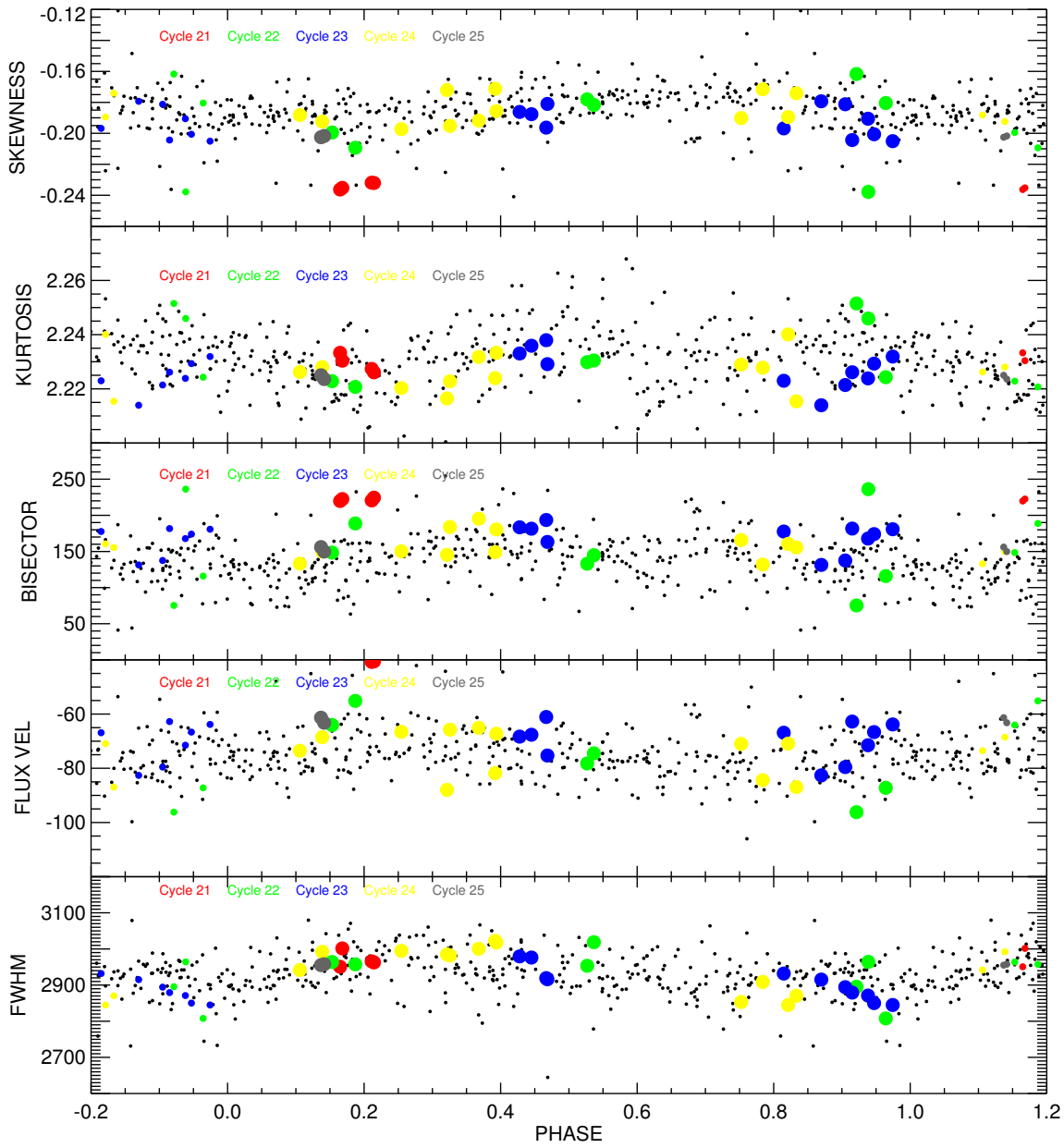
SKEWNESS
KURTOSIS
BISECTOR
FLUX VEL
FWHM
Cycle 21
Cycle 22
Cycle 23
Cycle 24
Cycle 25
PHASE

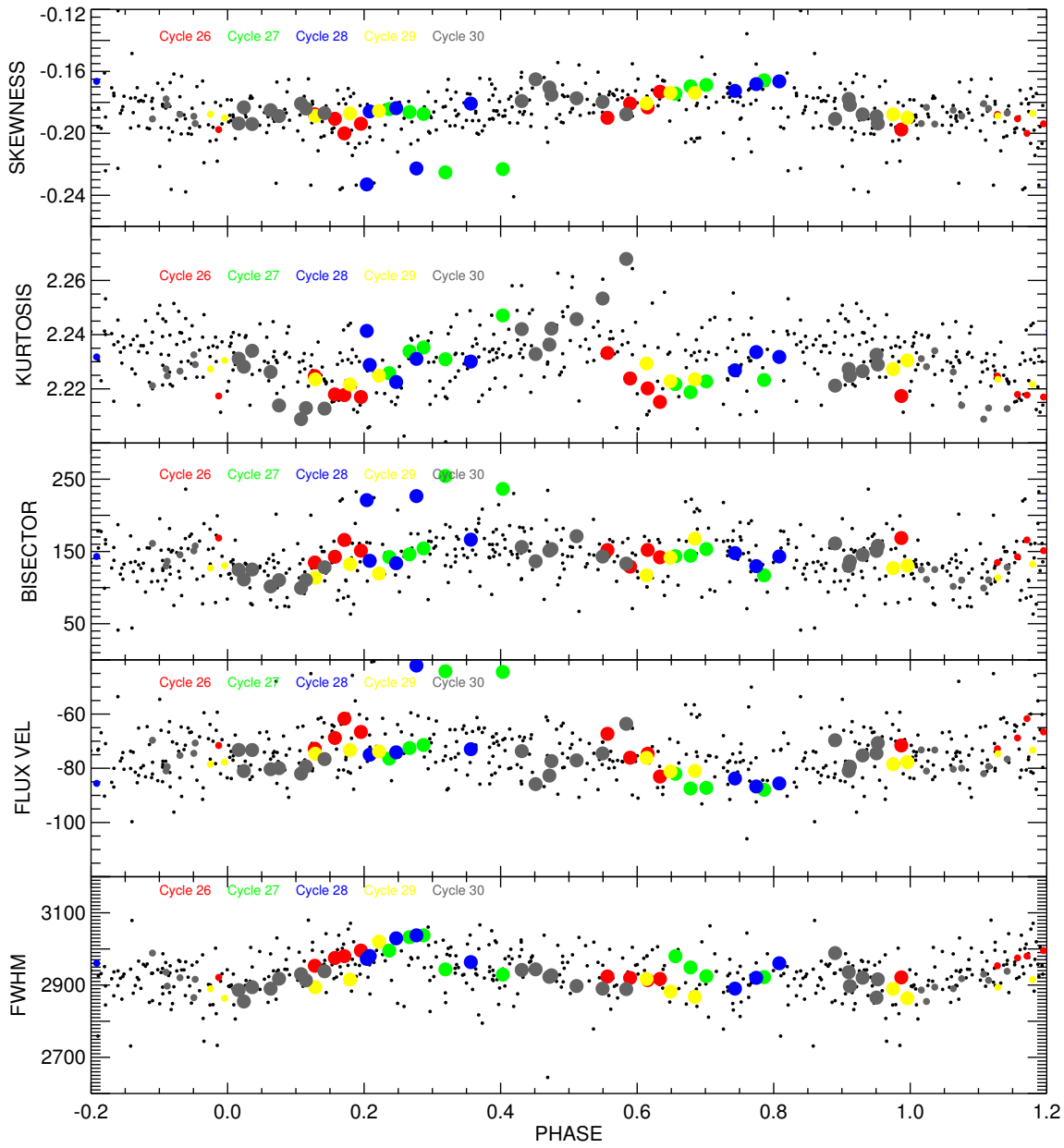
SKEWNESS
-0.12
-0.16
-0.20
-0.24
KURTOSIS
2.26
2.24
2.22
BISECTOR
250
150
50
FLUX VEL
-60
-80
-100
FWHM
3100
2900
2700
Cycle 26
Cycle 27
Cycle 28
Cycle 29
Cycle 30
-0.2
0.0
0.2
0.4
0.6
0.8
1.0
1.2
PHASE

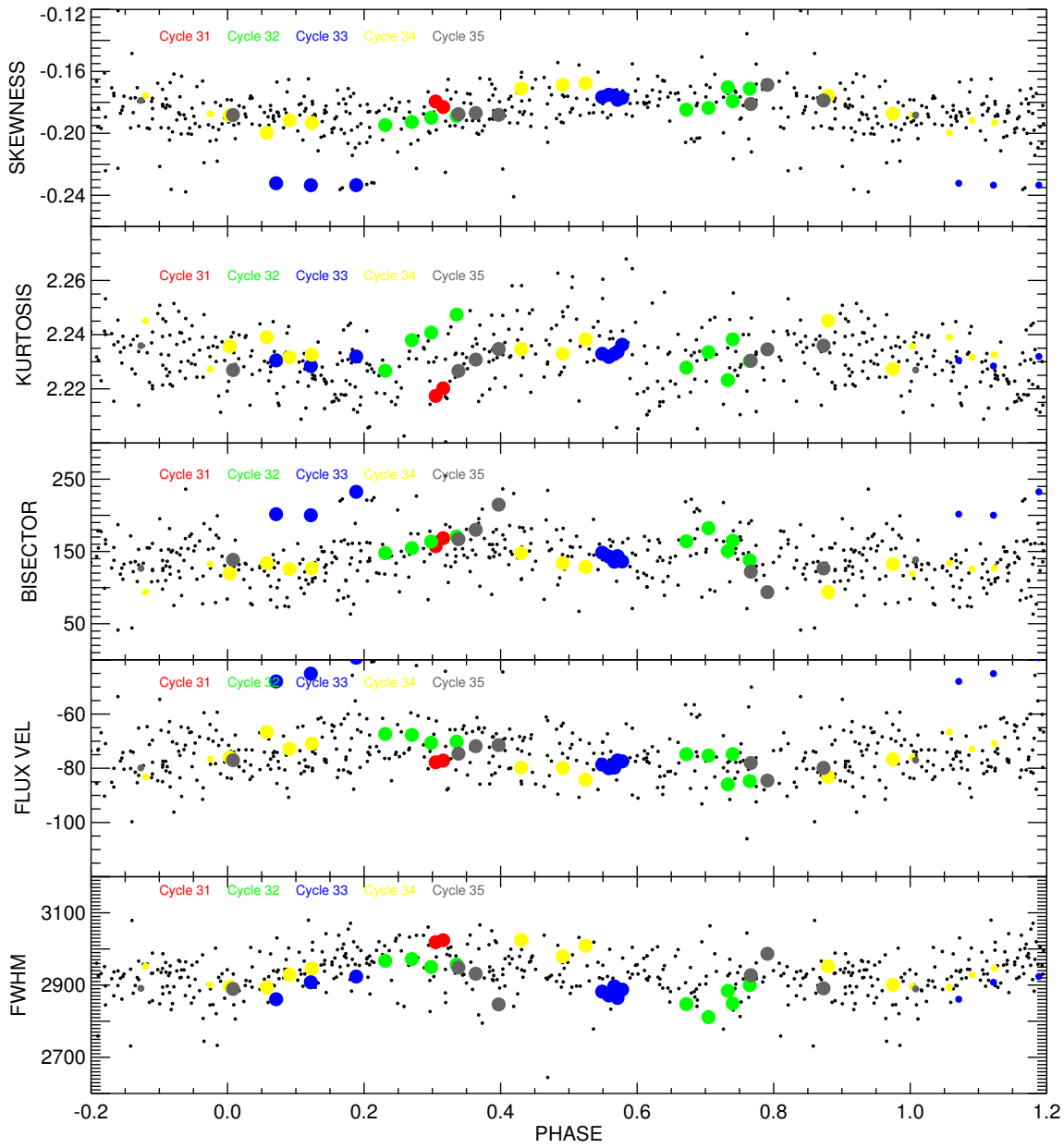
SKEWNESS
KURTOSIS
BISECTOR
FLUX VEL
FWHM
Cycle 31
Cycle 32
Cycle 33
Cycle 34
Cycle 35
PHASE

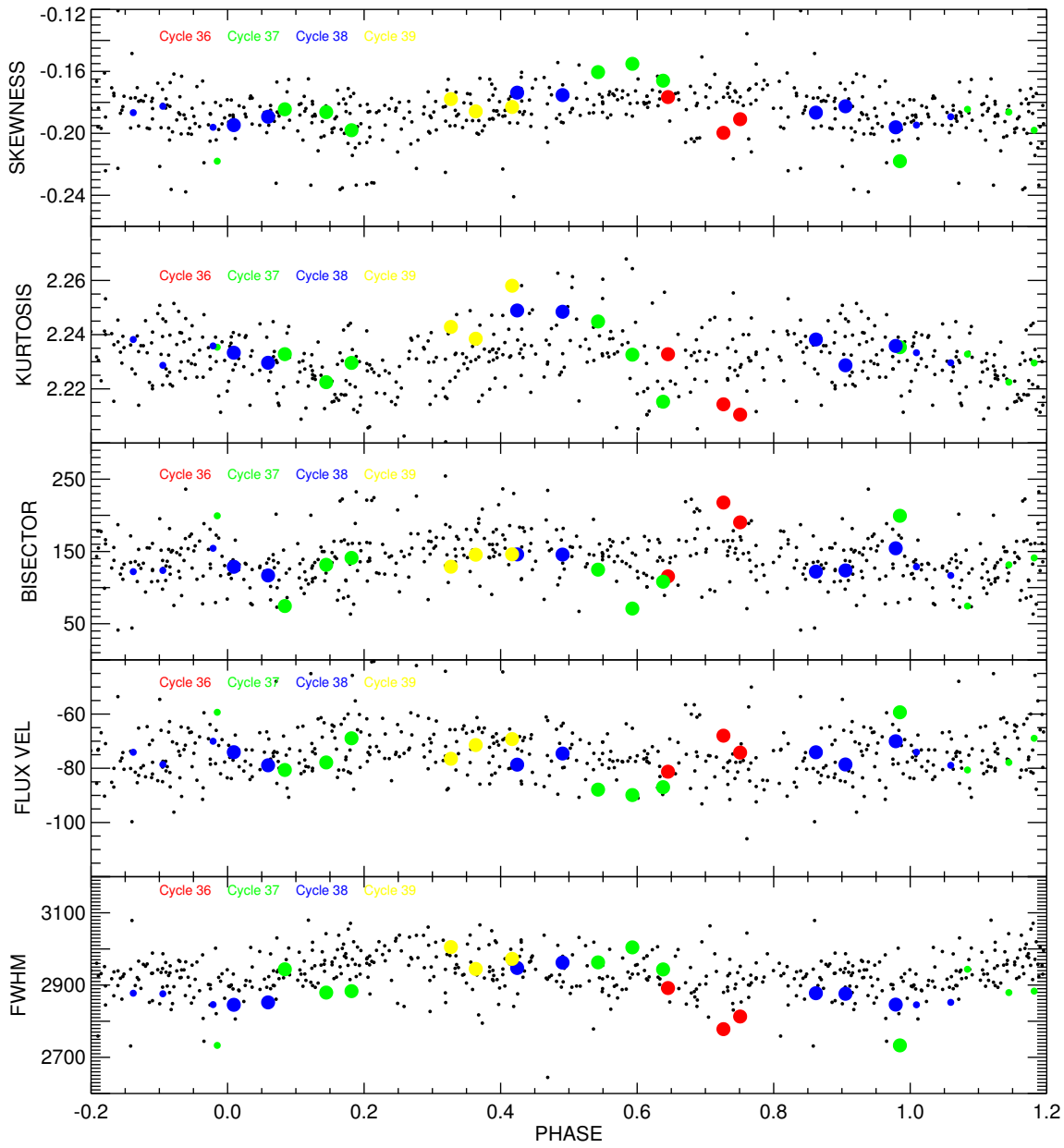
SKEWNESS
-0.12
-0.16
-0.20
-0.24
Cycle 36
Cycle 37
Cycle 38
Cycle 39
KURTOSIS
2.26
2.24
2.22
BISECTOR
250
150
50
FLUX VEL
-60
-80
-100
FWHM
3100
2900
2700
-0.2
0.0
0.2
0.4
0.6
0.8
1.0
1.2
PHASE

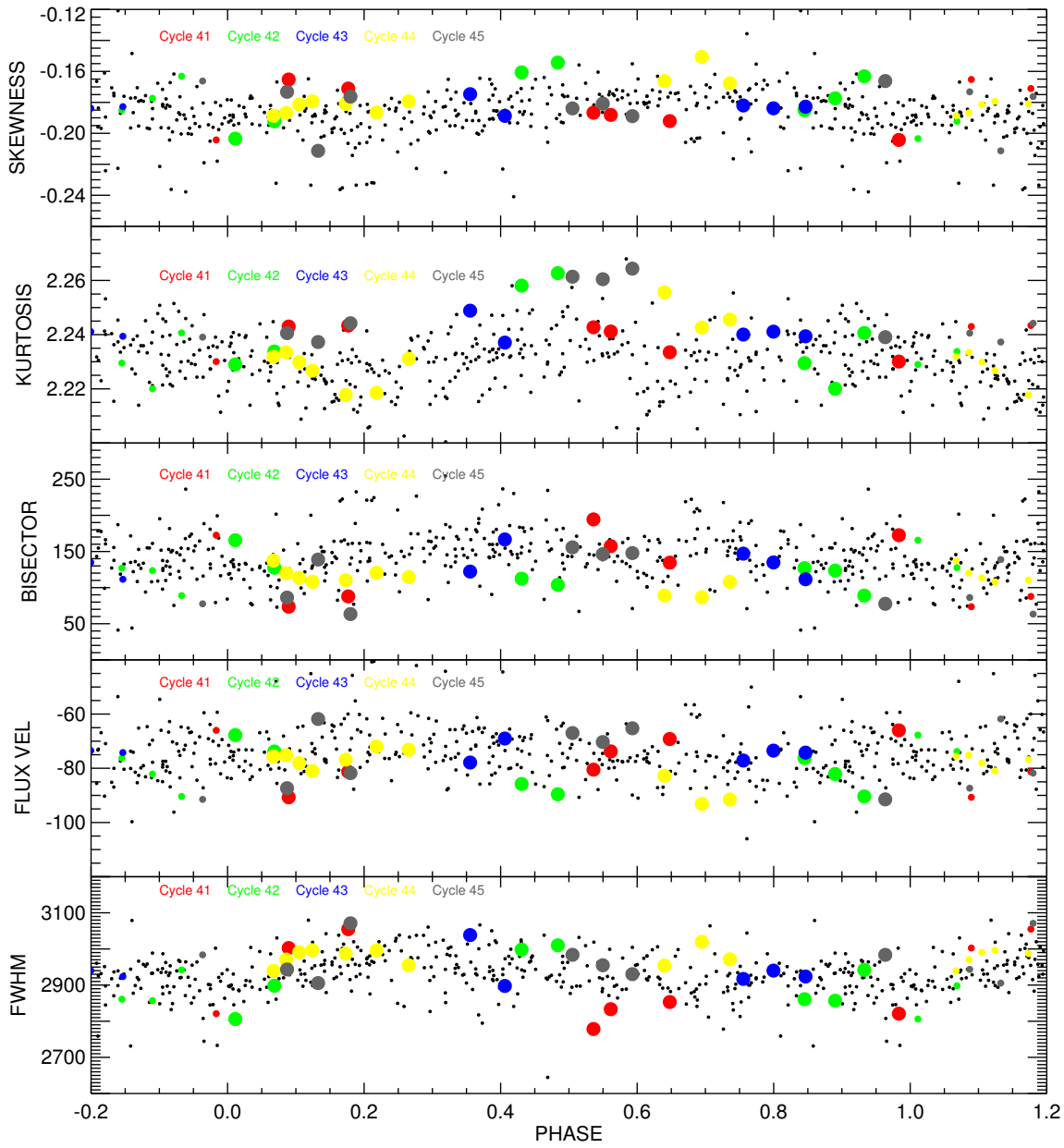
SKEWNESS
-0.12
-0.16
-0.20
-0.24
KURTOSIS
2.26
2.24
2.22
BISECTOR
250
150
50
FLUX VEL
-60
-80
-100
FWHM
3100
2900
2700
Cycle 41
Cycle 42
Cycle 43
Cycle 44
Cycle 45
-0.2
0.0
0.2
0.4
0.6
0.8
1.0
1.2
PHASE

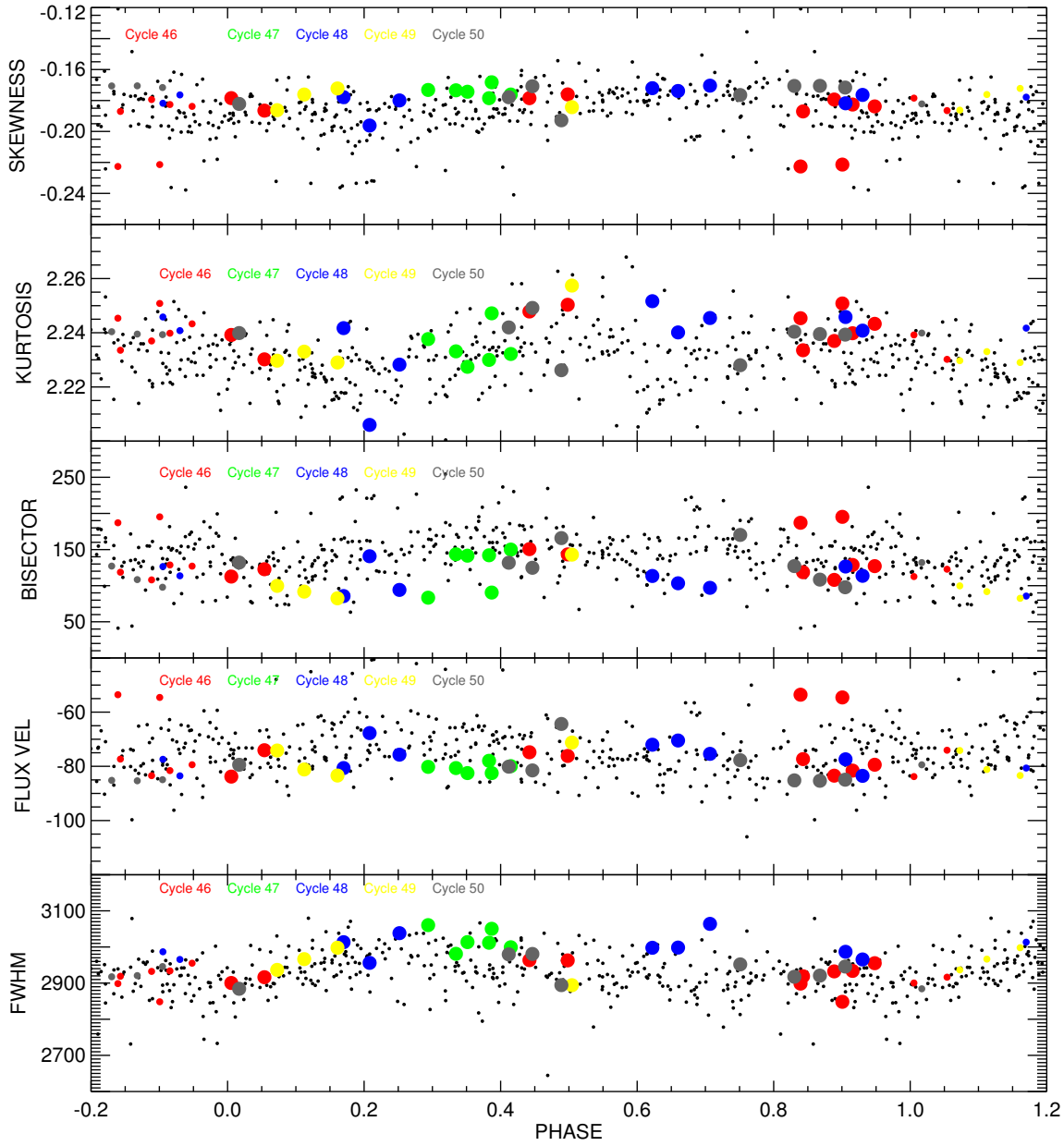
SKEWNESS
-0.12
-0.16
-0.20
-0.24
Cycle 46
Cycle 47
Cycle 48
Cycle 49
Cycle 50
KURTOSIS
2.26
2.24
2.22
BISECTOR
250
150
50
FLUX VEL
-60
-80
-100
FWHM
3100
2900
2700
-0.2
0.0
0.2
0.4
0.6
0.8
1.0
1.2
PHASE

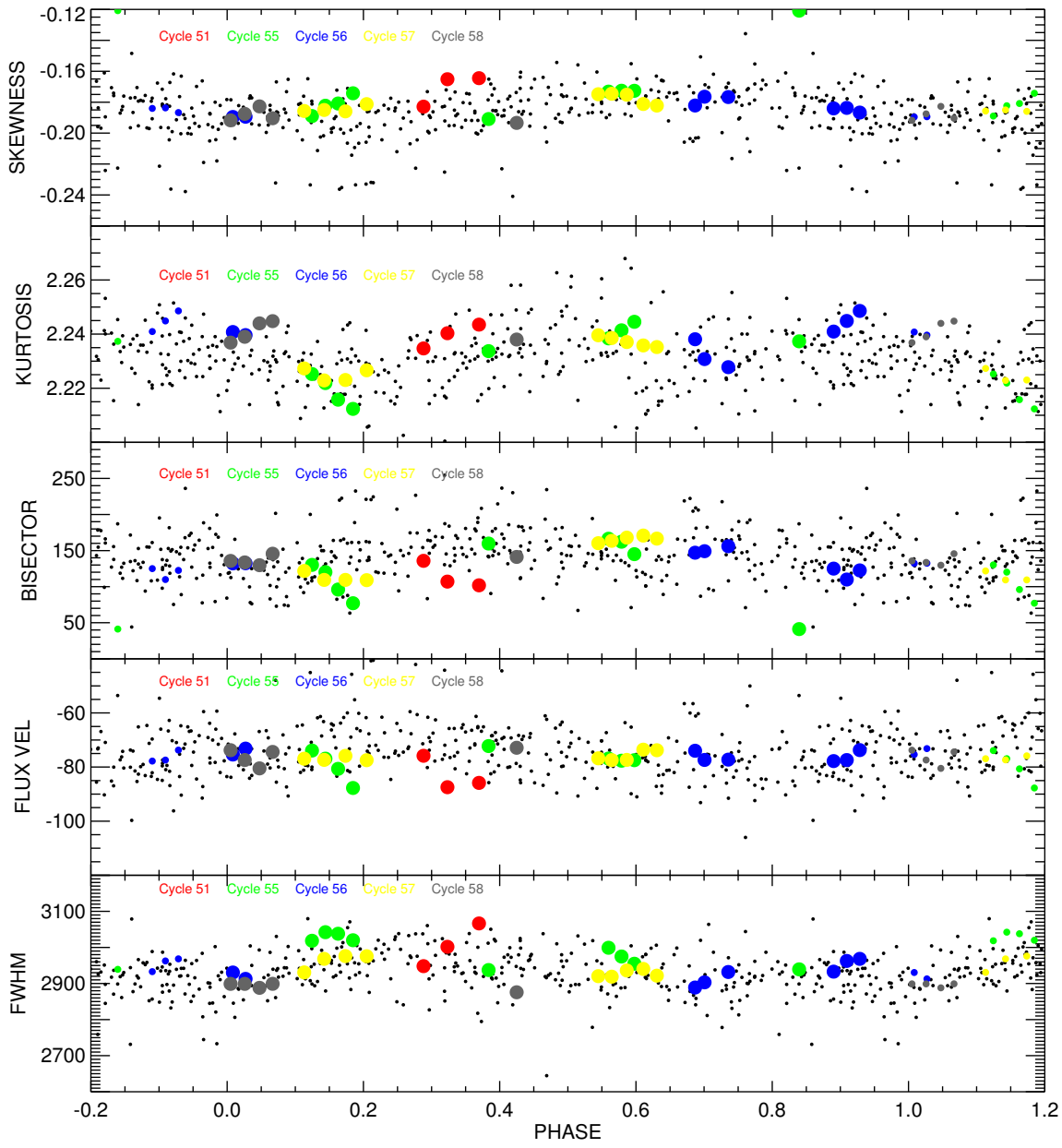
SKEWNESS
KURTOSIS
BISECTOR
FLUX VEL
FWHM
Cycle 51
Cycle 55
Cycle 56
Cycle 57
Cycle 58
-0.12
-0.16
-0.20
-0.24
2.26
2.24
2.22
250
150
50
-60
-80
-100
3100
2900
2700
-0.2
0.0
0.2
0.4
0.6
0.8
1.0
1.2
PHASE